ABSTRACT

FENG, JINYONG. Evaluation of Interfacial Forces and Bubble-Induced Turbulence Using Direct Numerical Simulation (Under the direction of Dr. Igor A. Bolotnov).

High fidelity prediction of multiphase flows is important in a wide range of engineering applications. While some multiphase flow scenarios can be successfully modeled, many questions remain unanswered regarding the interaction between the bubbles and the turbulence, and present significant challenges in the development of closure laws for the multiphase computational fluid dynamics (M-CFD) models. To address these challenges, we propose to evaluate the interfacial forces and bubble-induced turbulence in both laminar and turbulent flow field with direct numerical simulation (DNS) approach.

Advanced finite-element based flow solver (PHASTA) with level-set interface tracking method is utilized for these studies. The proportional-integral-derivative (PID) controller is adopted to ensure the statistically steady state bubble position and perform the detailed study of the turbulent field around the bubble. Selected numerical capabilities and post-processing codes are developed to achieve the research goals. The interface tracking approach is verified and validated by comparing the interfacial forces with the experiment-based data and correlations. The sign change of transverse lift force is observed as the bubble becomes more deformable. A new correlation is proposed to predict the behavior of the drag coefficient over the wide range of conditions. The wall effect on the interfacial forces are also investigated. In homogeneous turbulent flow, the effect of bubble deformability, turbulent intensity and relative velocity on the bubble-induced turbulence are analyzed. The presented method and novel results will complement the experimental database, provide insight to the bubble-induced turbulence mechanism and help the development of M-CFD closure models.

Evaluation of Interfacial Forces and Bubble-Induced Turbulence Using Direct Numerical Simulation

by
Jinyong Feng

A dissertation submitted to the Graduate Faculty of
North Carolina State University
in partial fulfillment of the
requirements for the degree of
Doctor of Philosophy

Nuclear Engineering

Raleigh, North Carolina

2017

APPROVED BY:

_____	_____
Prof. Igor A. Bolotnov Committee Chair	Prof. Nam Dinh
_____	_____
Prof. David Kropaczek	Prof. Venkateswaran Narayanaswamy

DEDICATION

This dissertation is dedicated to my parents and sister.

BIOGRAPHY

The author, Jinyong Feng, was born on September 30th, 1989, a year of snake in Chinese calendar. The family name, Feng, originates from a war hero during the Spring and Autumn period (from approximately 771 to 476 BC) in Chinese history. The first word of the given name, Jin, is shared by all his cousins and has the meaning of gold. The second word of the given name, yong, is given by his father and it means the bravery. His father wishes him to be fearless and explore the outside world.

As the second child in the family, he received high expectation from his parents, especially when he had an outstanding elder sister. His sister was academically always the #1 in their primary and middle school and then went to the #1 university in China, Peking University. The existence of his sister encouraged him to keep challenging himself and breaking through the limits. His mottos of the life is “one’s life must matter”.

He went to one of the top universities (but not #1) in China, University of Science and Technology of China (USTC), and graduated with the Bachelor’s degree in Nuclear Engineering. About 40% of the graduates in USTC will go to U.S. to pursue advanced degrees, like Master’s degree and Ph.D. So the USTC gained a nickname of “United Stated Training Center” in China. Among one of those students, Jinyong was also looking forward to the outside world and making differences in his life. Soon after his graduation, he came to the Texas A&M University. The life in Texas is very enjoyable and the author got a Master’s degree there. After that, he came to the North Carolina State University and conducted research on the two-phase flow simulation under the direction of Dr. Igor A. Bolotnov.

Traveling and sports are his favorite hobbies. Traveling is a great way to explore the beauty of the world and enrich the knowledge. He has visited 29 states of America and gained many great memories, the magnificent Grand Canyon, the bizarre skyline of New York City, -20 ^{o}C chilly temperature of Minnesota, the fabulous Las Vegas, etc. As a crazy basketball fan, one of his lifetime goal is to visit all the home stadiums of the NBA teams. He has visited 24 stadiums and only 5 are left now, Boston Celtics, Portland Trail Blazers, Sacramento Kings, Toronto Raptors and Utah Jazz. The Ph.D. is a milestone in his life, but there are numerous things to explore after that!

ACKNOWLEDGMENTS

I am incredibly thankful to my family. My parents worked very hard to ensure that I can receive the best education. Their great personalities and diligence served as the role model of my entire life. My elder sister gives me lots of helpful advices on my entire career and inspires me to keep pushing myself to the next level. My nephew is almost 3 years now and he is so adorable. My family is the most valuable treasure of my life and I wish to become the one they can be proud of.

I would like to express my sincerest thanks to Dr. Igor A. Bolotnov for all his guidance and help. Dr. Bolotnov brought me into the beautiful world of two-phase bubbly flow and taught me the solid theoretical knowledge, self-motivated research attitude, critical thinking capability and technical writing skills. He helped me grow from a fresh graduate to a serious researcher.

I also want to give thanks to my research group members. Dr. Jun Fang was my undergraduate classmate and we have known each other for almost 8 years. His brilliant guidance and friendly help made me quickly familiarize myself with our research code—PHASTA. We had lots of collaborations on various research topics and it was really enjoyable to work with him. Mr. Aaron Thomas built the foundation of the PID bubble controller and it had incredible value for my research and accelerated my research progress. Dr. Cameron Brown helped me a lot on my thesis and gave me some innovative ideas. The discussion of turbulence theory with him is very beneficial for my research.

I would like to extend my appreciation to my committee members, Dr. Dinh, Dr. Kropaczek and Dr. Narayanaswamy for serving on my committee. My committee members

are world-renowned professors. Their brilliant guidance and thoughtful suggestions helped me improve my understanding on the two-phase bubbly flow phenomena. Many of the faculty, staff, and graduate students in the Department of Nuclear Engineering at NCSU gave me valuable help and assistance. In particular: Dr. J. Michael Doster, Dr. Jack Edwards, Dr. Maria Avramova, Dr. Hong Luo, Dr. Jason Hou, Dr. Koruhonda Murty, Ms. Hermine Kabbendjian, Ms. Lisa Marshall, Mr. Mario Milev, Mr. Yuwei Zhu, Mr. Guojing Hou, Mr. Han Bao, Mr. Chih-Wei Chang, Mr. Hao-Ping Chang, Ms. Mengnan Li, Mr. Yangmo Zhu, Mr. Kaiyue Zeng, Ms. Ting-yi Wang, Ms. Paulina Duckic, etc. I also wanted to express my appreciation to Dr. William D. Pointer for his guidance at Oak Ridge National Lab (ORNL). During the 10-weeks internship, he helped me gain practical experience on developing two-phase boiling model using industrial standard software. His enthusiastic work spirit is very impressive.

Finally, I would like to acknowledge the support from the National Science Foundation—United States (award 13339933 under CBET-Fluid Dynamics Program). Some of the computational resources were supported by U.S. Nuclear Regulatory Commission's Faculty Development Program. An award of computer time was provided by the ASCR Leadership Computing Challenge (ALCC) program. This research used resources of the Argonne Leadership Computing Facility, which is a DOE office of Science User Facility supported under Contract DE-AC02-06CH11357. The solution presented herein made use of the Acusim linear algebra solution library provided by Altair Engineering Inc. and mesh and geometric modeling libraries by Simmetrix Inc.

TABLE OF CONTENTS

LIST OF TABLES

LIST OF FIGURES

LIST OF SYMBOLS OR ABBREVIATIONS

Abbreviation

3D	Three dimensional
BIT	Bubble-induced turbulence
BCT	Boundary condition transient data
CFD	Computation fluid dynamics
DES	Detached eddy simulation
DNS	Direct numerical simulation
E-E	Eulerian-Eulerian approach
E-L	Eulerian-Lagrangian approach
FEM	Finite element method
GCI	Grid convergence index
HOT	Higher order terms of truncation error
HPC	High performance computing
ITM	Interface tracking method
LES	Large eddy simulation
M-CFD	Multiphase computational fluid dynamics
PDE	Partial differential equation
PHASTA	Parallel, Hierarchic, Adaptive, Stabilized, Transient Analysis flow solver
RANS	Reynolds-Averaged Navier-Stokes equations
TKE	Turbulent kinetic energy
VOF	Volume of fluid

Notation

A	Bubble cross-sectional area (m^2)
A'''	Interfacial area density (m^{-1})
B	Constant used in “log law”
C	Coefficient for power decay law of turbulent kinetic energy
C_B	Coefficient of bubble-induced turbulence eddy viscosity for Sato’s model
C_D	Drag coefficient
$C_{\varepsilon 1}$	Constants used in $k-\varepsilon$ model
$C_{\varepsilon 2}$	Constants used in $k-\varepsilon$ model
C_L	Lift coefficient

C_L^D	Modified lift coefficient
C_μ	Constants used in $k-\varepsilon$ model
C_{TD}	Turbulent dispersion coefficient
C_p	Potential flow solution coefficient
C_T	Net transverse lift coefficient
C_{VM}	Virtual mass coefficient
C_W	Wall coefficient
$CF_i^{(n)}$	i^{th} component of the control force at time n
d	Scalar in re-distancing equation (m)
D	Spherical bubble diameter (m)
D_H	Extended bubble diameter (m)
$\frac{D}{Dt}$	Substantial derivatives
E_o	Spherical bubble-based Eotvos number
E_{o_H}	Extended bubble-based Eotvos number
f	Body force term
F_D	Drag force (N)
F_L	Lift force (N)
F_s	Factor of safety in GCI
F_{TD}	Turbulent dispersion force (N)
F_{VM}	Virtual mass force (N)
F_W	Wall force (N)
H_ε	Heaviside kernel function
I	Turbulent intensity
k	Liquid turbulent kinetic energy (m^2/s^2)
L	Distance between bubble center and the wall (m)
M	Spacing between two grids (m)
M_k	Momentum exchange term of phase k ($kg/(m^2.s^2)$)
M_k^D	Momentum exchange term of phase k caused by drag force ($kg/(m^2.s^2)$)
M_k^L	Momentum exchange term of phase k caused by lift force ($kg/(m^2.s^2)$)
M_k^{VM}	Momentum exchange term of phase k caused by virtual mass force ($kg/(m^2.s^2)$)
M_k^{TD}	Momentum exchange term of phase k caused by turbulent dispersion force ($kg/(m^2.s^2)$)
M_k^W	Momentum exchange term of phase k caused by wall force ($kg/(m^2.s^2)$)

Mo	Morton number
n	Power decay exponent
n_w	Unit normal vector
N_p	Number of phases in M-CFD governing equations
p	Pressure (N/m^2)
Q	q-criterion (s^{-2})
Re	Reynolds number
Re_b	Bubble Reynolds number
Re_τ	Friction Reynolds number
S	Strain rate tensor (m/s)
Sr	Non-dimensional shear rate
t	Time (s)
$\vec{w}$	Pseudo velocity in re-distancing equation (m/s)
We	Weber number
u	Streamwise direction (x) velocity (m/s)
$\bar{u}$	Mean velocity (m/s)
u'	Root-mean-square of the turbulent velocity fluctuations (m/s) or instantaneous velocity fluctuation (m/s)
${u'_E}^2$	Excess turbulent kinetic energy (m^2/s^2)
u_g	Gas velocity (m/s)
u_l	Liquid velocity (m/s)
u_r	Relative velocity between liquid and gas (m/s)
u_η	Kolmogorov velocity scale (m/s)
$\overline{u'u'}$, $\overline{v'v'}$, $\overline{w'w'}$	Reynolds stress terms (m^2/s^2)
U_o	Mean streamwise velocity in wind tunnel experiment (m/s)
U	Mean velocity (m/s)
v	Wall normal (y) direction velocity (m/s)
V_b	Bubble volume (m^3)
w	Lateral (z) direction velocity (m/s)
x	Streamwise (x) direction coordinate (m)
x_o	Virtual origin in wind tunnel experiment (m)
y	Wall-normal (y) direction coordinate (m)
z	Spanwise (z) direction coordinate (m)

Greek letters

α	Void fraction
α_{gs}	Void fraction in the small bubble region
δ	Channel width (m)
ε	Turbulence dissipation rate (m^2/s^3)
ε_l	Interface half-thickness in level-set equation (m)
ε_d	Interface half-thickness in re-distancing equation (m)
η	Kolmogorov length scale (m)
η_j^i	Computing efficiency, where i represents the bct file computing approach and j represents the number of partitions
κ	Constants used in $k-\varepsilon$ model or curvature of gas-liquid interface or the constant used in "log law"
λ	Taylor length scale (m)
φ	Scalar in advection equation (m)
ϕ_{sr}	Dimensionless drag multiplier
σ_k	Constants used in $k-\varepsilon$ model
μ_{BIT}	Bubble-induced turbulence dynamics viscosity ($N.s/m^2$)
μ_l	Liquid dynamic viscosity ($N.s/m^2$)
μ_t	Turbulent dynamic viscosity ($N.s/m^2$)
ν_l	Liquid kinematic viscosity (m^2/s)
ν_t	Turbulent kinematic viscosity (m^2/s)
ω	Shear rate (s^{-1})
Ω	Vorticity tensor (s^{-1})
σ	Surface tension (N/m)
τ	Pseudo time in re-distancing equation (s)
τ_{ij}	Viscous stress tensor (N/m^2)
τ_η	Kolmogorov time scale (s)
ρ_c	Continuous phase density (kg/m^3)
ρ_g	Gas density (kg/m^3)
ρ_l	Liquid density (kg/m^3)

CHAPTER 1. INTRODUCTION

1.1 Overview and motivation

Two-phase turbulent flows are widely encountered in light water reactor (LWR) engineering. Modern computing capabilities allow the migration to higher fidelity tools in thermal-hydraulics analysis to predict transient, three-dimensional behavior of two-phase flows in nuclear reactors. While modeling the turbulent single-phase flow using computational fluid dynamics (CFD) has already reached a certain level of maturity, the two-phase turbulent flow modeling still requires further development to achieve widespread adoption in nuclear engineering community. Currently, there is a high degree of empiricism in the two-phase turbulent flow models due to the complexity of the coupled flow and bubble-turbulence interaction mechanism. To obtain better understanding of the two-phase flow interaction mechanisms, it is desirable to utilize the direct numerical simulation (DNS) approach. In contrast with the Reynolds-Averaged Navier-Stokes (RANS) approach, DNS directly solves the Navier-Stokes equations without any turbulence closure models. This approach requires a full 3D time resolved simulations and thus, is a relatively new direction in turbulence studies since it has become affordable only in the past two decades due to the advancement of computing capabilities. However, the current computational power still does not permit full DNS of the realistic bubbly turbulent flow in large engineering systems. Therefore, the research and engineering community has been typically using turbulence models (such as large eddy simulation (LES), RANS, etc.) which needs the knowledge of turbulence parameters, like Reynolds stress, turbulent viscosity and bubble-induced turbulence viscosity. The estimation

of those parameters can be done using the advanced modeling approach, DNS method, to provide insight into this phenomenon. Furthermore, the closure of the governing equations in most of the multiphase CFD models (except DNS) requires the knowledge of interfacial forces (i.e., drag, lift, virtual mass, turbulent dispersion force). These key challenges were traditionally addressed with experiments, but not fully investigated due to the limitations of real experiment. We can now help address these challenges through the presented modeling approach.

The multiphase computational fluid dynamics (M-CFD) codes rely on the interfacial closure laws to model the bubble distribution and dispersion in the domain. The closure laws are normally developed based on experimental data [1, 2] and analytic solutions for very simple conditions. An interfacial closure law should have the following three features: (i) it must comply with actual physics and can describe physical phenomena of bubbly flows under different operating environments; (ii) the closure law should be a formula as simple and general as possible, and its profile should be continuous and should not show abnormal changes; (iii) factors influencing the closure law should be considered as comprehensively as possible. Although the experiments provide valuable databases for the development and validation of numerical models in the nuclear industry, the rapid advancement of computer power has made the DNS approach feasible in studying complex fluid dynamics problems.

Among the several interfacial forces, drag and lift forces are of special importance, due to the direct influence on the streamwise mean velocity and the lateral distribution of bubbles in two-phase flows. It has been observed in experiments [3-5] that the lateral migration of bubbles strongly depends on the bubble deformability, which typically depends on bubble size

and can be described by a dimensionless number (e.g. Eötvos number). Small, spherical bubbles in upflow conditions tend to migrate toward the pipe wall, which cause a wall-peaked bubble distribution, whereas large, deformable bubbles tend to migrate towards the pipe center, which result in a core-peak bubble distribution [4, 6]. Lu and Tryggvason [7] revealed that this phenomenon is caused by the bubble deformability, not the size of the bubbles, by simulating the bubble behavior in turbulent bubbly flow. The migration of bubbles can be explained by the shear-induced lift force [2, 3]. In this paper, we analyze the lift forces acting on a single bubble in low shear laminar flow (3.8 s^{-1}) and our results are consistent with the experimental observations [2, 8]. Then the more complex scenarios, the wall effect on the interfacial forces, are investigated by considering the influence of wall distance, bubble deformation level and bubble Reynolds number.

In addition to the interfacial force modeling, some of the critical issues in the development of a two-phase turbulent model is the understanding of the mechanisms in which the existence of bubbles alters the turbulence generation, redistribution and dissipation in the liquid phase. The effect of bubbles on the liquid is generally called bubble-induced turbulence (BIT). Therefore the development of a suitable model for bubble-induced turbulence is a key element to get a complete working model that allows predictive CFD-simulations for engineering applications involving turbulent bubbly flow.

Based on the well-established single-phase models, two-phase turbulence models are obtained using empirically established bubble-induced closure terms [9, 10]. The analytical form [11] for bubbles' contribution to the turbulence was formulated by the derivation of basic balance equations for turbulent kinetic energy and Reynolds stresses in gas liquid flow [12-

14]. The available experimental capabilities [15-17] only allowed for the estimation of the net change in turbulence level for multiple bubble flows. However, detailed studies on how individual bubbles contribute to the turbulence are limited and difficult to conduct experimentally. In this research, we plan to use a validated numerical approach together with flow control to conduct a set of systematic studies.

DNS, where all flow scales, from the largest turbulence eddies to the Kolmogorov scale, are fully resolved, provides a complete picture of the 3D time-dependent flow field (provided the computational grid is fine enough for the simulated flow). Numerical simulation also allows for performing parametric studies more easily than experiments since one can control a single parameter (e.g., surface tension or turbulent intensity) and analyze the influence of this parameter on the two-phase flow turbulence. The previous research on the behavior of deformable bubbles mainly focused on the transverse migration of bubbles [2, 18] to estimate lift force and influence of void fraction on the liquid turbulence in bubbly flow [19]. Note that many of these papers deal with laminar flows, which are rare in practical engineering applications.

Spherical and deformable bubbles will behave differently when interacting with liquid turbulence. Since the vorticity generated at a free surface is proportional to the local curvature, the deformable bubbles generate turbulent vorticity at a higher rate compared to a spherical bubble [20]. This way, the bubble shape influences the distribution of energy exchange between the liquid and gas phases. Stewart [21] showed that the turbulent kinetic energy enhancement is observed and caused by the wake capture and collision process of deformable bubble. The wake detachment creates turbulence which can be called wake generated

turbulence. A more detailed examination of the wake structure by Brucker [22] suggested that this amplification is due to the enlargement of the wake during the collision. Bunner and Tryggvason [23] confirmed that the turbulent kinetic energy induced by the bubbles in the liquid, with void fraction of 6%, is larger for deformable bubbles than spherical bubbles. These previous studies provide conceptual ideas regarding the general trend for how bubble deformability affects the bubble-induced turbulence. In the present research, we analyze the magnitude of the bubble-induced turbulence for a single bubble with controlled conditions in homogeneous turbulence field.

In this thesis, we will summarize the current status of the knowledge on bubble-induced turbulence (Section 1.7) and then introduce the numerical methods we are using (Chapter 2). Then we will present our results on the evaluation of interfacial forces, drag and lift force, under both laminar and turbulent flow conditions (Chapter 3) by comparing with the experiment-based correlations to justify the validity of interface tracking method. We have also separately studied (Chapter 4) the influence of three major parameters on the bubble induced turbulence in homogeneous two-phase turbulent flow: (i) surface tension, (ii) turbulent intensity and (iii) relative velocity. Previous numerical studies of bubbly flows typically dealt with nearly spherical bubbles [24], often in laminar flows. Realistic flows encountered in industrial applications and in nature often contain ranging bubble sizes, including deformed bubbles. The bubble deformation study would demonstrate the trend when the bubble would enhance or suppress liquid turbulent kinetic energy and investigate the relationship between bubble deformability and the BIT. The turbulent intensity study would provide insight on the amount of energy transferred between the bubble and the liquid turbulence as a function of

turbulence level already present in the flow. The main motivation for the presented research is to review the closure parameters of the major bubble-induced turbulent kinetic energy models [13, 14, 25], and propose new formulations for the energy transfer between bubble and liquid based on the obtained results.

1.2 Turbulence modeling and simulation

Turbulence is one of the most challenging and interesting phenomena in nature. It plays an important role in natural and engineering systems [26, 27]. For more than a hundred years [28-30], scientists have been working to understand the nature of turbulence and proposed numerous models [28, 31, 32]. The Navier-Stokes equations govern the velocity and pressure distribution of the fluid flow. For turbulent flows, one way to average the Navier-Stokes equations results in the Reynolds-Averaged Navier-Stokes (RANS) equations [27] which assume that the flow velocity field can be split into the mean and fluctuating components. The mass and momentum equations are solved for the mean quantities and a closure law for so-called Reynolds stress tensor is required to represent the effect of the unresolved fluctuations on the mean velocity field. Many models, e.g., [33], use the Boussinesq [29] approximation by introducing the turbulent viscosity, v_t, to model the turbulence. In contrast to single-phase turbulence, relatively little research has been done for turbulent two-phase flows. Two-phase turbulence simulation and analysis play a pivotal role in many engineering disciplines, including nuclear, chemical and biomedical engineering [26]. High-quality two-phase turbulence models are needed to accurately predict phase distribution and separation phenomenon. Naturally, the modelling of two-phase turbulence is even more involved and

typically requires a larger number of closure laws to predict the flow behavior [26, 34-36]. Many questions remain unanswered in two-phase modeling approach [35, 37].

In contrast with RANS approach, DNS directly solves the Navier-Stokes equations. With sufficiently temporal and spatial resolution, DNS can represent all the scales of turbulence down to the Kolmogorov scales, thus providing high-fidelity fundamental insights to complex fluid phenomena. Reynolds number play an important role in the grid resolution requirements for DNS and the 3D mesh size grows exponentially (power of 9/4) with Reynolds number (Appendix A). Thus, early research performed the simulation of single-phase turbulent flows in a channel at relatively low Reynolds numbers [38] (about 180 based on the friction velocity and channel half-width which corresponds to about 11,200 Reynolds number based on mean velocity and hydraulic diameter). More recently, Lee and Moser [39] conducted an unprecedented DNS of incompressible channel flow at friction Reynolds number of 5186 which corresponds to 500,000 Reynolds number based on mean velocity and hydraulic diameter. This large scale simulation represents a clear demonstration of DNS capability for practical engineering flows, such as in nuclear reactor cores (operating PWR core has flows at Reynolds number about 500,000 as well). The channel flow simulations provided much better understanding of turbulence and allowed the development of new turbulence models [40, 41] based on the analysis of the DNS data [42].

For two-phase turbulent flow simulation, DNS can be coupled with several interface tracking methods (ITM), such as volume of fluid (VOF) method [43, 44], front tracking method [45, 46] and level-set method [47]. Those simulations were normally limited to low Reynolds numbers and only tens of bubbles [45, 48] and thus produced limited information about real

world bubble-liquid interactions. Systematic parametric studies are also expensive to perform due to the significant computational cost of each separate simulation.

In the past decade, DNS coupled with the interface tracking method has been extensively used to study the bubble-turbulence interaction [44, 46, 49]. As first-principle based approach, DNS can serve as the "virtual experiment" to help fill the knowledge gap between the current understanding of two-phase flows and that required for future engineering applications. A systematic investigation on the bubble-turbulence interaction is feasible using DNS approach. Care needs to be exercised in: (a) quantitatively defining the liquid phase turbulence prior to the introduction of bubbles; (b) understanding the roles of size, shape and interface mobility of bubbles; (c) proper bubble-liquid coupling. Ilic et al. [24] quantified the turbulent kinetic energy balance in bubble-induced turbulence and evaluated the energy spectra in bubble driven liquid flow using DNS [50]. Turbulent bubbly channel flows were extensively studied by Tryggvason et al. [26, 51, 52] under low Reynolds number conditions. Bolotnov et al. [48] investigated the turbulent bubbly channel flow using the level-set method and later performed turbulence anisotropy analysis for bubbly turbulence with Reynolds number up to 400 (based on friction velocity) [53].

However, the cost of these simulations usually limited the studies to a few cases. In this research, we will afford to perform DNS/ITM routinely with the available computational facilities locally and remotely. Utilizing the previously developed tools for data analysis [53-55] and flow control [56], we plan to produce a systematic database of bubble-turbulence interactions and allow for creating new models for bubble-induced turbulence and interfacial momentum transfer forces.

1.3 Decay of homogeneous turbulence

In the single-phase turbulent flow, the turbulence energy spectrum is considered to follow the Richardson's [57] description. Large scale eddies are generated in the regions of high velocity gradients and the mean kinetic energy is converted into turbulent kinetic energy. These larger scale eddies are not stable and undergo continuous breakage process (energy cascade in the spectral inertial range) till the Kolmogorov length scale is achieved beyond which the fluid viscosity dissipates the turbulent kinetic energy. Given the two parameters, dissipation rate ε and kinematic viscosity ν_l, the Kolmogorov scales are determined from dimensional considerations as follows

$$\text{length scales: } \eta = \left(\frac{\nu_l^3}{\varepsilon}\right)^{\frac{1}{4}} \quad (1)$$

$$\text{velocity scales: } u_\eta = (\varepsilon \nu_l)^{\frac{1}{4}} \quad (2)$$

$$\text{time scales: } \tau_\eta = \left(\frac{\nu_l}{\varepsilon}\right)^{\frac{1}{2}} \quad (3)$$

Two identities stemming from these definitions clearly indicate that the Kolmogorov length scales characterize the smallest dissipative eddies. First, the Reynolds number based on the Kolmogorov scales is unity, i.e., $\frac{\eta u_\eta}{\nu_l} = 1$, which is consistent with the notion that the cascade proceeds to smaller and smaller scales until the Reynolds number is small enough for the dissipation to be effective. Second, the dissipation rate is given by

$$\varepsilon = \nu_l \left(\frac{u_\eta}{\eta}\right)^2 = \frac{\nu_l}{\tau_\eta^2} \quad (4)$$

It shows that $\left(\frac{u_\eta}{\eta}\right) = \frac{1}{\tau_\eta}$ provides a consistent characterization of the velocity gradients of the dissipative eddies. The Kolmogorov length scale will be used to determine the grid resolution for the generation of turbulent flow using DNS [27].

The decay of the turbulence generally follows the power laws. Experimentally, a good approximation to decay of homogeneous turbulence can be achieved in wind-tunnel experiments by passing a uniform stream (of velocity U_o in the x direction) through a turbulence generating grid as shown in Figure 1. In the absence of mean velocity gradients, homogeneous turbulence decays because there is no turbulence production due to local shear. In the laboratory frame, the flow is statistically stationary and statistics vary only in the x direction. In the frame moving with the mean velocity U_o, the turbulence is homogeneous and it evolves with time ($t = x/U_o$).

The classic paper by Comte-Bellot and Corrsin [58] provide measured $\langle u^2 \rangle$ and $\langle v^2 \rangle$ values from the decay of grid turbulence experiment. They suggested that the normal stresses and turbulent kinetic energy, *k*, decay following the power laws, which, can be written as

$$\frac{k}{U_0^2} = C\left(\frac{x - x_0}{M}\right)^{-n} \quad (5)$$

where x_o is the virtual origin, M is the spacing between the two grid rods. Values of the decay exponent n between 1.15 and 1.45 are reported in the literature [58-61]. Samtaney et al. [62] performed the DNS of decaying compressible, isotropic turbulence at fluctuation Mach number from 0.1 to 0.5 and found the power components $n = 1.3{\sim}1.7$. The value of C varies widely depending on the geometry of the grid and the Reynolds number.

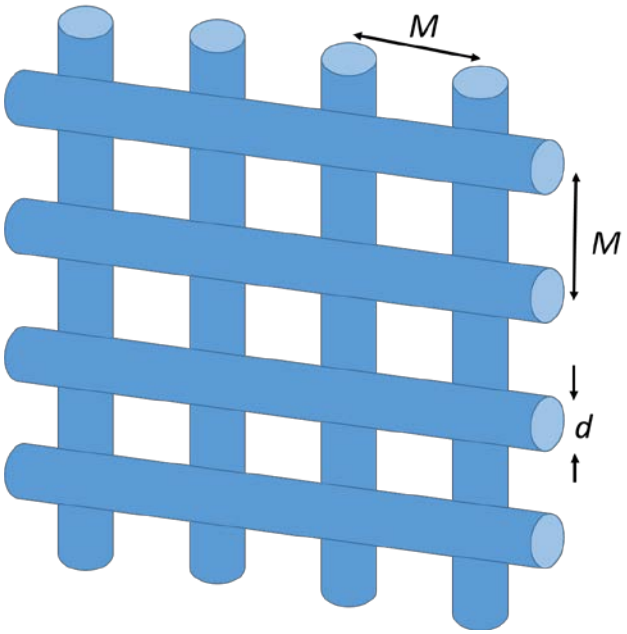

Figure 1. A sketch of a turbulence-generating grid composed of bars of diameter *d*, with mesh spacing *M* [27].

In this research, we will numerically generate homogeneous turbulent flow and shear turbulent flow using the block-induced turbulence method. As the flow passes through the designated obstacles, i.e., spheres, with high Reynolds number, the existence of obstacles will disrupt the liquid velocity field and create instabilities [16, 63]. Periodic boundary conditions will be used to let the instabilities develop to a quasi-steady turbulence field. The decay of homogeneous turbulent flow is validated with the experiment-based coefficient and will be discussed later.

1.4 Multiphase flow modeling

Thanks to the increasing computer power and advanced algorithms, numerical simulation of multiphase flows, especially computational fluid dynamics (CFD) approach,

emerges as an effective tool for exploring the multiphase flow. Due to the wide range of spatial and temporal scales in the industrial size system, it is virtually impossible to capture all the details of the flow field with the current available computational resources. Depending on the scales, three approaches are mostly used to simulate bubbly flows: the Eulerian-Eulerian (E-E) approach, the Eulerian-Lagrangian (E-L) approach and the Interface Tracking Methods (ITM) which is often coupled with direct numerical simulation (DNS) or large eddy simulation (LES) for turbulence modeling. These three approaches have their own advantages and disadvantages and their specific range of applicability. In the E-E approach, which is also referred to as the two-fluid model [11, 35, 64], both phases are treated as continuum fluids. The ensemble-averaged mass and momentum conservation equations are used to describe the time-dependent motion of both phases. In case of adiabatic two-phase flow without phase change, the closure terms are the interfacial forces terms which are generally considered to include the drag force [1, 65], lift force [2, 66], wall force [67, 68] and turbulent dispersion force [69-71] and the bubble-induced turbulence terms [14, 72, 73]. At this level of E-E continuum models, bubbles lose their discrete identity, which enables the simulation of relatively large systems and the study of various flow regimes, like bubbly flow, slug flow, churn-turbulent and annular flow, in a single channel. In the E-L approach, each bubble is separately tracked while the liquid phase is treated as a continuum. The interaction between the bubbles and the liquid is accounted for through a source term [1, 74] in the momentum equations. Several thermal-hydraulics codes, such as TRACE [75], RELAP5 [76], GOTHIC [77] and Cobra-TF [78], have been developed to analyze the reactor transients and heat transfer phenomena based on either E-E or E-L approach. Since the E-E approach treats the gas bubble

or particles as a continuum phase and the E-L approach treats the gas bubble as a non-deformable spherical particle, both cannot be used for describing a deformable bubble behavior.

DNS is a useful tool to improve the current understanding of the local and instantaneous properties of the flow fields. The flow field is obtained by solving the governing equations numerically on sufficiently fine grids so that all the flow details in the liquid turbulence or the bubble-induced turbulence in the laminar flow are fully resolved. DNS coupled with interface tracking method (ITM) has emerged as a reliable tool for engineers and scientists, providing valuable information on the temporal and spatial distribution of key flow variables in the two-phase flow fields [79, 80]. Although existing DNS codes can be applied with confidence to solve a variety of single-phase flow problems, considerable research efforts are still necessary to investigate the gas-liquid two-phase flows with the same level of confidence. Detailed knowledge on the behavior of single bubble or droplet in complex flow fields is still limited. For example, even the behavior of a single air bubble rising in quiescent water is not yet completely understood: not only the physical properties like the density, viscosity, and surface tension [2, 8] affect the behavior of the bubbles, but also small amounts of surface impurities [81]. The information gained by DNS can be employed to improve our understanding on the single bubble behavior and developing closure relations in the framework of E-E computations which allow simulate much larger engineering configurations.

For the E-E approach, the equations of the two-fluid model are derived by ensemble-averaging the local instantaneous equations. The governing mass conservation equations for adiabatic, incompressible, multiphase flow in the vector form for N_p phases are [34, 36]:

$$\frac{\partial}{\partial t}\alpha_k\rho_k + \nabla\cdot\alpha_k\rho_k\overrightarrow{V_k} = \sum_{j=1}^{N_p}\left(\dot{m}_{kj} - \dot{m}_{jk}\right) + \alpha_k S_k \qquad (6)$$

where α_k is the volume fraction of phase-k, ρ_k is the density of phase-k, $\overrightarrow{V_k}$ is the velocity vector, and S_k is the source term. $\dot{m}_{kj}$ and $\dot{m}_{jk}$ describe the mass transfer terms from phase k to phase j and from phase j to phase k, respectively.

The right hand side of the continuity equation describes mass transfer from phase k to phase j as well as vice versa and includes the additional source terms. Since our studies focus on the bubble-induced turbulence from a single bubble without evaporation or condensation, we neglect mass transfer and source terms. Thus it is simplified as

$$\frac{\partial}{\partial t}\alpha_k\rho_k + \nabla\cdot\alpha_k\rho_k\overrightarrow{V_k} = 0 \qquad (7)$$

The momentum equation is

$$\frac{\partial}{\partial \mathrm{t}}\alpha_k\rho_k\overrightarrow{V_k} + \nabla\cdot\alpha_k\rho_k\overrightarrow{V_k}\overrightarrow{V_k} = -\alpha_k\nabla p_k + \nabla\cdot[\alpha_k(\tau_k + \tau_k^T)] + \alpha_k\rho_k g_k + M_k \qquad (8)$$

where τ_k is the shear stress tensor, p_{ki} is the interfacial pressure and M_k is the interfacial forces. Note that one should solve separate set of continuity and momentum equations for each phase along with the following condition: $\sum_{k=1}^{N}\alpha_k = 1$.

Turbulence is taken into consideration in the continuous liquid phase. The velocity field inside the dispersed gas phase has little effect on the overall mixture dynamics due to the relatively small gas density, thus the turbulent kinetic energy inside the bubble is not under consideration for the momentum equation. However, the disperse gas phase influences the turbulence in the continuous phase by the so called bubble-induced turbulence. The widely

used single-phase standard $k-\varepsilon$ turbulence model [82] is used to model the turbulence phenomena in the continuous phase of the gas-liquid flow. The constants used in $k-\varepsilon$ equation are given in Table 1. The transport equations for the turbulent kinetic energy, k, and the turbulent dissipation rate, ε, are:

$$\frac{\partial}{\partial t}(\alpha_k \rho_k k_k) + \nabla \cdot \left(\alpha_k \rho_k k_k \overrightarrow{V_k}\right) = \nabla \cdot \left[\alpha_k \left(\left(\mu_k + \frac{\mu_k^T}{\sigma_{k_k}}\right) \nabla k_k\right)\right] + \alpha_k P - \alpha_k \rho_k \varepsilon_k + \alpha_k \phi_k \quad (9)$$

$$\frac{\partial}{\partial t}(\alpha_k \rho_k \varepsilon_k) + \nabla \cdot \left(\alpha_k \rho_k \varepsilon_k \overrightarrow{V_k}\right) = \nabla \cdot \left[\alpha_k \left(\left(\mu_k + \frac{\mu_k^T}{\sigma_{\varepsilon_k}}\right) \nabla \varepsilon_k\right)\right] + \alpha_k C_{\varepsilon_1} \frac{\varepsilon_k}{k_k} P - \alpha_k \rho_k C_{\varepsilon 2} \frac{\varepsilon_k}{k_k} + \alpha_k \phi_{\varepsilon_k} \quad (10)$$

where P is the production of the turbulent kinetic energy (TKE) due to shear; ϕ_k and ϕ_ε are the energy contributions from the interaction between the fields.

Table 1. Constants used in the $\boldsymbol{k-\varepsilon}$ model.

C_μ	$C_{\varepsilon 1}$	$C_{\varepsilon 2}$	σ_k	σ_ε	κ
0.09	1.44	1.92	1.0	$\frac{\kappa^2}{C_{\varepsilon 2} - C_{\varepsilon 1}}$	0.4187

The set of transport equations in the $k-\varepsilon$ model are applicable only in the fully turbulent regions (i.e., excluding the narrow viscous region near the wall). As in the single-phase flows, the wall functions were derived for a "wall point" at the edge of the buffer zone, (i.e., y^+=30). The logarithmic velocity profile was assumed to be valid, thus

$$u^+ = \frac{1}{\kappa} ln y^+ + B \quad (11)$$

This is the "log law" of the wall given by von Karman [83]. In the literature, there is some variation in the values ascribed to the log law constants, but generally they are within 5% of

$$\kappa = 0.41, \qquad B = 5.2 \tag{12}$$

In the single-phase $k-\varepsilon$ model, the turbulent viscosity is expressed by

$$\mu_L^t = C_\mu \frac{k_l^2}{\varepsilon_l} \tag{13}$$

When applying LES, the model proposed by Smagorinsky [84] is used to calculate the turbulent viscosity. The turbulent viscosity, i.e., the SGS viscosity, is formulated as follows:

$$\mu_L^t = \rho_l (C_S \Delta)^2 |S| \tag{14}$$

where C_S is a model constant with a value of 0.1 and S is the characteristic filtered rate of strain and $\Delta = \left(\Delta_i \Delta_j \Delta_k\right)^{\frac{1}{3}}$ is the filter width.

When the $k-\varepsilon$ turbulence model is used to evaluate the shear-induced turbulent viscosity, there are two approaches to account for the bubble-induced turbulence. One is to use the standard $k-\varepsilon$ model, i.e., ϕ_k and ϕ_ε are set to zero, while the bubble-induced turbulence is accounted for using the Sato's bubble-induced turbulent viscosity model [72]

$$\mu_{BIT} = \rho_L \alpha_g C_{\mu,BIT} D_b |u_r| \tag{15}$$

The Sato's approach of employing a bubble induced turbulence eddy viscosity is the most straightforward and often gives reasonable prediction of flow fields and void fraction distribution. It should be the most appropriate approach when bubble-induced turbulence is dissipated locally, so that this turbulence does not need to be converted and diffused by being included in the transported quantity k. A drawback of the eddy viscosity approach is that it does not provide a direct means of predicting local turbulence energy. Indeed, if bubble-

induced turbulence is substantially dissipated locally and is of a very different length-scale from shear-induced turbulence, then the eddy viscosity approach could provide advantages over the source term approach.

Another approach to account for the bubble-induced turbulence is to include extra source terms in the turbulence models, that is, the bubble-induced turbulence is implicitly included in Eq. (9) and μ_{BIT} is set to zero.

In the approach of Pfleger and Becker [14], the bubble-induced turbulence are expressed as follows

$$\phi_k = \alpha C_K |M_l^D||u_r| \quad (16)$$

C_K is a constant with the value of 1.44. $|M_l^D||u_r|$ represents the rate of energy input of the bubbles resulting from the interfacial forces and the slip velocity. $\tau_{BIT} = \frac{\varepsilon_l}{k_l}$ represents the time scale for the dissipation of the bubble-induced turbulence.

In the approach of Troshko and Hassan [73], they has the following expressions for the source terms

$$\phi_k = \alpha |M_l^D||u_r| \quad (17)$$

Both models attributed the drag force as the main source of the energy input while they used different characteristic time-scale of the bubble-induced turbulence. Troshko and Hassan used $\tau_{BIT} = \frac{2C_{VM}D}{3C_D|u_r|}$ while Pfleger and Becker adopted $\tau_{BIT} = \frac{\varepsilon_l}{k_l}$. Another expression proposed by Lee [85] and Varaksin and Zaichik [86] is

$$\phi_k = C_p \left(1 + C_D^{\frac{4}{3}}\right) \alpha \frac{|u_r|^3}{D} \quad (18)$$

Here $C_p = 0.25$ for the potential flow around a sphere [34].

These three expression of the bubble-induced turbulence source terms consider the drag force as the energy input of the bubbles. However, several simplifications are involved in the derivation of the source terms: assumptions that the fluctuating motion of the interface is isotropic would not hold for large bubbles (such as spherical cap type) rising under buoyancy; some of the bubble-induced turbulence will clearly immediately dissipated in the bubble boundary layer; bubble-bubble interactions generate turbulence at moderate to high void fraction, but the form of such a source term is not clear.

1.5 Interfacial forces in M-CFD

The past several decades witnessed the development of numerical methods based on the continuum (E-E) and the discrete particle (E-L) approaches to simulate the multiphase flow. In both approaches the momentum exchange between the two phases is accounted by the source term which can be expressed as a superposition of terms representing different physical mechanisms, specifically,

$$M_k = M_k^D + M_k^L + M_k^{VM} + M_k^W + M_k^{TD} \quad (19)$$

where the individual terms on the right hand side are: drag force, lift force, virtual mass force, wall force and turbulent dispersion force, respectively. A correct description of the closure laws is of great importance in the numerical simulation of bubbly flows. Currently, it is generally agreed that the drag force is largely predominant over other distributions, and the lateral distribution of the bubble is tightly associated with the lift force. The accuracy of the

closure relations for the interfacial forces significantly determine the prediction capability of the two-fluid model for the dispersed two-phase flow.

1.5.1 Drag force

In bubbly flow, the drag force plays a significant role on the flow pattern. It determines the gas phase residence time and terminal velocity of the bubbles. The drag force can be expressed as [87]

$$M_l^D = -M_g^D = \frac{1}{8} C_D A''' \rho_l |u_g - u_l| (u_g - u_l) \quad (20)$$

where C_D and A''' are the drag coefficient and the interfacial area density, respectively. The interfacial area density can be determined for large range of the gas volume fraction using the Ishii and Mishima' correlation [88],

$$A''' = \frac{4.5}{D} \frac{\alpha - \alpha_{gs}}{1 - \alpha_{gs}} + \frac{6\alpha_{gs}}{D} \frac{1 - \alpha}{1 - \alpha_{gs}} \quad (21)$$

where α_{gs} is the void fraction in the small bubble region, and $\alpha_{gs} = \alpha$ for spherical bubbles.

Kurul and Podowski [89] recommended the following expression for α_{gs}

$$\alpha_{gs} = \begin{cases} \alpha, & for\ \alpha < 0.25 \\ 0.3929 - 0.5714\alpha, & for\ 0.25 \le \alpha < 0.6 \\ 0.05, & for\ 0.6 \le \alpha \end{cases} \quad (22)$$

For a single bubble, the drag force experienced by the bubble is expressed as

$$F_D = \frac{1}{2} C_D A u_r^2 \rho_l \quad (23)$$

where A is the bubble projected area on the lateral plane.

The origin of the drag force is the resistance experienced by a bubble moving in the liquid. Various drag closure laws have been proposed in the literature over the last few decades. Well-known closure laws include those proposed through the analytical solutions of Hadamard [90] for creeping flow past a spherical gas bubble,

$$C_D = \frac{16}{Re_b} \quad (24)$$

which is valid only for low Re_b, i.e., $Re_b \leq 1$. It assumes that the interface is completely free from surface-active contaminants. Surface-active contaminants may cause marked changes in internal circulation and drag force for a bubble or drop, but the effect on shape is negligible at low Reynolds number.

Moore [91] proposed a correlation for the spherical bubble rising at high Reynolds number ($Re_b \gg 1$) based on the analytical derivation

$$C_D = \frac{48}{Re_b}\left(1 - \frac{2.21}{\sqrt{Re_b}}\right) \quad (25)$$

Various correlations have since been proposed to bridge the gap between these two drag closure laws. One of the most widely accepted correlation is proposed by Tomiyama et al. [1]. This correlation is based on spherical bubbles in pure systems

$$C_D = \min\left[\frac{16}{Re_b}\left(1 + 0.15Re_b^{0.687}\right), \frac{48}{Re_b}\right] \quad (26)$$

Tomiyama et al. [1] also proposed a formula for the drag coefficient, C_D, in a slightly contaminated system as:

$$C_D = \min\left[\frac{24}{Re_b}\left(1 + 0.15Re_b^{0.687}\right), \frac{72}{Re_b}\right] \quad (27)$$

Legendre and Magnaudet [92] pointed out that the presence of liquid velocity gradient increased the drag force acting on a bubble and proposed the following drag multiplier ϕ_{sr}:

$$\phi_{sr} = 1 + 0.55Sr^2 \quad (28)$$

where Sr is the non-dimensional shear rate defined by

$$Sr = \frac{d\omega}{u_r} \quad (29)$$

where ω is the magnitude of the liquid velocity gradient and u_r is the relative velocity between the bubble and the liquid. While this correlation is based on the linear shear flow with a wide range of Reynolds number ($0.1 \leq Re_b \leq 500$) and shear rate ($0 \leq Sr \leq 1$), it is useful to investigate the impact of turbulent shear flow on the correlation.

Bagchi and Balachandar [93] studied the effect of freestream isotropic turbulent flow on the drag and lift forces acting on a spherical particle. Within the range they discussed where the particle Reynolds number is about 60~600 and the freestream turbulence intensity is about 10~20%, they observed that the turbulence does not have a substantial and systematic effect on the time-averaged mean drag and the standard drag correlation results in a reasonably accurate prediction of the mean drag obtained from the DNS.

When we developed the proportional-integral-derivative (PID) based controller to evaluate lift and drag forces in laminar flows, we demonstrated excellent agreement with the drag correlation developed by Tomiyama et al. [1] over a wide range of bubble Reynolds numbers [94]. While the development of closure model for two-phase laminar flow has reached a certain level, more studies and investigations are required for the turbulent flows. In Section 3.3, we want to numerically analyze the influence of turbulent flow on the drag force

experienced by a single bubble and compare its behavior with the laminar flow based on Tomiyama's correlation. A set of parametric studies will be performed to justify the relationship between typical two-phase turbulent flow parameters and drag force.

1.5.2 Lift force

The lift force on the bubble originates from the mean velocity gradient of the liquid phase and relative velocity between the bubble and the liquid phase. It has a significant effect on the lateral gas volume fraction distribution in bubbly flows. Bubbles traveling through a shear flow (such as wall boundary layer) will experience lift force transverse to the direction of motion. Experimental investigations by Tomiyama et al. [68] as well as numerical predictions by Ervin and Tryggvason [18] have shown that the direction of the lift force can change its sign if a substantial deformation of the bubble occurs. Drew and Lahey [95] derived the following expression for the ensemble-averaged interfacial lift force,

$$M_l^L = -M_g^L = C_L \rho_l \alpha_g (u_g - u_l)(\nabla \times u_l) \quad (30)$$

where C_L is the lift coefficient.

In plane shear flow, the lift force exerted on the single bubble is typically modeled as

$$F_L = -C_L \rho_l u_r \frac{\partial u}{\partial y} V_b \quad (31)$$

Lift force governs the transverse migration direction of bubbles in the liquid. The magnitude and direction of the lift force is related to the bubble characteristics, such as size and deformability as wells as liquid flow characteristics. The key factors influencing the lift coefficient are the bubble Reynolds number, shear rate and the bubble deformability. Earlier

experimental research in two-phase upflow [2] observed that small bubbles tend to migrate toward the pipe wall, causing a wall-peak bubble distribution, whereas large bubbles tend to migrate toward the pipe center, resulting in a core-peak bubble distribution. For a spherical bubble in upflow, the shear lift coefficient C_L is positive so that the lift force acts (Eq.(31)) in the direction of decreasing liquid velocity, i.e. in the direction towards the channel wall.

Legendre and Magnaudet [92] investigated the lift force experienced by the spherical bubble over a wide range of bubble Reynolds number ($0.1 \leq Re_b \leq 500$) and shear rate ($0 \leq Sr \leq 1$) and proposed the following lift coefficient model

$$C_L = \sqrt{\left(\frac{6}{\pi^2}\frac{2.255}{(Re_b Sr)^{0.5}\left(1+\frac{0.2Re_b}{Sr}\right)^{1.5}}\right)^2 + \left(\frac{1}{2}\frac{1+\frac{16}{Re_b}}{1+\frac{29}{Re_b}}\right)^2} \qquad (32)$$

They observed that when the shear rate increases, i.e. $Sr = O(1)$, a small but consistent decrease of the lift coefficient occurs while a very significant increase of the drag coefficient, essentially produced by the modifications of the pressure distribution, is observed.

While Legendre and Magnaudet's closure model is valid over the range they discussed, they did not consider the impact of bubble deformation on the lift coefficient which is more important for the practical applications. One of the important experimental research efforts on the lift force evaluation has been carried out by Tomiyama et al. [2] who used a linear shear velocity field in viscous liquids. The following dimensionless numbers were used to describe the bubble characteristics in the experiment: Morton number (Mo) characterizing the shape of bubbles in a surrounding fluid or continuous phase; Eotvos number (Eo) defining the ratio of

buoyancy to surface tension forces, and the velocity gradient, ω, of a simple shear flow. These are defined as

$$Mo = \frac{g(\rho_l - \rho_g)\mu_l^4}{\rho_l^2 \sigma^3} \quad (33)$$

$$Eo = \frac{g(\rho_l - \rho_g)D^2}{\sigma} \quad (34)$$

$$\omega = |\frac{du_l}{dy}| \quad (35)$$

The experiments [2] varied these parameters within the ranges of $-5.5 \leq \log_{10} Mo \leq -2.8$, $1.39 \leq Eo \leq 5.74$, and $0 \leq \omega \leq 8.3\ s^{-1}$. The closure law for the lift coefficient proposed by Tomiyama is based on the modified Eotvos number given as:

$$C_L = \begin{cases} \min\left(0.288\tanh(0.121Re_b), f(Eo_H)\right), & Eo_H < 4 \\ f(Eo_H) = 0.00105Eo_H^3 - 0.0159Eo_H^2 - 0.0204Eo_H + 0.474, & 4 \leq Eo_H < 10.7 \end{cases} \quad (36)$$

$$Eo_H = \frac{g(\rho_L - \rho_G)D_H^2}{\sigma} \quad (37)$$

where D_H is the extended bubble diameter and it is defined as the maximum horizontal dimension of a bubble shown in Figure 2. In Eq.(34), D is the spherical bubble diameter. In Eq. (36), Tomiyama et. al. [2] use modified Eotvos number, Eo_H, for deformable bubble and replace spherical bubble diameter with extended bubble diameter, D_H, in their study. Figure 2 shows a schematic illustrating the difference between spherical bubble diameter and extended bubble diameter and the spherical and deformable bubble migration direction in laminar shear upflow.

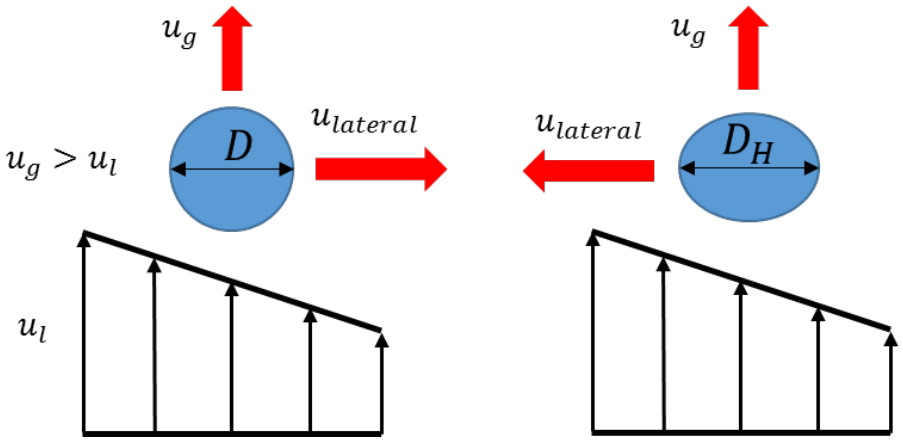

Figure 2. Illustration of the migration direction for spherical and deformable bubble. $u_{lateral}$ represents the lateral migration velocity of the bubble, u_g and u_l represent the streamwise velocity of the bubble and liquid, respectively.

Dijkhuizen et al. [8] did both numerical and experimental investigation on the lift force acting on the single bubble and found that for the spherical bubble, the numerical simulation using front tracking method agreed well with the correlation presented by Legendre and Magnaudet [92]. For large deformable bubbles, a good agreement with the correlation proposed by Tomiyama et al. [2] was found over a wide range of liquid viscosities. However, the experimental results were quite different from Tomiyama's results. Dijkhuizen et al. attributed those differences to the effect of contamination in the liquid [8].

1.5.3 Virtual mass force

The third term in Eq. (19) represents the virtual mass force, which comes into play when one phase is accelerating relative to the other one. Virtual mass or added mass is the inertia added to the system because an accelerating or decelerating body must move some

volume of surrounding fluid as it moves through it. In the case of a bubble accelerating in a continuous liquid phase, this force can be described by the following expression [96, 97]:

$$M_l^{VM} = -M_g^{VM} = C_{VM}\alpha_g\rho_l[\frac{D_l u_l}{Dt} - \frac{D_g u_g}{Dt}] \quad (38)$$

where C_{VM} is the virtual mass coefficient, which for a spherical particle is typically assumed to be 0.5 [98].

1.5.4 Wall force

The term M_K^W represents the wall force. When the bubbles migrate toward the wall, the bubble rise velocity and void fraction distribution are affected by the solid boundary presence. The wall-induced force, often simply referred as wall force, makes the interfacial force closures model more complex. The near wall behavior and bubble distribution play an important role in the multiphase flow. Therefore, it is important to understand the motion of bubbles near the wall, and moreover, to understand the hydrodynamic forces acting on the bubbles.

Antal et al. [67] proposed the wall force model based on a potential flow past two cylinders

$$F_L^W = \frac{2}{D}\left[C_{W1} + C_{W2}\left(\frac{D}{2x}\right)\right]\rho_l u_r^2 \boldsymbol{n} \quad (39)$$

where x is the distance between the bubble center and the wall, $\boldsymbol{n}$ is the unit vector normal to the wall, C_{W1} and C_{W2} are the wall force coefficients:

$$C_{W1} = -0.06v_r - 0.104 \quad (40)$$

$$C_{W2} = 0.147 \quad (41)$$

Tomiyama et al. [68] pointed out that the coefficient C_{W2} in Antal's model vanishes for bubbles in two parallel walls and modified the Antal's model by introducing the second term with respect to $D/2x$. By measuring the trajectories of single bubble rising in glycerol-water solution ($\log_{10} Mo = -2.8$), they confirmed that the value of C_{W2} was zero and proposed the following wall force model

$$F_W = \frac{2}{D} C_{W3} \left(\frac{D}{2x}\right)^2 \rho_l u_r^2 \boldsymbol{n} \qquad (42)$$

Under a constant Morton number, the coefficient C_{W3} should be a function of the Eotvos number, Eo, and deducted the following empirical correlation of C_{W3}:

$$C_{W3} = \begin{cases} \exp(-0.933Eo + 1.79), & for 1 \le Eo \le 5 \\ 0.007Eo + 0.04, & for\ 5 < Eo \le 33 \end{cases} \qquad (43)$$

Hosokawa et al. [74] extended the study of the Tomiyama et al. [68] and claimed that C_{W3} is not only a function of bubble deformation but also the bubble Reynolds number Re_b. They proposed the following correlation of C_{W3} for $Re_b < 10$ under the condition of $-6 \le \log_{10} Mo \le -2.5$ and $2.0 \le Eo \le 10.0$.

$$C_{W3} = max\left\{\frac{7}{Re_b^{1.9}}, 0.0217Eo\right\} \qquad (44)$$

It is important to investigate the combined effects of lift and wall forces. The modeling work of Jiao and Podowski [99] revealed that the bubble motion is not constrained by the wall force when the distance from the walls is larger than the bubble diameter. Shaver et al. [100] proposed a modification to the lift coefficient based on the distance from the wall given in Eq. (45) and suggested using modified lift force near the wall instead of using wall force.

$$C_L^{\mathrm{D}} = \begin{cases} 0, & \text{for } \frac{y}{D} < \frac{1}{2} \\ C_L\left(3\left(\frac{2y}{D}-1\right)^2 - 2\left(\frac{2y}{D}-1\right)^3\right), & \text{for } \frac{1}{2} \le \frac{y}{D} \le 1 \\ C_L, & \text{for } 1 < \frac{y}{D} \end{cases} \quad (45)$$

where C_L^D is the modified lift coefficient, C_L is the nominal lift coefficient and is determined in the usual manner, *y* is the bubble distance from the wall and *D* is the bubble diameter.

Sugioka and Tsukada [101] observed that the direction of net transverse lift force near the wall changes at bubble Reynolds number of 30. Takemura and Magnaudet [102] had similar observation that the lift force acting on clean bubble is directed away from the wall force with $Re_b < 35$ and toward it for higher Re_b while the contaminated bubbles are always repelled by the wall. Our study revealed that the interfacial forces acting on the bubble near the wall are a coupled phenomenon of Re_b and bubble deformation level. A comprehensive map of lift coefficient versus bubble Reynolds number and deformation level is shown in Figure 41 which displays the bubble transverse migration direction and complements the current database of wall effect on the interfacial forces.

Additionally, the current study on the effect of the wall presence on the interfacial forces focuses on the influence of the transverse migration. Limited work [101] has been reported about the wall effect on the drag force which will determine the bubble residence time and terminal velocity. The PID bubble controller enables us to extract the transverse force experienced by the bubble which incorporate both lift force and wall force. The total transverse force, F_T, can be expressed as follows

$$F_T = -C_T V_b u_r \frac{\partial u}{\partial y}\rho_l = F_L + F_W \quad (46)$$

where C_T is the net transverse lift coefficient.

1.5.5 Turbulent dispersion force

The last term in Eq. (19) is the turbulent dispersion force. The turbulent dispersion force is defined when the turbulent liquid velocity field have a direct effect on bubble behavior. The turbulent dispersion force models this effect. Lift force, turbulent dispersion force and wall force act in the transverse (normal to the wall) direction. Their actions on the bubbles are as follows: the wall force drives the bubbles away from the wall, the lift force either push them toward the wall or pull them away from the wall depending on the flow properties and the turbulent dispersion force tends to smooth out the void fraction gradient. The expression of the turbulent dispersion force is proposed by Lahey et al. [71]:

$$M_l^{TD} = -M_g^{TD} = -C_{TD}\rho_l k_l \nabla \alpha_g \qquad (47)$$

where k_l is the turbulent kinetic energy of the continuous phase. The turbulent dispersion coefficient, C_{TD}, for bubbly two-phase flow was 0.1 [71]. Further work revealed that the turbulent dispersion coefficient varies from 0 to 0.5 depending on the operational conditions [103].

1.6 Wall effect on interfacial forces and BIT

The fundamental understanding of the wall presence effect on the bubble-induced turbulence production as well as the interfacial closures has not been fully developed. The bubble rise velocity and bubble volume fraction (or void fraction) distribution is influenced by the presence of solid boundaries. The physics behind the bubbly flows behavior near the wall

can be very complex due to the various parameters and phenomena involved, such as surface contamination [102], bubble deformation, relative velocity and wall distance. Numerous experimental and analytical work [97, 104-109] have reported on the interfacial forces acting on the solid sphere while only a few studies analyze the bubbles' motion near the wall. Antal et al. [67] proposed the first wall force model based on the theoretical derivation for the flow past two cylinders. The void fraction distribution and liquid velocity profile agreed quite well with the trends found experimentally [110, 111] while the prediction of zero void fraction positions are different. Takemura et al. [102, 112] experimentally investigated the spherical bubble rising near a plane vertical wall in a quiescent liquid with different bubble Reynolds numbers, Re_b. They found that at low Re_b(<35), the net transverse lift force acting on the bubble was directed away from the wall and it can be solved analytically based on the Oseen approximation [106]. However, for higher Re_b, the bubble tends to migrate toward the wall. They explained that the distribution of the vorticity around the bubble is responsible for the weak interactions observed for Reynolds numbers of $O(10)$. For the high enough Reynolds numbers where the inertia effects are dominant, the interaction with the wall results in an attractive lift force. The bouncing process of the bubbles moving sufficiently close to the wall, at high Re_b, may be due to the competition between these two mechanisms.

In addition to the experimental studies, the rapid growth of computer power and advanced numerical algorithms make CFD become an important role in multiphase simulation. Sugioka and Tsukada [101] conducted drag and lift analysis on the spherical bubbles rising near a wall and found that an increase in drag force is always obtained due to the bubble-wall interaction. The increase in drag coefficient was found to be inversely proportional to the

distance from the wall. On the other hand, the direction of the lift force is highly dependent on the distance between the bubble and the wall as well as the bubble Reynolds number. At low values of bubble Reynolds number ($Re_b \leq 30$), the bubbles tend to move away from the wall, whereas bubbles with higher values of Reynolds numbers ($Re_b \geq 100$) tend to move towards the wall at $0.62 \leq \frac{L}{D} \leq 3.0$. At the same time, at smaller values of bubble-to-wall distance $\left(\frac{L}{D} < 0.62\right)$, the bubbles tend to attain a positive lift force and move away from the wall. This direction change in the lift force causes the bouncing motion of the bubbles as reported by [102]. Sugioka and Tsukada [101] attributed these changes in the direction of the lift force towards the contribution of two competing forces, a repulsive force due to asymmetric distributions of the vorticity in the presence of the wall, and an attractive force due to the accelerated irrotational flow in the gap between the bubble and the wall. In their study [101], it was assumed that the bubble shapes are rigid and spherical which is not possible in the realistic situations. Zeng et al. [113, 114] carried out DNS for a rigid sphere moving parallel to a plane wall in a quiescent fluid for $Re_b < 300$ using a spectral element method. They revealed that the lift coefficient decreases with both the Re_b and the distance from the wall for $Re_b \leq 100$. However, the lift coefficient increases dramatically for increasing Re_b when $Re_b > 100$. Zaruba et al. [115] numerically investigated the motion of single bubble rising in upward shear liquid flow in the vicinity of a vertical wall. Bubbles were found to slide along the wall when their diameter is small. Bubbles could also experience multiple collisions with the wall at certain experimental parameters. Vhora et al. [116] investigated the lift and wall force balance using DNS coupled with interface tracking method. A spherical bubble was

initially released with different inclination angles and migrated towards the wall. Due to the force balance between wall repulsive force and lift force, the bubble reached a steady state and stayed at a fixed position away from the wall. The bubble' trajectories agree with the experimental results. Lucas et al.[117] performed the full 3D simulations using the commercial code CFX for simplified monodisperse cases. In the validation of different models for the interfacial forces, a set of Tomiyama's lift [2] and wall force [118] and Favre averaged turbulent dispersion force [119] was found to provide the best agreement with the experimental data.

Zhang et al. [120] conducted some studies on the interaction between the wall-induced and bubble-induced turbulence in the upward turbulent bubbly flow near the wall. They observed that the existence of a wall could suppress the bubble-induced turbulence given the same void fraction and the existence of bubbles could also suppress the solely wall-induced turbulence as compared to the single-phase turbulent flow, even though the total turbulence is enhanced. They attributed the first turbulence reducing effect to the elongation of the bubble and the suppression of bubble wake by the wall. This is consistent with the observations that the stronger bubble-induced turbulence is generated in the duct center of larger ducts, as compared to that in small ducts. While for the second turbulence reducing effect with small bubbles or low void fraction scenarios, two factors contribute to it: (a) large velocity fluctuation gradient near the bubble interface which increases the turbulent energy dissipation; (b) an energy dumping effect due to the bubble deformation. For the cases with relatively larger bubble size and high void fractions, two mechanisms may be responsible which are the flow acceleration laminarization by bubbles and the suppression of the coherent structures. For the

single-phase flow, the “bursting event” of the coherent structures is the key process for the turbulence energy generation near the wall. However, the passing-by of the bubbles breaks these structures by hitting their heads or trapping them in the bubble’s wake and then suppressing the source of the wall-induced turbulence. While their work provided a conceptual theory for the interaction between the wall-induced turbulence and bubble-induced turbulence, the models of the mechanism are lacking for now.

Reboux and Lakehal [121] analyzed the interactions between the bubbles and the liquid through in-depth analysis of the turbulence statistics. They found that the near-wall flow is affected by the bubbles. The coherent structures are different in shape than in single-phase flow, featuring less elongated, broken structures. The decay in the energy spectra near the wall was found to be significantly slower (slope of -3) for the bubbly flow than for a single-phase flow (slope of -6).

The source of energy for turbulence generation in single-phase flows is the mean velocity shear (turbulence production). Away from the walls the energy usually delivered through the turbulence diffusion from the near wall regions since the local shear is relatively small. However, the local shear effect on the bubble induced turbulence production has not been investigated.

The flow direction relative to the buoyancy force plays an important role on the bubble distribution in the channel. For spherical bubbles, the upflow of the liquid results in wall-peaking void fraction distribution, while the downflow in center-peaked profile, as was shown in experimental observation [17]. It would be interesting to investigate how the reversal in flow direction influences the amount of energy transfer from a bubble train utilizing a periodic

domain. The major difference in the two flow patterns is the switch of the direction of wall shear gradients relative to the velocity gradient generated by the liquid flow around the bubble. The amount of energy transferred between the bubble and the liquid turbulence may depend not only on the bubble size and relative velocity, but also on the energy already present in the liquid. Those unsolved issues are crucial for the development of two phase model.

1.7 Bubble-induced turbulence theory

As mentioned above, the turbulence energy spectrum is considered to follow the Richardson's [57] description in the single phase flow. Large scale eddies are generated due to local velocity gradient and the mean flow kinetic energy is converted into turbulent kinetic energy as turbulent fluctuations develop. However, the production of the turbulence energy in gas-liquid two-phase flow is more complex. Because the turbulent structures are formed by the breakage of larger structures (like in single-phase flow) as well as a parallel mechanism of structure formation because of the bubbles' presence on a variety of scales. Such a multiple mechanism of turbulent structures formation is expected to give an energy spectrum having characteristic features different from the single-phase energy spectrum.

The bubble and liquid turbulence interaction is a coupled phenomenon where the presence of bubbles modifies the turbulence [16, 53] while the turbulence influences the bubble distribution [35]. Bubble motion and turbulent intensity have a strong effect on fluid mixing, which is an important parameter when studying boiling heat transfer, chemical reaction rates and other phenomena. The fundamental understanding of these interactions to support the CFD modeling is very important for practical applications.

1.7.1 Experimental work

In 1975, Serizawa et al. published three papers [122-124] which opened the door for the experimental measurement of the two-phase turbulent field. The first paper [124] described the developed electronic instrumentation, i.e. electric resistivity probe, for the measurement of bubble size and velocity distribution. The second paper [123] talked about the statistical analysis of two-phase bubbly flow in a vertical pipe. In the near-wall region, a maximum void fraction was observed. The spectrum of the bubble's velocity showed a Poisson distribution while the liquid velocity was found to follow normal distribution shown in Figure 3. Serizawa et al. observed an important phenomenon that the turbulent intensity would decrease first with increasing gas flow rate for constant water velocity and then increase again with a further increase in the gas flow rate. This phenomenon was more significant for a higher liquid Reynolds number. The influence of the dispersed phase (bubbles, drops or particles) on the continuous phase, especially whether the dispersed phase is a turbulence enhancer or dampener, became a topic which many researchers focused on in the past few decades. Shawkat et al. [125] observed that when the bubbles are introduced into the flow, there is a general increase in the turbulent intensity. However, the gas bubbles suppress the turbulence close to the wall in very low void fraction flows (less than 1.6%). At superficial liquid velocity, J_f, of 0.58 and 0.68 m/s and superficial gas velocity, J_g, of 0.015 m/s, a turbulence suppression relative to the single-phase flow is observed near the wall. The magnitude of the suppression increases with superficial liquid velocity. A review paper from Hetsroni [126] on particle-fluid systems concluded that the presence of particles with a lower particle Reynolds number ($Re_p =$

$\frac{\rho D_p u_r}{\mu} < 40$) tends to suppress the turbulence of the continuous carrier fluid while particles with high particle Reynolds number ($Re_p > 400$) tends to enhance the turbulence of the fluid motion. Gore and Crowe [127] proposed the ratio of particle diameter to the turbulent length scale, $\frac{D}{\lambda} \cong 0.1$, to determine whether the turbulent intensity would be increased or decreased by the addition of particles. Similar systematic, comprehensive and quantitative study is not available for gas-liquid dispersion. Serizawa et al. [122] showed that the turbulent velocity components of the liquid phase play a predominant role in the turbulent transport process due to the high liquid density compared to gas density. A bubble diffusion model appears to be applicable for describing the turbulent transport of bubbles in stationary water in a pool and air-water two-phase bubbly flow in a pipe.

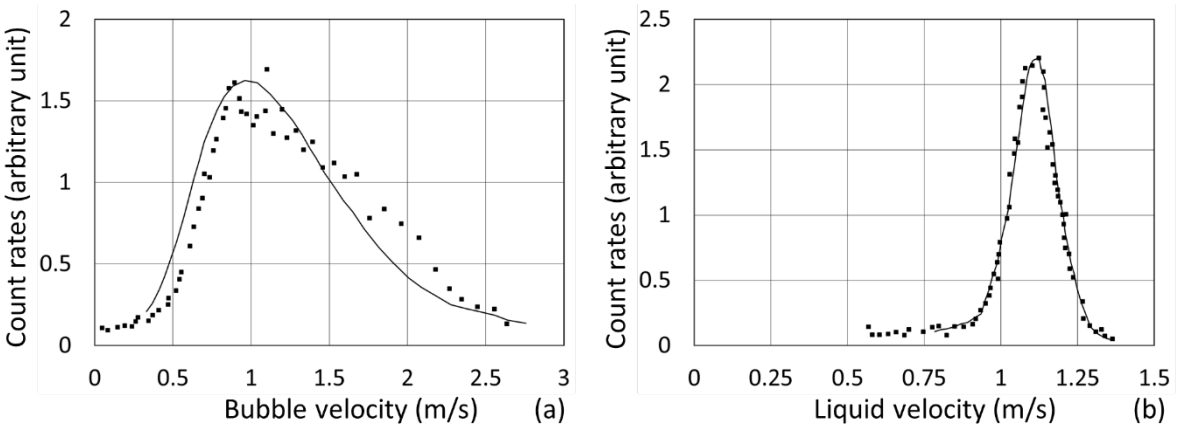

Figure 3. Comparison of bubble and liquid velocity distributions in Serizawa's experiment [123].

A few years later, Serizawa and Kataoka [128] revealed that the diffusion of turbulence eddies and the dumping effect of bubbles may be the main mechanism responsible for the turbulent intensity reduction. They provided a physical explanation and interpretation of the interchange mechanism between the turbulence kinetic energy and interfacial energy.

However, a quantitative evaluation of each mechanism's contribution to the turbulence reduction is still very difficult. At the same time, Kataoka and Serizawa [13] suggested that the liquid turbulence production in two-phase flow is governed by two terms; namely the production due to the shear stress ($\rho_l(1-\alpha)\overline{u'v'}\frac{\partial u}{\partial r}$) and a bubble-induced generation term due to the relative velocity between the bubbles and the liquid.

Sato et al. [10, 129] proposed a well-known theory to describe the transfer process of momentum and heat in two-phase bubbly channel flows. For single-phase turbulent flow, the momentum transfer is decided by molecular dynamic viscosity μ_l and turbulent viscosity μ_t. In the presence of the gas phase, additional turbulence is generated and a bubble-induced turbulence eddy viscosity μ_{BIT} is introduced in the momentum transfer to model this. Based on his theory, the velocity profile and the frictional pressure gradient for a given flow can be predicted when its void fraction profile is known. Sato et al. proposed the following equation for μ_{BIT}:

$$\mu_{BIT} = C_B \rho_l \alpha D |u_g - u_l| \qquad (48)$$

Sato et al. tuned the value of constant C_B to satisfy their own measured velocity profile. Sato has recommended a value of 0.6 for C_B. Using this value of constant, the predicted values of wall shear stress agreed with the experimental measurement.

Michiyoshi and Serizawa [130] presented the two-dimensional turbulence measurements in air-water bubbly flow in a pipe with improved techniques, a dual-sensor hot-film anemometry. They observed the bubble-induced turbulence to be roughly isotropic. The effect of bubble-induced velocity fluctuations has been discussed based on the turbulence

intensity measurements and was found to increase as a 0.8 power of the void fraction. The measured turbulent shear stress showed the highest values in the wall proximity, corresponding to the maximum in the gas volume fraction profile.

The experimental work of Lance and Bataille [16] can be considered as a landmark contribution for the bubble-induced turbulence research. They studied the characteristics of liquid phase turbulence in a bubbly, grid generated nearly uniform turbulent flow field. The authors made turbulence measurements in a hydrodynamic tunnel using hot-film anemometer and laser-Doppler anemometer. It was observed that, except near the walls, the local void fraction, the mean liquid velocity and the turbulence intensity were practically uniform (within 10%) in the spanwise direction, as was intended in the experiment design. The single phase grid generated turbulence was isotropic and even remained isotropic in the presence of bubbles. The observations of isotropic turbulence are similar to those made by Theofanous and Sullivan [131] and Drew and Lahey [96].

One of the important observations of Lance and Bataille [16] was regarding the excess turbulent kinetic energy ($u_E'^{\,2} = u'^2 - u_o'^2$, where u'^2 and $u_0'^2$ are the streamwise component of the turbulent kinetic energies in the presence and absence of bubbles, respectively). The authors conclude that the value of $u_E'^{\,2}/u_r^2$ was found to be function of only α and u_o'/u_r. While they did not consider the bubble deformability, they did get some valuable conclusions. The value of $u_E'^2/u_r^2$ varied linearly with α when the later, u_o'/u_r, was less than 1%. In addition, the kinetic energy in the liquid is a superposition of the turbulent energy in the absence of bubbles (created by the grids) and that generated by the bubbles. Such a decomposition is not true when $\alpha > 1\%$ because of the existence of large scale fluctuations.

Beyond α of 1%, ${u'_E}^2/u_r^2$ was found to depend strongly on u'_0/u_r. Tsuji et al. [132] found that the neighboring spherical particles can interact only when the distance between them is less than five particle diameters. Such a geometric arrangement gives dispersed phase void fraction to be about 1%. Except the near wall region, the concentration of the bubbles are uniform in the transverse direction in this experiment by design. Above this void fraction, bubbles may have non-uniform distribution which result into local pressure gradients and hence large-scale structures. One more important observation of the authors was that the contribution of the wakes to the turbulent kinetic energy remains small compared to the overall turbulent kinetic energy observed in the flow.

Lance and Bataille [16] also examined the turbulent energy spectrum. Compared to the single-phase flow, it was observed that the turbulent kinetic energy of the liquid in two-phase bubbly flow is distributed over a significantly wider range of wave numbers. The minimum value of the velocity fluctuation spectrum, $\frac{E_{11}}{u_l^2}$, decreased from 10^{-6} to near 10^{-7}. Accordingly, the associated Taylor and Kolmogorov scales are much smaller than the corresponding single phase length scales. The existence of bubbles breaks up the continuous liquid eddies. Further, the classical -5/3 power law for the inertial range of turbulent single-phase flow is progressively replaced by another power law of exponent equal to -8/3 when the void fraction increases for given value of u'_o/u_r. This particular observation has become very important in understanding of the turbulence in two-phase flows.

Mudde et al. [133] observed the slope of -5/3 is over a wide range of void fraction, 0.0% ~ 25%, and in three columns of practical interest where the pipe diameters are 152, 234,

and 384 mm. All columns were filled with tap water and homogeneously aerated via a sintered polyethylene porous plate which generated bubbles with an equivalent diameter of 3mm. Rensen et al. [134] carried out careful hot-film anemometry measurements in a fully developed two-phase turbulent flow. They rationalized the behavior of slope based on the bubblance parameter which is defined as the ratio between the energy added to the liquid flow by the bubbles and the initial single-phase turbulence energy, $b = \frac{1}{2}\alpha u_r^2 / u_0'^2$. They argued that the slope of -8/3 is found only when the energy associated with the perturbations of liquid (in the absence of bubbles) is greater than the energy associated with bubble generated turbulence (i.e. $b > 1$). Later similar observations have been made by Mendez-Diaz et al. [135] and Bouche et al. [136-138] who have reported slopes close to -8/3 and in the range of -8/3 to -3. Generally, it may be concluded that a slope of -5/3 is observed when the gas-liquid dispersion is homogeneous and close to -3 when it is heterogeneous.

1.7.2 Numerical simulations

The rapid advancement in high-performance computing (HPC) and direct numerical simulation (DNS) coupled with interface tracking methods (ITMs) provided reliable analysis tool for the two-phase flow high-fidelity modeling. Bunner and Tryggvason [23] performed a 3D DNS of 27 deformable bubbles ($Eo = 5$) rising in a periodic domain. They found a -3.6 slope in the dissipation region which is very close to -11/3 slope. They also compared the results for the deformable bubbles with the nearly spherical bubbles, $Eo = 1$, in order to compare the effect of deformation on the interaction of the bubbles. The spectra are similar at high wavenumber while in the low wavenumber region are quite different. Note that in the low

wavenumber region the spectrum is determined by the interactions between the bubbles and the collective structures that they form. Since these structures were shown to be qualitatively different, it is reasonable to see differences in the spectrum at low wavenumber. In the high wavenumber region the spectrum corresponds to velocity fluctuations on length scales smaller than the bubble diameter and is therefore determined primarily by the structure of the flow around individual bubbles, particularly in the bubble wake. The structures of the flow around the bubbles for different bubble deformation levels are basically the same, so the spectra at high wavenumbers are approximately the same.

Later research efforts [41] revealed that Lance and Bataille [16] had a slope between -8/3 and -11/3 in the high wavenumber dissipation range. Although this has been the general observation, there are no studies which clearly understand the turbulence characteristics of the two regimes. More advanced numerical methods, like DNS, can help us improve our understanding in this direction.

Bolotnov et al. [139] has proposed a spectral turbulence cascade-transport model, which tracks the evolution of the turbulent kinetic energy from large to small liquid eddies, for the analysis of the homogeneous decay of isotropic single and bubbly two-phase turbulence. This model has been validated for the decay of homogeneous, isotropic single and two-phase bubbly flow turbulence. The Reynolds number of the data based on bubble diameter and relative velocity is appropriately 1400. Spectral analysis of turbulent single-phase and two-phase DNS data in flat plane channel, circular pipe, and reactor subchannel geometries conducted by Brown and Bolotnov [140] showed that the energy spectrum has a power law

scaling close to -3 for the two-phase flow case, regardless of geometry, while the single-phase turbulent DNS data for each geometry showed the traditional -5/3 power law.

Previously researchers considered the liquid energy balance and assumed that the work performed by the bubble's relative motion to the liquid is transferred to the energy of turbulence. It was also hypothesized that the liquid eddies gaining the most from the bubble's energy are the same size as the bubble [16]. However, there is little experimental evidence to support those hypotheses [139]. The presented research will help us understand the energy exchange through a detailed analysis of single-bubble behavior.

1.8 Influence of the BIT on the interfacial forces

The concept of interfacial forces was introduced to mechanistically model the bubble distribution in M-CFD. The lateral distribution of bubbles is classically modeled by lift, wall and turbulent dispersion forces. However, the drag and lift models have not considered the explicit influence of the bubble-induced turbulence on the interfacial forces. To further understand the hydrodynamics of turbulent two-phase flows, the influence of turbulence on the dynamics and wake of a bubble, and vice versa, needs to be clarified.

The effect of the turbulent field on the drag and lift forces experienced by an isolated spherical bubble will be presented as follows. Bagchi and Balachandar [93] did some studies on the effect of isotropic turbulent flow with strong turbulent intensity ($\approx$10~25%) on the drag and lift forces on a spherical particle. It was shown that the mean drag force experienced by the sphere was well-predicted by a standard drag correlation [108] that is applicable for a spherical particle in a laminar environment. Merle et al. [141] performed a LES of a fixed

spherical bubble ($Re_b = 500$, based on the bubble diameter and centerline velocity in the pipe) in a turbulent pipe flow ($Re = 6000$, based on the pipe diameter and bulk velocity) with smaller turbulent intensity, approximately 6.4%. They observed that the interfacial forces were found to be affected by all of the length scales of the turbulent fields. The drag force was found to conform to the drag closure proposed by Moore [91] whereas the lift force could be predicted through the closure law of Drew and Lahey [66], similar to the case of a bubble in a laminar flow field. Their findings confirmed the observations of Bagchi and Balachandar [93].

The development of vorticity at the interface of rising bubbles influences the wake formation behind them and their path instabilities. Bubbles with open, turbulent and unsteady wakes tend to attain significant helical or zigzagging movements throughout their rise path through the fluid, with significant oscillations in the shapes of the bubbles. It has previously been noted that these oscillations in both shape and rise path tend to 'distribute' the kinetic energy through the wake of the bubble [142]. Subsequent bubbles rising in the paths of these bubbles would therefore experience some velocity disturbances, thus compounding the shape and path oscillations and velocity fluctuations in the swarm.

The development of vorticity and wake structure around rising bubbles also influences the stability of the rise paths of the bubbles and their interaction with each other in cases of multiple bubble systems. In turn, these phenomena highly influence the tendencies of bubbles to converge and collide with each other. It has been previously noted that the collision of bubbles can contribute greatly towards the amplification of turbulent energy production in a multiple bubble system [22]. Saffman [143] studied zigzagging and spiraling bubbles and concluded that the zigzag motion is possibly related to an oscillation of the wake or a periodic

discharge of vorticity from the bubble. The interaction of bubbles and their tendency to either collide and repel or coalesce is therefore highly important towards the understanding of turbulence in bubble columns.

1.9 Dissertation overview

The dissertation is structured as follows. Chapter 2 describes the numerical method and provides the information of the DNS flow solver, level-set interface tracking method, PID bubble controller, block-induced turbulence generation algorithm and parallel transient boundary conditions (BCT) computing capability. They are the basis of the presented research. Chapter 3 shows the results of the interfacial forces evaluation in both laminar and turbulent flow fields. The level-set interface tracking method is validated and verified against the experimental results. The research scope include the lift force in laminar shear flow field, wall effect on the interfacial forces, and the drag force in homogeneous turbulent flow field. The research work presented in Chapter 3 has been already published in [56, 94, 144]. Chapter 4 evaluates the bubble-induced turbulence under the homogeneous turbulent flow field. It helps to understand the kinetic energy transfer between a single bubble and surrounding liquid turbulence. The bubble-induced turbulence will switch from the energy sink to the energy source as the bubble becomes more deformable. Those research efforts have been published in [79, 80]. Chapter 5 provides the results of the single-phase shear turbulent flow range from ~10 s^{-1} to ~10^3 s^{-1}. The approach to generate self-sustained shear turbulent flow is reported in [145]. The shear rate near the wall is up to ~1300 s^{-1} which is desirable to simulate the reactor subchannel conditions. The shear rate in the domain center is as low as 13 s^{-1} with turbulent

intensity of 9%. Those preliminary results can be adopted to simulate the two-phase shear turbulent flow using the BCT capabilities. To conclude the dissertation, the completed research work is summarized in Chapter 6 and the future work recommendations are presented in Chapter 7.

CHAPTER 2. NUMERICAL METHODS

2.1 PHASTA overview

The direct numerical simulations are performed with research CFD-solver, PHASTA [146, 147]. PHASTA is a Parallel, Hierarchic, higher-order (from the 2nd to the 5th order accuracy, depending on the choice of function), Adaptive, Stabilized (finite element method-based (FEM)) Transient Analysis flow solver for both incompressible and compressible flows. The flow solver has been proven to be an effective tool for a multitude of different types of simulations including, Reynolds-Averaged Navier-Stokes (RANS), Large-Eddy Simulation (LES), Detached-Eddy Simulation (DES), and DNS. PHASTA uses advanced anisotropic adaptive algorithms [148] and the most advanced LES-DES models [149].

Various benchmarks have verified and validated the PHASTA code for the simulation of turbulent flows. Jansen [146] described the development and validation of PHASTA for LES to compute the turbulence around airfoil. Then in 2001 [150], Whiting and Jansen validated the stabilized FEM with higher-order hierarchical basis functions by performing a series of classic single-phase CFD problems, including Kovasznay flow, flow over a backward-facing step and lid-driven cavity flow. Trofimova et al. [151] performed the DNS for the turbulent single-phase channel flows at $Re_\tau = 180$ and 395. By analyzing and validating various turbulent statistics, they demonstrated the accuracy of the stabilized FEM for turbulence simulation. Araya et al. [152] introduced a dynamic rescaling-recycling method to the code. This capability enables the simulation of the spatially evolving boundary layers

under more general pressure gradient situations. The validation test are performed in zero, favorable and adverse pressure gradient flows and the results agree with the expected values.

Nagrath et al. [95] implemented the level-set interface tracking method [49, 153] to the PHASTA code, thus significantly extending the simulation capability from single-phase to two-phase. They validated the approach by simulating the implosion and rebound of an air bubble and the simulation results were qualitatively similar to those observed/predicted in experimental/numerical studies. The two-phase simulations using PHASTA have been reported in a wide range of applications. Galimov conducted the study about interfacial waves [154] and plunging liquid jet [155] using PHASTA. Rodriguez et al. [156] described a parallel mesh adaptation method to refine and coarsen regions of the solution domain on the application of annular two-phase flows. They validated their approach by performing a set of simulations ranging from simple canonical test problems, i.e., two dimensional dam break and solitary wave, up to the experimental annular steam-water flow condition with Re_τ of 792 using PHASTA. Bolotnov et al. [48] performed the two-phase turbulent bubbly channel flow at $Re_\tau = 180$. They determined the bubbles' influence on the turbulence field by analyzing the mean velocity distributions, local void fraction as well the local turbulent kinetic energy and the dissipation rate of the liquid phase. Later an additional study to analyze the influence of bubbles on the turbulence anisotropy at $Re_\tau = 180$ and 400 was performed [53]. Behafarid et al. [157] analyzed the dynamics of large deformable bubbles in a vertical circular pipe and a narrow rectangular channel of different inclination angles from 0^0 to 45^0. The simulation results of the Taylor bubble flow in a vertical pipe are validated against the theoretical model and the results for bubbles flowing along inclined rectangular channels were validated against

experimental data [158] as well. Thomas et al. [94] implemented a proportional-integral-derivative (PID) bubble controller to the PHASTA code and evaluated the interfacial force closure under both laminar and turbulent flow. Good agreement were found between the obtained drag coefficient and experiment-based correlation [1]. Recent publication [159] about the bubbly flows study in PWR relevant geometries has performed with PHASTA at Re of 29,079 and 80,775 based on channel hydraulic diameter. As a massively parallel turbulent flow solver, PHASTA demonstrates strong scalability at extreme scale. Sahni et al. [160] reported that PHASTA scales well up to 32,768 cores. Rasquin et al. [161] extended the application of PHASTA on a realistic wing design with up to 786,432 cores.

PHASTA is an open source code. However, in the current setup, it uses commercial linear solver libraries from Altair Engineering, Inc. The visualization is carried out using Paraview [162], an open-source software developed by Kitware Inc. Meshing tools for PHASTA are provided by Simmetrix Inc.

2.1.1 Governing equations

The spatial and temporal discretization for the Incompressible Navier-Stokes (INS) equations used in PHASTA have been described in [150]. The strong form of the INS equations is given by:

Continuity
$$\frac{\partial u_i}{\partial x_i} = 0 \qquad (49)$$

Momentum
$$\frac{\rho \partial u_i}{\partial t} + \rho u_j \frac{\partial u_i}{\partial x_j} = -\frac{\partial p}{\partial x_i} + \frac{\partial \tau_{ij}}{\partial x_j} + f_i \qquad (50)$$

where ρ is density, u_i is the i^{th} component of velocity, p is the static pressure, τ_{ij} is the viscous stress tensor, and f_i is the body force along the i^{th} coordinate, including the surface tension force and gravitational force. The viscous stress tensor for an incompressible flow of a Newtonian fluid is related to the fluid's dynamic viscosity, μ_l, and the strain rate tensor, S_{ij}, as:

$$\tau_{ij} = 2\mu_l S_{ij} = \mu_l\left(\frac{\partial u_i}{\partial x_j} + \frac{\partial u_j}{\partial x_i}\right) \quad (51)$$

Level-set interface tracking method has the superior capability in capturing interface parameters. Based on the level-set distance field (φ), the curvature of gas-liquid interface can be computed as

$$\kappa(\varphi) = -\nabla \cdot \left(\frac{\nabla\varphi}{|\nabla\varphi|}\right) \quad (52)$$

The surface tension force is then represented by

$$F_{st} = \kappa\sigma\left(\frac{\nabla\varphi}{|\nabla\varphi|}\right) \quad (53)$$

where σ is the surface tension coefficient. We utilize the Continuum Surface Force (CSF) model [163] which is formulated to numerically model the surface tension effects and it is included in f_i.

2.1.2 Level-set method

The solution of the interface tracking method is based on the "one-fluid" formulation. The one-fluid formulation allows the multiphase flow with interfaces to be treated as a single fluid which has different properties on each side of the interface. To distinguish between liquid

phase and gas phase, the level set method [49, 153, 164, 165] is proposed for interface tracking in the presented research and involves modeling the interface as the zero-level set of a smooth function, φ, where φ is often called the first scalar and it represents the signed distance from the interface. Hence the interface is defined by $\varphi = 0$. In case of no phase change in the flow the scalar, φ, is advected with a moving fluid according to

$$\frac{D\varphi}{Dt} = \frac{\partial \varphi}{\partial t} + \boldsymbol{u} \cdot \nabla \varphi = 0 \qquad (54)$$

where $\boldsymbol{u}$ is the flow velocity vector. The liquid phase is indicated by a positive level set.

As a promising alternative to the Volume of Fluid (VOF) and Front-Tracking (FT) method, the level-set interface tracking method is known for mass conservation issues, especially for under-resolved flows. We introduce an approach to ensure the constant bubble volume for adiabatic two-phase cases. The level set advection equation is given by Eq.(54), in which u is the advection velocity. As long as the expected bubble volume is known, the PID bubble controller, which will be discussed in the following section, can be used to compare the current bubble volume with the prescribed value, and then manipulate the advection velocity accordingly to preserve the bubble volume [166]. Figure 4 shows the bubble volume evolution with the prescribed bubble volume of $6.545 \times 10^{-8}\ m^3$. The time range shown in Figure 4 is 0.1 s which corresponds to one quarter flow-through, the number of times one Lagrangian particle passing through the domain. The selected case is the turbulent intensity study case with bubble local turbulent intensity of 2.86%. With the mass control capability, the case maintains good mass conservation and the bubble volume fluctuation magnitude is around 2.0% throughout the entire simulation. Good mass conservations are observed for all the cases

described in this thesis while the fluctuation magnitude will vary from 0.3% to 3.0% depending on the conditions.

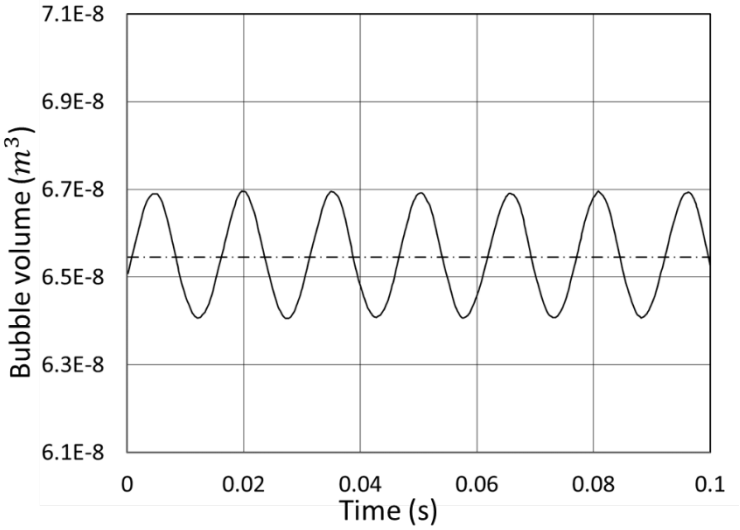

Figure 4. Comparison of the bubble volume evolution of a selected case for turbulent intensity study. Solid and dash lines represent the instantaneous void fraction and the expected void fraction, respectively.

Since evaluating the jump in physical properties using a step change across the interface is challenging numerically, the properties near the interface are defined using a smoothed Heaviside kernel function, H_ε

$$H_\varepsilon(\varphi) = \begin{cases} 0, & \varphi < -\varepsilon \\ \frac{1}{2}\left[1 + \frac{\varphi}{\varepsilon} + \frac{1}{\pi}\sin\left(\frac{\pi\varphi}{\varepsilon}\right)\right], & |\varphi| < \varepsilon \\ 1, & \varphi > \varepsilon \end{cases} \quad (55)$$

where ε is the interface half-thickness. The fluid properties are then defined as

$$\rho(\varphi) = \rho_1 H_\varepsilon(\varphi) + \rho_2\left(1 - H_\varepsilon(\varphi)\right) \quad (56)$$

$$\mu(\varphi) = \mu_1 H_\varepsilon(\varphi) + \mu_2(1 - H_\varepsilon(\varphi)) \quad (57)$$

Although the solution may be reasonably good in the immediate vicinity of the interface, the distance field may not be correct throughout the domain since the turbulent flow field distort the level-set contours. Thus, the level-set has to be corrected with a re-distancing operation by solving the following partial differential equation (PDE) [153, 164, 167, 168].

$$\frac{\partial \varphi_d}{\partial \tau} = S(\varphi)[1 - |\nabla \varphi_d|] \quad (58)$$

and φ_d is a scalar that represents the corrected distance field and τ is the pseudo time over which the PDE is solved to steady-state. The initial condition is

$$\varphi_d(\boldsymbol{x}, 0) = \varphi(\boldsymbol{x}) \quad (59)$$

A nice feature of this re-initialization procedure is that the level-set function is reinitialized near the front first. So it can be alternatively expressed as the following transport equation:

$$\frac{\partial \varphi_d}{\partial \tau} + \vec{w} \cdot \nabla \varphi_d = S(\varphi_d) \quad (60)$$

The so-called second scalar d is originally assigned and the level set field φ is convected with a pseudo velocity $\vec{w}$ where

$$\vec{w} = S(\varphi)\frac{\nabla \varphi_d}{|\nabla \varphi_d|} \quad (61)$$

and $S(\varphi)$ is defined as

$$S(\varphi) = \begin{cases} -1, & \varphi < -\varepsilon_d \\ \left[\frac{\varphi}{\varepsilon_d} + \frac{1}{\pi}\sin\left(\frac{\pi\varphi}{\varepsilon_d}\right)\right], & |\varphi| < \varepsilon_d \\ 1, & \varphi > \varepsilon_d \end{cases} \quad (62)$$

where ε_d is the distance field interface half-thickness which, in general, may be different from ε in Eq. (55). The zeroth level set, or the interface $\varphi = 0$, does not move since its convecting velocity $\vec{w}$ is zero. Solving the second scalar to steady-state restores the distance field $\nabla d = \pm 1$

but does not alter the location of the interface. The first scalar φ is then updated using the steady solution of the second scalar *d*.

2.2 PID bubble controller

The proportional-integral-derivative (PID) bubble controller is implemented [94] in the PHASTA code to balance the interfacial forces, like drag and lift forces. Using the PID bubble controller, we can control the bubble at a fixed position (in all three directions) shown in Figure 5. The control forces can be extracted from the simulation and used to compute lift and drag coefficients [56, 94].

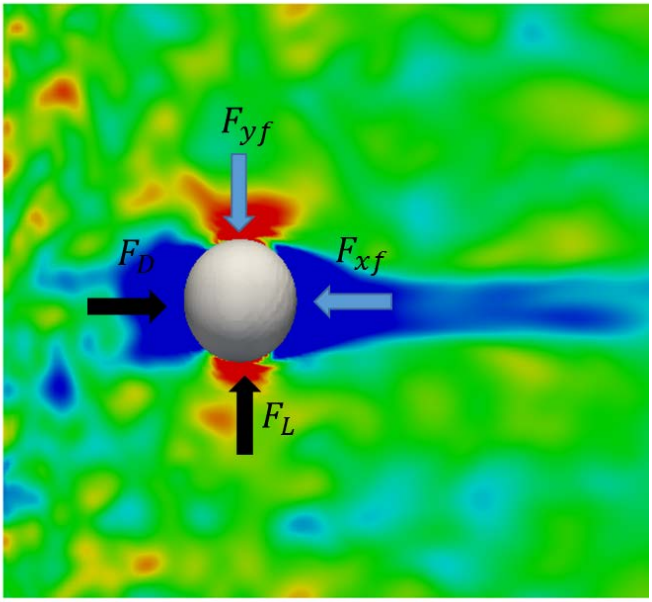

Figure 5. Illustration of the force balance acting on the bubbles. F_D, F_L, F_{xf} and F_{yf} represent the drag force, lift force, streamwise (x) direction control force and lateral (y) direction control force, respectively.

The Galilean invariant states that the laws of motion are the same in all inertial frames. Considering the rising bubble in two-phase upflow, the liquid phase has a rising velocity of

$-|u_r|$ when taking the center of the rising bubble as inertial frame. Using the PID bubble controller, the bubble is kept at fixed position. Taking the constant moving liquid phase as inertial frame, the bubble has a rising velocity of -$|u_r|$. Therefore, the physics behind the PID bubble controller is essentially Galilean invariant to the rising bubble in standing fluid. Figure 6 shows the transformation of the observation frame for the wall effect study on the interfacial forces acting on the bubble. Figure 6(a) shows the schematics of the two-phase upflow scenarios and our simulation in the laboratory frame. After the transformation of the observation frame, Figure 6(b) demonstrates that the two scenarios are essentially the same with PID bubble controller.

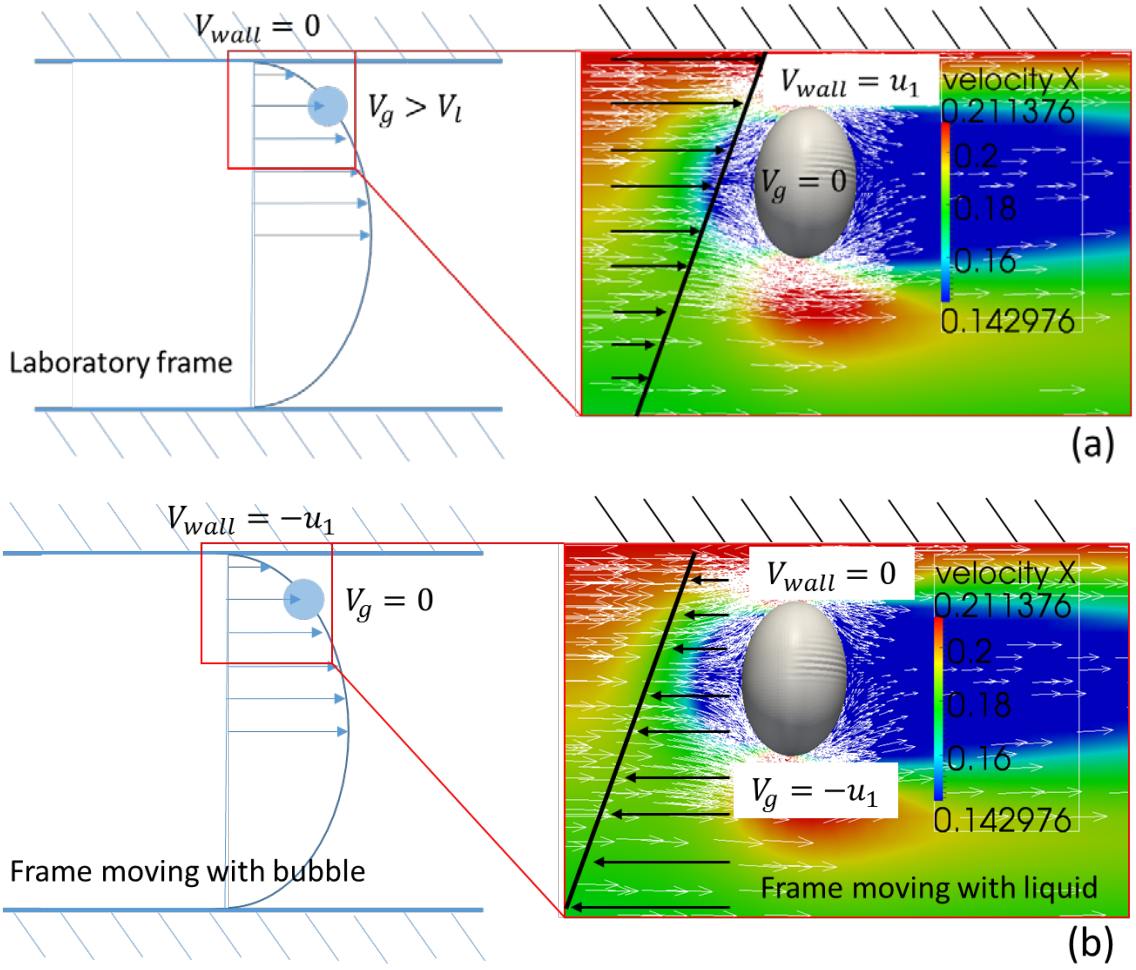

Figure 6. Transformation of inertial frame for wall effect on interfacial forces study.

The PID controller consists of three error feedback mechanisms: the proportional part which represents the current error; the integral part which represents the accumulation of past errors; the derivative part which represents the prediction of future error. The error output for the bubble control algorithm is treated as the distance between the bubble's current position and its initial position. For each simulated time step, the bubble controller assesses the bubble's location and velocity and uses those variables as inputs for control loop feedback. The mathematical form of the PID-based bubble controller is given below [167]

$$CF_i^{(n+1)} = c_1\overline{CF_i^{(n)}} + c_2\left[CF_i^{(n)} + c_3 dx_i^{(n)} + c_4 dx_i^{2^{(n)}} + c_5 dx_i^{3^{(n)}} + c_6 v_i^{(n)} + c_7 v_i^{2^{(n)}} + c_8 v_i^{3^{(n)}} + c_9 dv_i^{(n)}\right] + \left[c_{10} dx_2^{2^{(n)}}\right]_{if\ i=1} \quad (63)$$

where $CF_i^{(n)}$ is the i^{th} component of the control force at time n, $\overline{CF_i^{(n)}}$ is the historical average of the i^{th} component of control force at time n, $dx_i^{(n)}$ is the i^{th} component of the bubble position difference between time n and time zero, $v_i^{(n)}$ is the i^{th} component of the bubble's average velocity at time n. $dv_i^{(n)}$ is the i^{th} component of the difference in the bubble's average velocity at time n and time $n-1$, $dx_i^{2^{(n)}}$ and $dx_i^{3^{(n)}}$ are the i^{th} components of the difference between the bubble's location at time n and time zero squared, and cubed, respectively, $v_i^{2^{(n)}}$ and $v_i^{3^{(n)}}$ are the i^{th} components of the bubble's average velocity at time n squared, and cubed, respectively, c_k, for k=1, …, 10, are controller gains. The velocity component convention used in this work is $i = 1$ refers to the x-component, $i = 2$ refers to the y-component, and $i = 3$ refers to the z-component. Eq. (63) can be simplified to the following form, as it was determined that many of the higher order terms were not necessary for obtaining the results presented in this paper.

$$CF_i^{(n+1)} = c_1\overline{CF_i^{(n)}} + c_2\left[CF_i^{(n)} + c_3 dx_i^{(n)} + c_4 dx_i^{2^{(n)}} + c_5 v_i^{(n)}\right] \quad (64)$$

Analysis of Eq. (63) reveals a PID-based form. The historical average, $\overline{CF_i^{(n)}}$, is analogous to the integral input, the linear, and higher order location difference terms function as the proportional input, and the velocity and velocity difference terms resemble the derivative input. The application and implementation of PID bubble controller is an extensive learning

process. Through iterative test-trials, we are able to find the appropriate control coefficients to keep the bubble fixed in space over time.

A set of validation tests were done for a range of relative velocity values where the bubble Reynolds number was varied. The bubble Reynolds number is defined as

$$Re_b = \frac{\rho_l u_r D}{\mu_l} \quad (65)$$

By using the PID bubble controller, we can balance the drag and lift forces, extract the information of control force and calculate the drag coefficient based on Eq. (23). The results are summarized in Table 2. The control coefficients setup is summarized in Appendix B.

Table 2. Drag coefficients at different bubble Reynolds numbers.

Case	1	2	3	4	5	6	7	8	9	10
u_r (m/s)	0.0125	0.0175	0.025	0.04	0.05	0.06	0.07	0.08	0.09	0.10
Re_b	72.93	102.11	145.86	233.38	291.73	350.07	408.42	466.77	525.11	583.46
C_D	0.6805	0.4493	0.3172	0.2075	0.1722	0.1520	0.1372	0.1266	0.1198	0.1142

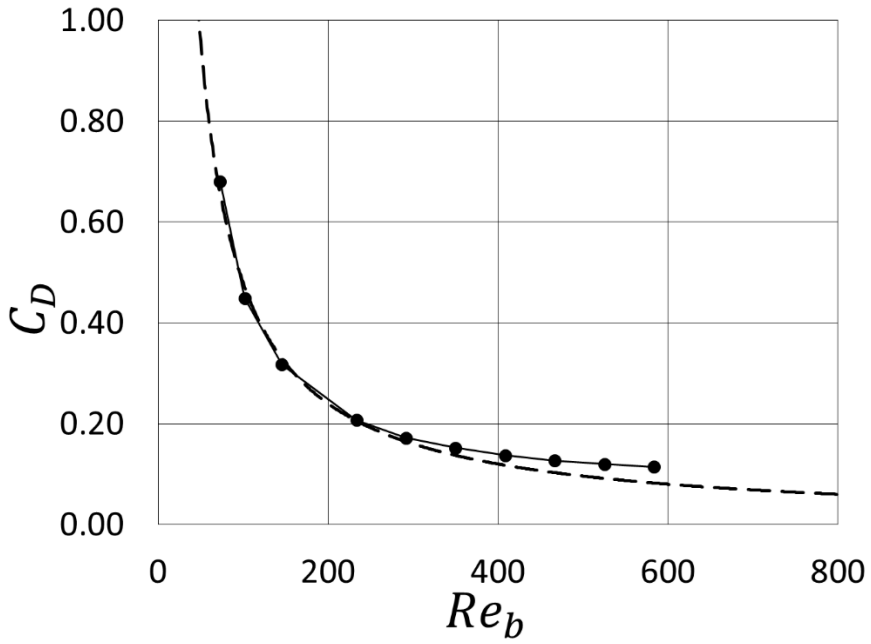

Figure 7. Estimated drag coefficient from PHASTA simulation (solid line with symbols) as a function of bubble Reynolds number. Dashed line shows Tomiyama's experiment-based correlation [1].

Figure 7 shows the estimated drag coeffcients extracted from the PHASTA simulations plotted against bubble Reynolds number. The influence of the bubble Reynolds number on the drag coefficient is drastic when Re_b is less than 200, however, the influence of the bubble Reynolds number on the drag coefficient becomes smaller and smaller with continuously increasing the bubble Reynolds number. At low bubble Reynolds number, the estimated coefficients agree very well with the correlation. It is noted that for higher bubble Reynolds number, the correlation begins to under-predict the estimated coefficients. Since the correlation was developed for spherical bubbles, the under prediction is expected to occur when the numerical results are obtained for a slightly deformed bubble. In the simulations the deformation (shown in Figure 8) occurs due to increased relative velocity and larger drag force.

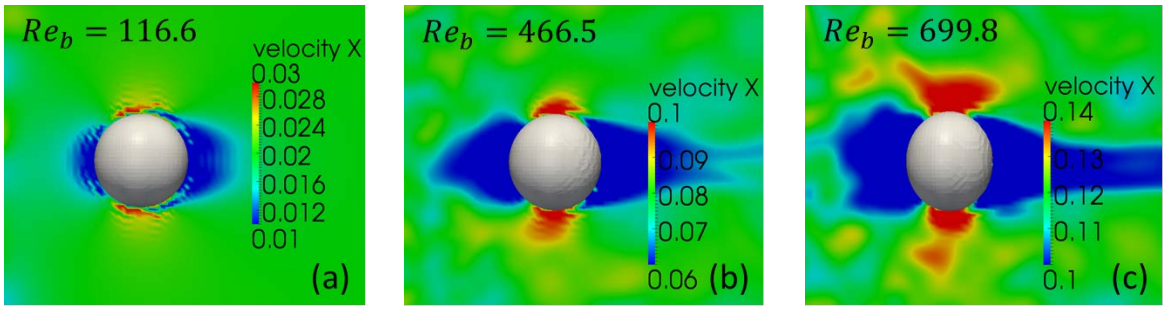

Figure 8. Bubble shape versus bubble Reynolds number, Re_b.

2.3 Turbulence generation algorithm

In the presented research we will consider two common types of turbulent flows: homogeneous uniform flow and shear turbulent flow. Thus two turbulent generation algorithms are designed accordingly here and both are based on the block-induced turbulence algorithm which is widely used in the physical experiment [16, 58, 63, 169].

2.3.1 Homogeneous uniform turbulent flow generation

To reduce the uncertainties in bubble-induced turbulence measurement, it is important to use reproducible boundary conditions to represent the liquid turbulence structure repeatedly. While the random behavior of the turbulent flows is well-known, the DNS approach allows well controlled boundary conditions which are not possible with experimental setup. The general research steps are: (i) perform a stand-alone simulation of single-phase turbulence flow in a desired geometry with periodic boundary conditions to obtain desired turbulence level and flow rate; (ii) record the instantaneous two-dimensional velocity profile as a function of time at the periodic outflow location; (iii) utilize the recorded instantaneous field as the inflow boundary conditions for the production two-phase simulations. This procedure has been

successfully tested by our research group before [55, 145]. The production simulations will use the same inflow boundary conditions which will remove the single-phase turbulence uncertainties from the two-phase analysis results.

The stand-alone simulation of single-phase turbulent flow is designed as follows. In order to obtain homogeneous turbulent flow, we apply the uniform pressure gradient to drive the flow through two grid planes, similar to the typical experimental setup [16, 63]. The existence of small spheres will serve as obstacles to disrupt the laminar flow and create turbulence, like the turbulence generating grids in experiments (Figure 1). The computational domain for the generation of the single-phase homogeneous turbulent flow in our DNS is prescribed by a box with the dimension of 60×25×15 mm^3 as shown in the Figure 9.

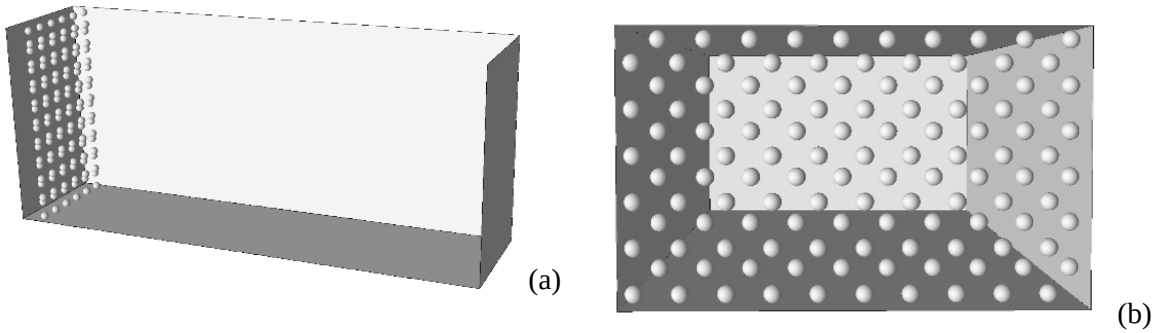

(a) (b)

Figure 9. Domain of sing-phase homogeneous turbulence generation. (a) shows the 3D geometrical configuration of the domain; (b) shows the cross sectional view of the domain in streamwise (x normal) direction.

Two grid planes with spacing of 1 mm are placed at $x = 2$ mm and $x = 3$ mm streamwise direction to leave enough distance to develop the homogeneous turbulence. In each grid, we have a 10×6 cells. Each cell has the dimension of 2.5×2.5 mm^2 and contains 1 mm diameter sphere as the obstacle. The configuration is shown in the Figure 10. The Reynolds number of the sphere is 350 and is high enough to generate turbulent eddies.

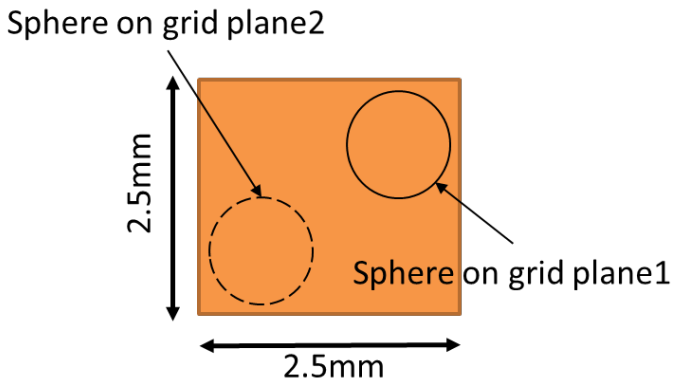

Figure 10. Geometric configuration of a single cell on the obstacle grid planes.

Let us describe the meshing approach for the single-phase simulation domain. We apply several meshing layers parallel to the boundary of each obstacle sphere surface to capture the turbulent boundary layer. The thickness of the first boundary layer is estimated based on the smallest turbulence length scale, i.e., Kolmogorov scale. The Kolmogorov scale is estimated using the following equation [27]:

$$\eta = \left(\frac{\nu^3}{\varepsilon}\right)^{\frac{1}{4}} \quad (66)$$

where ν is the kinetic viscosity and ε is the dissipation rate of turbulent kinetic energy. The dissipation rate is determined based on the energy balance. The energy balance estimate is performed as follows. We apply the pressure gradient on the whole domain to offset the drag force due to the existence of the spherical obstacles. The drag force on the sphere is given in Eq.(67). Since the sphere Reynolds number is 350, the drag coefficient is found to be 0.617 [108].

$$F_{drag} = \frac{1}{2} C_D \rho u_r^2 A \quad (67)$$

where C_D is the drag coefficient, u_r is the relative velocity between solid sphere and liquid and A is the sphere projected area on the lateral plane.

Then the pressure force is determined based on the drag force:

$$F_{pressure} = F_{drag} \quad (68)$$

$$P = F_{pressure} v_r \quad (69)$$

The dissipation rate is finally determined as

$$\varepsilon = \frac{P}{m} \quad (70)$$

where m is the liquid mass in the whole domain. The dissipation rate is then calculated to be $3.49 \times 10^{-2} \frac{m^2}{s^3}$.

Based on the calculation from Eq. (67) to (70), the Kolmogorov scale is estimated to be 6.5×10^{-2} mm. The dimensionless wall distance, y^+, based on the first layer thickness of the obstacle sphere is 0.33. The geometrical and mesh configuration of the model are given in Table 3 and Figure 11. Boundary layers are added on the obstacle sphere surface to accurately capture the flow behavior.

Grid refinement study is performed with two mesh setups, 28 and 129 million elements. The statistics of the mesh configuration is given in Table 3. Grid resolution studies are not typical for DNS since the individual runs are quite expensive. Since we are considering the decay of homogeneous turbulence in the wake of the obstacles, the mesh resolution requirements downstream the obstacles vary as the turbulence intensity changes. We perform the mesh study to demonstrate that the choice of the mesh resolution is appropriate to resolve all the turbulent scales in the region of interest. The finer mesh case, 129 million elements, has

been created using the same domain as the coarser mesh case (with 28 million elements) while the bulk mesh resolution is refined from 0.2 mm to 0.1 mm in all 3 directions. Identical mesh resolution on the sphere surface are chosen for both cases and it is finer than the Kolmogorov length scale. The mesh configuration of the 28 million elements case is shown in Figure 11. Since the second grid plane is shifted by 1.25 mm in the direction normal to the view, we can only observe the first grid plane in the figure.

Table 3. Geometrical and mesh configuration of the single phase homogeneous turbulent flow case.

Setup		28 million elements case	129 million elements case
Domain size (mm^3)		$60\times25\times15$	
Bulk mesh resolution (mm)		0.2	0.1
Mesh setup of sphere boundary layer	Mesh resolution on the surface (mm)	5×10^{-2}	
	First layer thickness (mm)	2×10^{-2}	
	Boundary layer total thickness (mm)	5.19×10^{-1}	

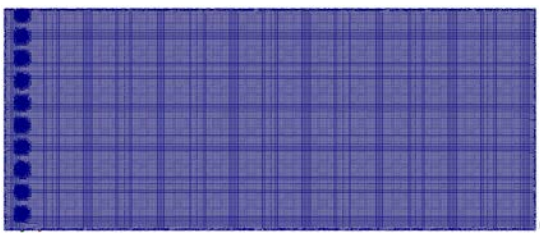
(a)
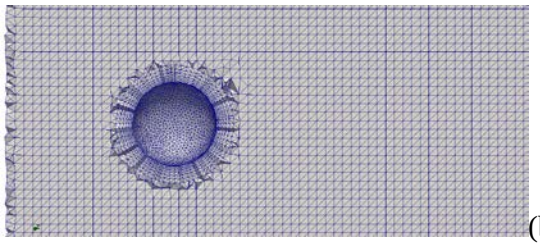
(b)

Figure 11. Mesh configuration of the homogeneous turbulence generation case. (a) shows the mesh configuration of the whole domain; (b) shows the mesh configuration and boundary layer on the obstacle sphere surface.

Based on the force balance between the pressure and the obstacles' friction, a constant pressure gradient of 400 N/m^3 is applied on the domain to drive the flow. Periodic boundary

conditions are used in all three directions in order not to restrain the liquid turbulence structures. 3D view of the single-phase homogeneous turbulent flow generation is shown in Figure 12. As the flow passes around each grid sphere, vortices are created around the sphere and in its wake. After the turbulent flow reaches a statistically steady-state conditions, the transient velocity profile of a plane perpendicular to the flow direction is recorded over the time period corresponding to the 28 domain flow-throughs (e.g. the time it takes a Lagrangian particle to cross the domain). The position of the probe plane, $\boldsymbol{x = 55\ mm}$, is chosen to make sure that both the velocity profile and the turbulent kinetic energy are homogeneous and are not directly affected by the shape and spanwise location of the turbulence generating grid. The probe plane [53] which is normal to the streamwise direction, i.e., x direction, contains 125 (nodes in *y* direction) $\times 75$ (nodes in *z* direction) probes which are used to extract the instantaneous velocity information at those points over time and allows user to determine the level of turbulent kinetic energy. By measuring the liquid turbulence consecutively using probe planes, the liquid turbulence are averaged over time window of 1.86 s. As the relative error in turbulent kinetic energy profiles for three consecutive time windows are within 2%, we claim that the liquid turbulence reaches steady state. Figure 13 shows the statistics of single phase turbulent flow for three consecutive time windows and the results show consistency.

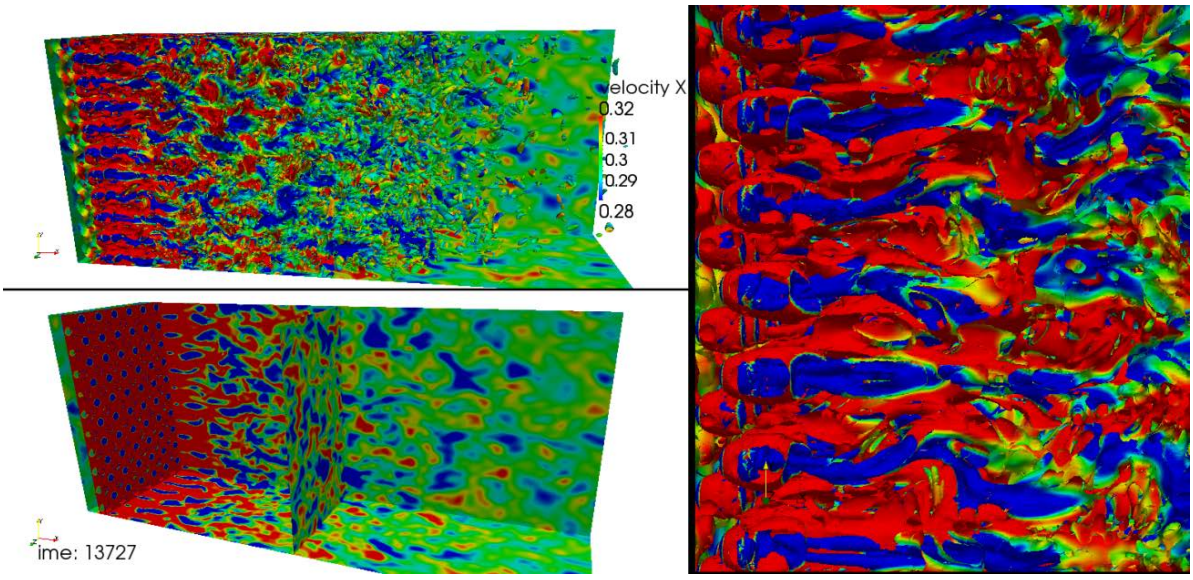

Figure 12. 3D view of the homogeneous turbulent flow generation.

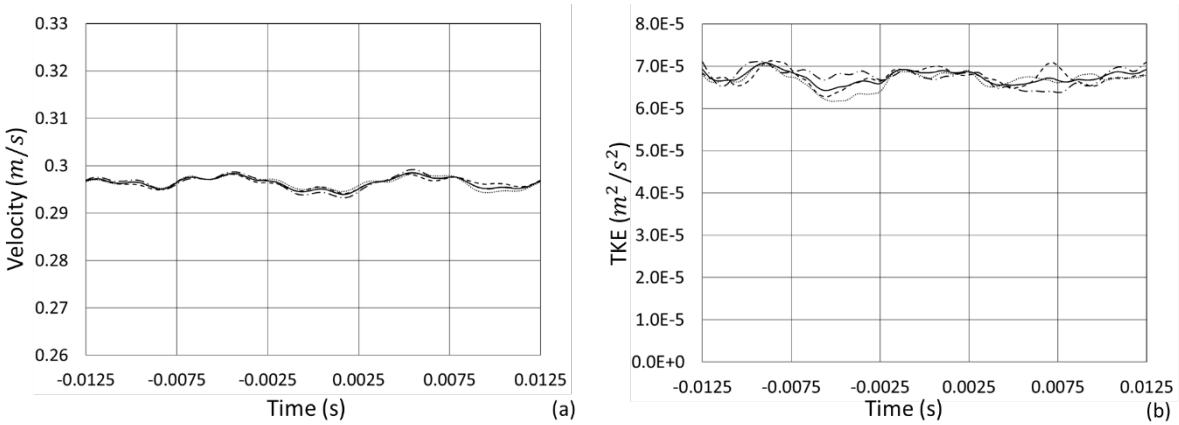

Figure 13. Measurement of turbulence statistics for three consecutive windows and each has a time window of 1.86 s. Dot, dash, dash-dot and solid lines represent the time window 1, the time window 2, the time window 3 and the entire time window containing all three windows, respectively.

2.3.2 Shear turbulent flow generation

Similar turbulence generation approach is adopted for the shear turbulent flow. The need for a deeper understanding of turbulent shear flow leads naturally to a search for “simple”

shear flows. Owen and Zienkiewicz [169] developed a formula (Eq. (71)) to generate shear turbulent flow using non-uniform grid distribution shown in Figure 14.

$$\frac{\xi}{(1-\xi)^2} = K_0\left[1 - 2\frac{\lambda h}{U}\left(\frac{1}{K_0} + \frac{1}{1+a}\right)\left(\frac{y}{h} - \frac{1}{2}\right)\right] \quad (71)$$

where $\xi = d/S(y)$, d is the rod diameter, S is the lateral direction spacing. The remaining parameters are expressed as follows

$$K_0 = \frac{P_0 - P_1}{\frac{1}{2}\rho U_o^2}, a = \frac{1.1}{\sqrt{1+K_0}}, \lambda = \frac{\partial U}{\partial y} \quad (72)$$

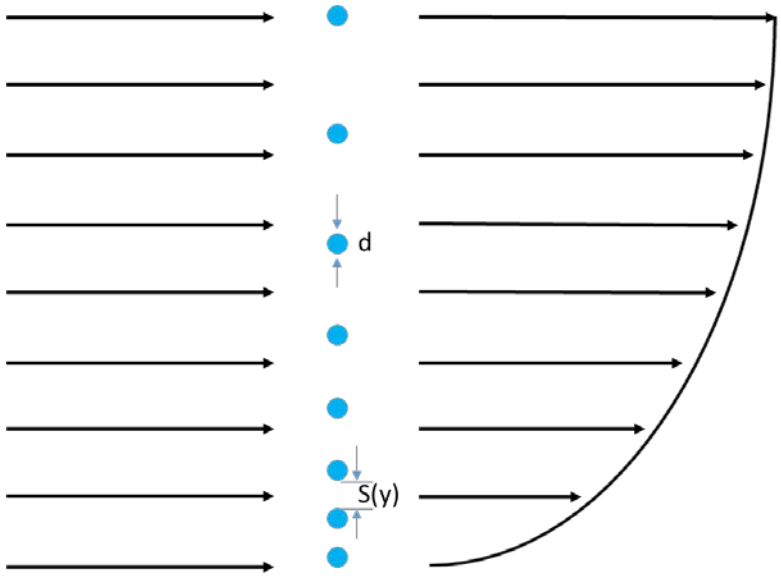

Figure 14. Illustration of turbulent flow generation using non-uniform grid distribution [169].

However, the generated turbulent flow will decay in the streamwise direction. The shear flows are also complicated by the proximity of the solid boundaries. It is known that for certain friction Reynolds number [170], a turbulence profile will sustain itself, thus the motivation for computing friction Reynolds number and boundary layer mesh constraints for

the turbulent cases. It has been shown that a friction Reynolds number as low as 127.3 sustained channel flow turbulence [171]. The friction Reynolds number is given by

$$Re_\tau = \frac{u_\tau \delta}{\nu_l} \quad (73)$$

where u_τ is the friction velocity, δ is the width of the channel, and ν_l is the kinematic viscosity of the liquid. To compute the friction velocity, u_τ, Marie [172] assumed that since bubbles do not reach the laminar sub-layer, the friction velocity for two-phase flows can be found by assuming that the non-dimensional averaged velocity parallel to the wall is equal to the non-dimensional distance from the wall, $u^+ = y^+$, for $y^+ < 5$, just as it is in the single-phase flows:

$$u_\tau = \sqrt{\nu_l \left(\frac{du_l}{dy}\right)_{y=0}} \quad (74)$$

where u_l is the local mean axial liquid velocity. Solving Eq. (73) in terms of the friction velocity, substituting into Eq. (74) and solving that in terms of the shear rate, $\frac{du_l}{dy}$, can give an estimate for the friction Reynolds number for the turbulent shear cases.

$$Re_\tau = \sqrt{\frac{\delta^2}{\nu_l}\left(\frac{du_l}{dy}\right)_{y=0}} \quad (75)$$

The single-phase cases with various initial shear rates were run. To save time on computation and introduce the velocity instabilities, the turbulence was invoked by an array of solid rigid spheres in the center of the domain as shown in Figure 15. Once the turbulence was generated, the solid rigid spheres were removed from the domain and the simulation was run long enough to observe that the turbulence was sustained solely by the wall shear. Then we

can put a virtual probe plane to record the instantaneous velocity history for the future use of two-phase flow simulation. Those data files are called boundary condition transient (BCT) data. Figure 16 shows the flowchart of the BCT generation and implementation. Selected subroutines can be found in Appendix C and D. The author makes the parallel computing of those BCT files possible and it will be discussed in the following sub-section.

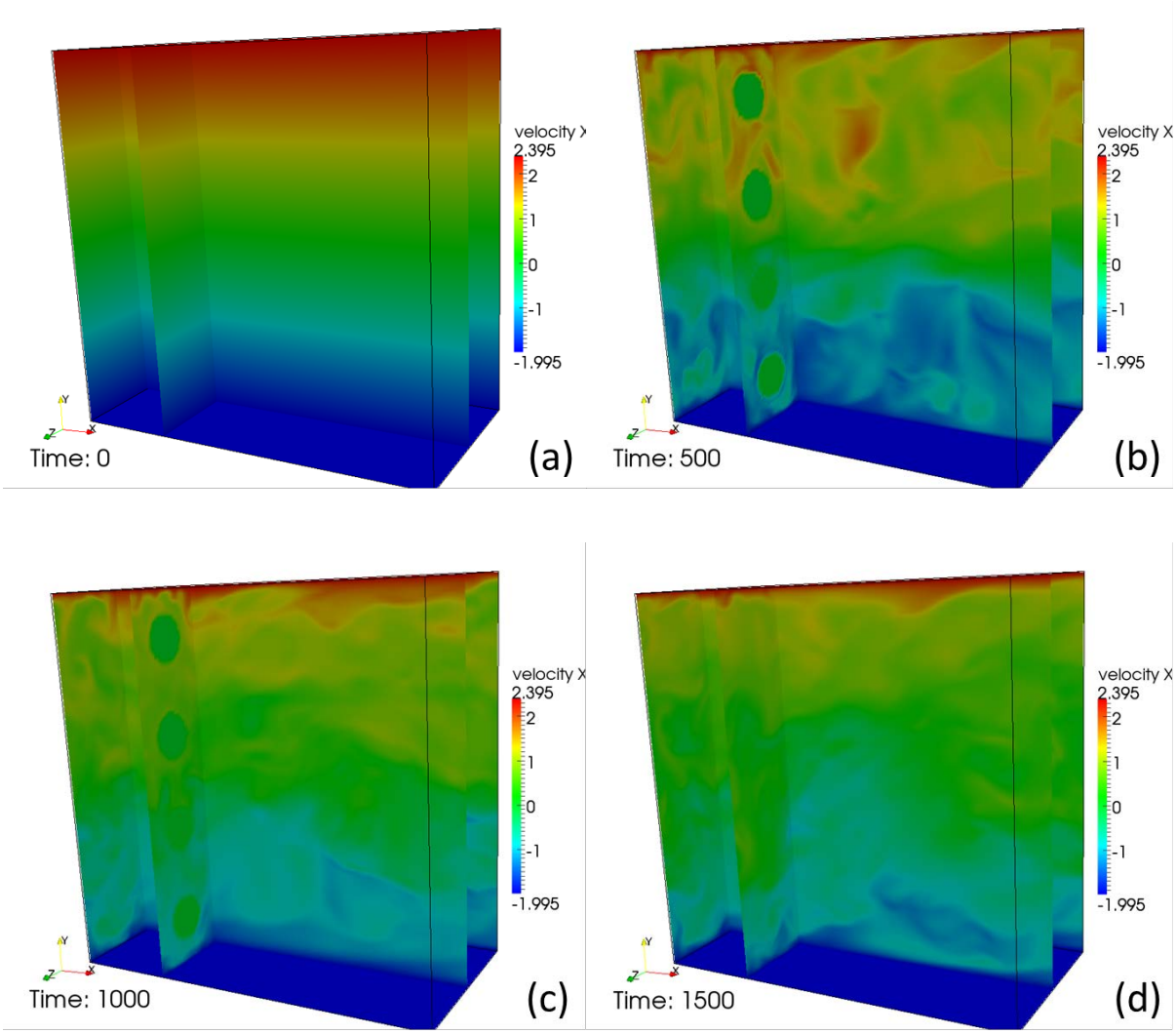

Figure 15. Shear turbulent flow generation at various simulation time steps.

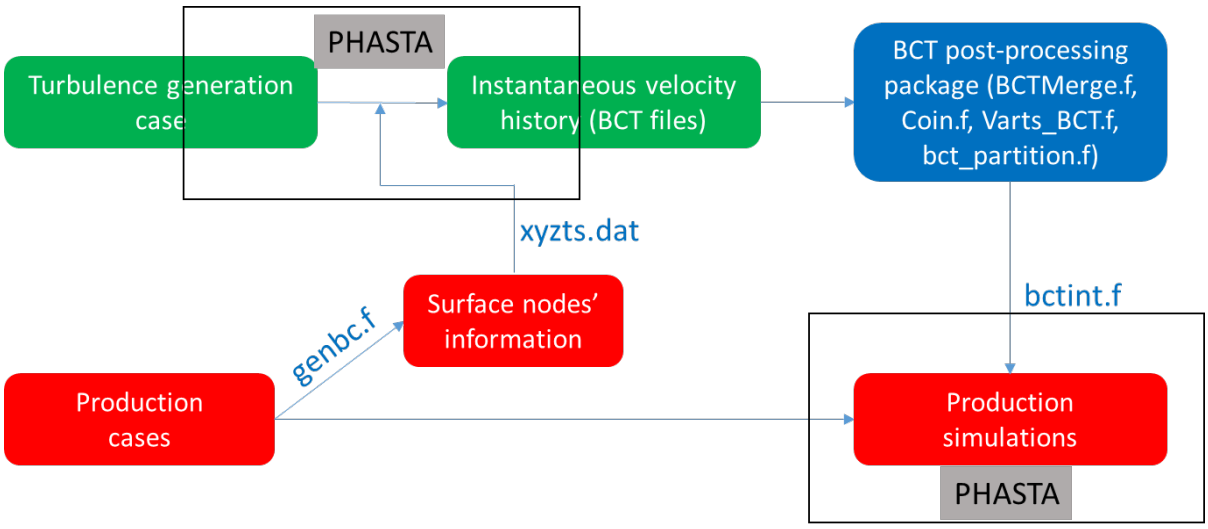

Figure 16. Flowchart of BCT files' generations and implementations.

To determine whether the single-phase turbulent field reached a statistically steady-state condition or not, the recorded data was averaged over several time windows to assess whether the mean velocity and turbulent kinetic energy were converging to a statistically steady state solution. The subroutines for the data analysis is given in Appendix E.

2.4 Parallel BCT file computing capability

After we obtained the instantaneous velocity history from either homogeneous turbulent flow or shear turbulent flow, those raw data files, i.e., the BCT files, are used to provide the transient inflow boundary condition for the two-phase turbulent flow cases. In PHASTA code, the simulation domain is divided into several partitions to be computed in parallel on multiple computing cores. In parallel simulations, each compute core/unit is responsible of calculations on one mesh partition, which usually contains thousands of elements (the recommended range is between 3,000 and 100,000 elements per each partition).

Since both the inflow boundary surface and the outflow boundary surface are usually partitioned into different cores which makes the parallel computing capability of the BCT files necessary. Initially, the implementation of BCT files was solely conducted by forcing all the elements on the inflow surface to be computed on the master node. However, this approach could not be efficiently scaled beyond 64 core runs. Using the previous approach, the simulation cannot proceed to the next time step until the master partition core has implemented the latest velocity information on the boundary surface. The author implemented the parallel BCT computing capability to the PHASTA code using Message Passing Interface (MPI) programming. This capability follows a two-step approach. The first step is called pseudo-run which usually takes a few seconds to finish since only one time step is required to be performed. In this step, the PHASTA code will determine the assigned computation cores for each mesh element on the boundary surface and output the elements' information and their assigned cores. The second step is the production run. The original BCT files will be reconstructed and distributed on those cores which contain the boundary elements. The new BCT files will be read by the solver and used as the boundary conditions for the two-phase flow.

As shown in Figure 17, in the original master node computing approach, all the elements on the inflow surface are forced to stay at node 2 which represents the master node. However, after we implement the parallel computing approach, the boundary elements are successfully distributed to various cores.

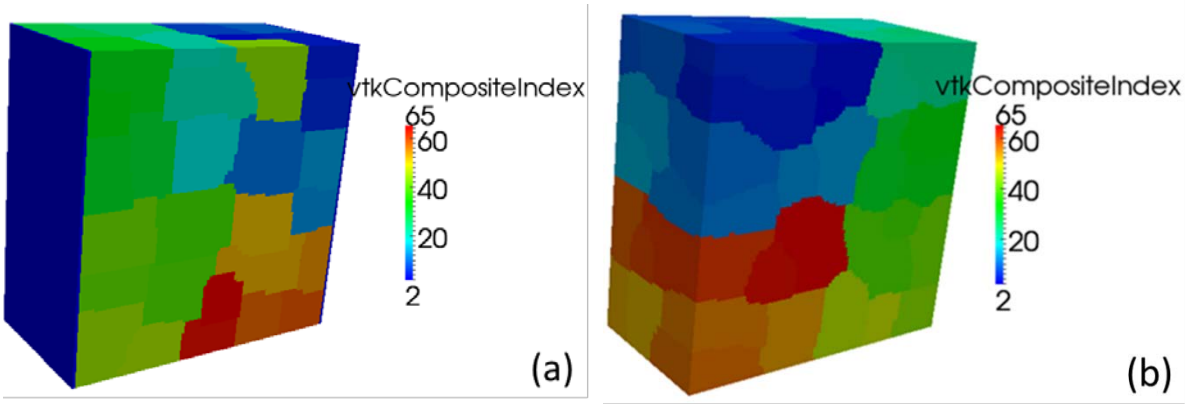

Figure 17. Partition of the simulation domain to 64 cores where vtkCompositeIndex represents the ID of the cores. (a) shows the partition where all the nodes on the inflow surface are assigned to the master core; (b) shows the new partition using the new parallel computing approach.

A test case with 1.17 million elements are built to test the scaling performance of the new capabilities running on 64, 128, and 256 cores. Figure 18 compares the computational performance for different partitions. Figure 18 (a-c) shows the physical computing time, i.e., wall clock, for the identical test case running separately on 64, 128 and 256 cores with different simulation time steps and BCT files computing approach. The parallel computing approach did boost the computational efficiency. The relative efficiencies are calculated as follows. We first calculate the physical time per simulation time step

$$\frac{time}{iterations} = \frac{final\ wall\ clock - initial\ wall\ clock}{final\ time\ step - initial\ time\ step} \quad (76)$$

Then the absolute computing efficiency is calculated as

$$\eta = \frac{time}{iteration} \times number\ of\ cores \quad (77)$$

For example, we have a test case running on 64 cores. The case runs from time step 500 to time step 1000. The wall clock at time step 500 is 1.598×10^4 s and the wall clock at time step 1000 is 3.109×10^4 s. Thus the absolute efficiency is

$$\eta_{64} = \frac{3.109 \times 10^4 - 1.598 \times 10^4}{1000 - 500} \times 64 = 1818.88 \quad (78)$$

Then the relative efficiency is defined as η_j^i/η_{64}^m, where i represents the different BCT file computing approaches, either master code computing approach (m) or parallel computing approach (p); j represents the different partitions, 64, 128, and 256 cores. Figure 18(d) compares the relative efficiency and it shows that the parallel computing capability boosts the efficiency by 40% when the case is running on 64 and 256 cores.

However, when using the master node computing capability, the efficiency at 128 cores is better than the case running on 64 cores. This is surprising because for the parallel computing process, the separate tasks running on various cores generally requires some inter-process communication during execution. So we would expect to observe that the computing efficiency decreases as we have more cores. Detailed analysis reveals why this abnormal behavior happens. For this test case, we find that we have 9375 elements on the inflow surface which are computed at the master node. When we run the case on 64 cores, each core will have approximately 18164 elements which is twice the elements on the master node. This means that the master node will finish its computing task first and have to wait for the other cores to finish their task before proceed to the next time step. However, when we run the case on 128 cores, each core will have approximately 9082 elements which is close to the elements on the master node. Accidentally, this mesh partition is close to the mesh partition of the optimal

parallel computing approach. In this way, all the computing cores together with master node will finish their own computing task approximately the same time and proceed to next time step quicker. Due to the unique mesh size of the test case, we observe higher computing efficiency for 128 cores than 64 cores when using master node computing approach. The mesh partition between master node and regular cores still have some difference, around 300, thus the computing performance is still less than the parallel computing capability.

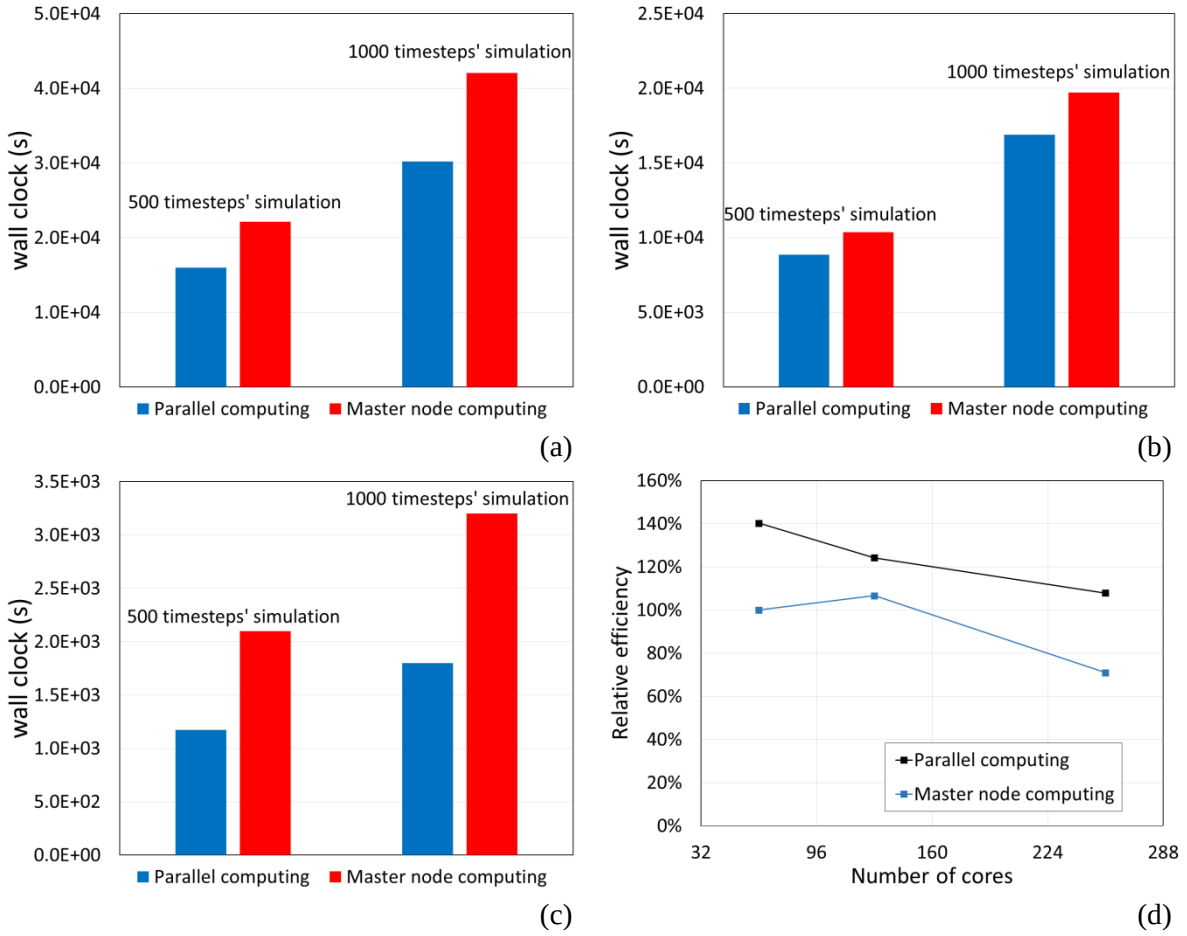

Figure 18. Evaluation of the computational performance of the new parallel BCT files computing capability. (a) to (c) are the computational performance for the cases running on 64, 128 and 256 cores. (d) is the relative efficiency versus the number of cores for different approaches of computing BCT files.

2.5 Data analysis algorithm

We employ averaging techniques (given in Appendix E) to learn about the turbulence structure and the bubble behavior. In contrast with RANS approach, the DNS approach provides us a full 3D time resolved solution of the Navier-Stokes equations. We can introduce virtual probe planes to record the instantaneous velocity history. The probe plane which is normal to the streamwise direction, i.e., *x* direction, contains user-defined probes which are used to extract the instantaneous velocity information at those points over time and allows us to determine the level of turbulent kinetic energy. After we obtained the instantaneous velocity field, the time averaged velocity is defined as

$$\overline{u_i}(\vec{x},t) = \frac{1}{T}\int_T u_i(\vec{x},t)\,dt = \frac{1}{T}\sum_{i=1}^{N} u_i(\vec{x},t)\Delta t \qquad (79)$$

Here, $\bar{u}$ stands for the averaged velocity in all the three spatial directions, u, v and w. Vector $\vec{x}$ represents the probe positions on the probe plane, i.e., y-z plane.

We define the instantaneous velocity fluctuation as

$$u_i'(\vec{x},t) = u_i(\vec{x},t) - \overline{u_i} \qquad (80)$$

Then the time averaged Reynolds stress terms, $\overline{u'u'}$, $\overline{v'v'}$, and $\overline{w'w'}$ are defined as

$$\overline{u'u'}(\vec{x}) = \frac{1}{T}\int_T (u'u')(\vec{x},t)\,dt = \frac{1}{T}\sum_{i=1}^{N}(u'u')(\vec{x},t)\Delta t \qquad (81)$$

The turbulent kinetic energy is defined as

$$k(\vec{x}) = \frac{\overline{u'u'(\vec{x})} + \overline{v'v'(\vec{x})} + \overline{w'w'(\vec{x})}}{2} \qquad (82)$$

The spatial averaged velocity profile in spanwise direction is defined as

$$u'u'(y) = \frac{1}{L_z}\int_{L_z} u_i' u_i'(y,z)\, dz = \frac{1}{L_z}\sum_{i=1}^{N} u_i' u_i'(y,z)\Delta z \qquad (83)$$

Following the same procedure as time averaging, the spatial averaged turbulent kinetic energy is

$$k(y) = \frac{\overline{u'u'(y)} + \overline{v'v'(y)} + \overline{w'w'(y)}}{2} \qquad (84)$$

For the two phase flow analysis, an additional field-indicator function is introduced. Since the bubble is kept at fixed position using PID bubble controller, the averaged velocity inside the bubble would be approximately equal to zero which would cause an abrupt change of velocity profile and lead to unrealistic results. This phenomenon exists in the experiment as well. In the experimental measurement using hot film anemometer [16, 134], the signal delivered by a hot film probe in bubbly flow is very spiky, owing to the abrupt change of heat transfer at the crossing of the interface. It is necessary to remove the peaks from the signal before calculating the turbulence intensity. Lance and Bataille [16] distinguished the gas phase by the inspection of the amplitude of the quantity $\left(\frac{\partial u_l'^2}{\partial t}\right)^2$. A threshold value was chosen, above which the characteristic function was set equal to zero. This value was fitted so that the mean value of the characteristic function was equal to the local void fraction measured by the optical probe. In our case shown in Figure 19, we exclude the probes inside the circle with 1.2 bubble diameter for data averaging as shown below. Figure 20 shows the results of sensitivity analysis. The bubble-induced turbulence versus streamwise position is plotted where the bubble is located at $\frac{x}{D} = 3.14$. Four different diameters for data averaging circle are compared and it shows that 1.2D averaging circle can capture the general trend of the bubble-induced

turbulence. Simultaneously, 1.2D is able to exclude the properties transition region on the interface while keeping the information of the liquid velocity field near the bubble. To avoid the numerical instability for the abrupt change of flow properties, the adoption of level-set interface tracking method (Section 2.1.2) introduces a transition region with a smoothed Heaviside function. The verification of the influence of the transition region on the turbulence near the interface is performed as part of this research and provided in Section 4.1.

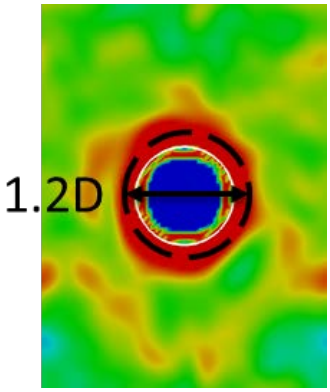

Figure 19. Diagram of averaging algorithm for two-phase simulation. White circle represents the bubble-liquid interface and the probes inside the dashed circle are excluded for the data averaging.

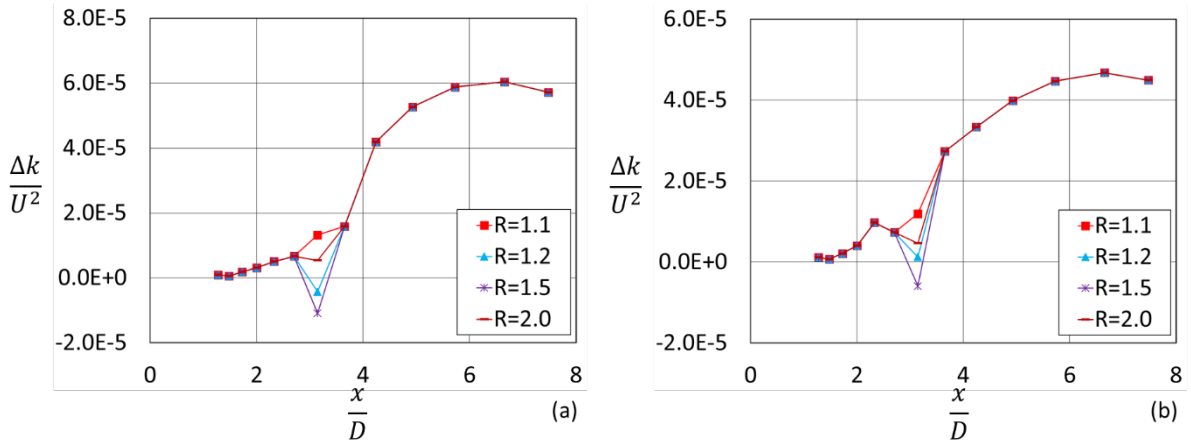

Figure 20. Sensitivity analysis (bubble-induced turbulence versus streamwise position) of screening windows for two different bubble deformation levels, We=1.35 (a) and 2.03 (b). The diameter of the exclusion circles are 1.1, 1.2, 1.5, and 2.0D.

CHAPTER 3. INTERFACIAL FORCES EVALUATION

The results of the lift and drag force evaluation in both laminar and turbulent flow are provided in this section. The evaluation of the lift force in laminar shear velocity field is conducted to verify and validate our methodology. Set of parametric studies are conducted to evaluate the drag force in homogeneous no-shear turbulent flow conditions. We propose a new drag closure law based on the obtained set of results. The modification of the interfacial closures due to the wall presence are investigated as well and presented in this chapter.

3.1 Evaluation of lift force under laminar shear flow

In the present work we systematically evaluate the interfacial forces acting on a bubble in various conditions. We numerically analyze the lift force acting on a single bubble in shear flow with the exactly same parameters as Tomiyama's experiment did [2], including bubble diameter, shear rate and surface tension to validate our approach against the experimental data. By applying the appropriate relative velocity, we can maintain the Earth gravity (in order to mimic experimental conditions) and the same extended bubble diameter as shown in Figure 2. The estimation of relative velocity is based on the force balance between buoyancy force and drag force.

$$F_D = F_b \tag{85}$$

$$\frac{1}{2}\rho_l A u_r^2 C_D = V\left(\rho_l - \rho_g\right)g \tag{86}$$

$$g = \frac{3}{4}\frac{\rho_l}{\rho_l - \rho_g}\frac{C_D u_r^2 D_H^2}{D^3} \quad (87)$$

with C_D is the drag coefficient, u_r is the relative velocity, D is the spherical bubble diameter, D_H is the extended bubble diameter. If we assume the ratio of D_H to D to be a constant, then the Eq. (86) can be simplified as

$$g \sim \frac{C_D u_r^2}{D} \quad (88)$$

The validation of this assumption depends on the flow conditions. For spherical bubble, the ratio of D_H to D remains constant, close to 1, while for deformable bubble, the value of the ratio can be slightly larger than 1. Our simulation results show that the value of $\frac{D_H}{D}$ is within the range of 1.04~ 1.32 for different deformable bubble shapes.

Tomiyama's drag coefficient correlation is based on the bubble Reynolds number.

$$C_D = \min\left\{\frac{16}{Re_b}(1 + 0.15Re_b^{0.687}), \frac{48}{Re_b}\right\} \quad (89)$$

This way gravity can be evaluated as:

$$g \sim \min\left\{\frac{16u_r\mu}{D^2\rho}\left(1 + 0.15\left(\frac{\rho u_r D}{\mu}\right)^{0.687}\right), \frac{48\mu u_r}{\rho D^2}\right\} \quad (90)$$

Since the fluid properties are constant in this case, the value of the gravity can be expressed as $g = g(D, u_r)$. Based on the expression of the gravity, we can observe that as the bubble diameter increases, the relative velocity is expected to increase to get the corresponding Earth gravity.

The proposed velocity profile is $(3.8y + u_r)$ *m/s* and the shear rate is identical to the physical experiment performed in [2]. The relative velocity, u_r, is case dependent and based

on the force balance as discussed above. We apply uniform shear inflow velocity condition on the streamwise direction, constant velocities on the top and bottom surface in lateral direction and natural pressure on the outflow surface. The surface tension is $0.061\ \frac{N}{m}$. The air properties are based on 25 ^{o}C and 1 atm which are identical to the experiment setup as well.

In order to capture the curvature behavior of a deformable bubble, we propose to use the unstructured / locally refined mesh instead of structured / spatially uniform Cartesian mesh approach. The advantage to use the unstructured mesh capabilities [147] is that we could define a specific refinement region which helps us increase the mesh resolution in the region containing bubble while maintaining the total mesh size within the computational capabilities. The selected spherical bubble diameters are *2.84 mm, 3.52 mm, 4.16 mm, 4.85 mm and 5.54 mm,* which are identical to the experiment.

3.1.1 Mesh independence study

The mesh refinement study was completed to ensure that the bubble control algorithm was built and implemented properly. For this study, the bubble diameter of *5.54 mm* case is simulated with five different mesh resolutions to verify lift and drag results. The mesh configuration is shown in Figure 21. The number of elements across the bubble diameter used for the study are 25, 35, 45, 55 and 65. It should be mentioned that in order to balance the mesh cost while maintaining consistent study, the finest mesh region is compressed in the streamwise direction for the 65 elements case. However, as shown in the part (f) of Figure 21, the entire bubble is kept in the finest mesh region when the bubble reaches a steady state.

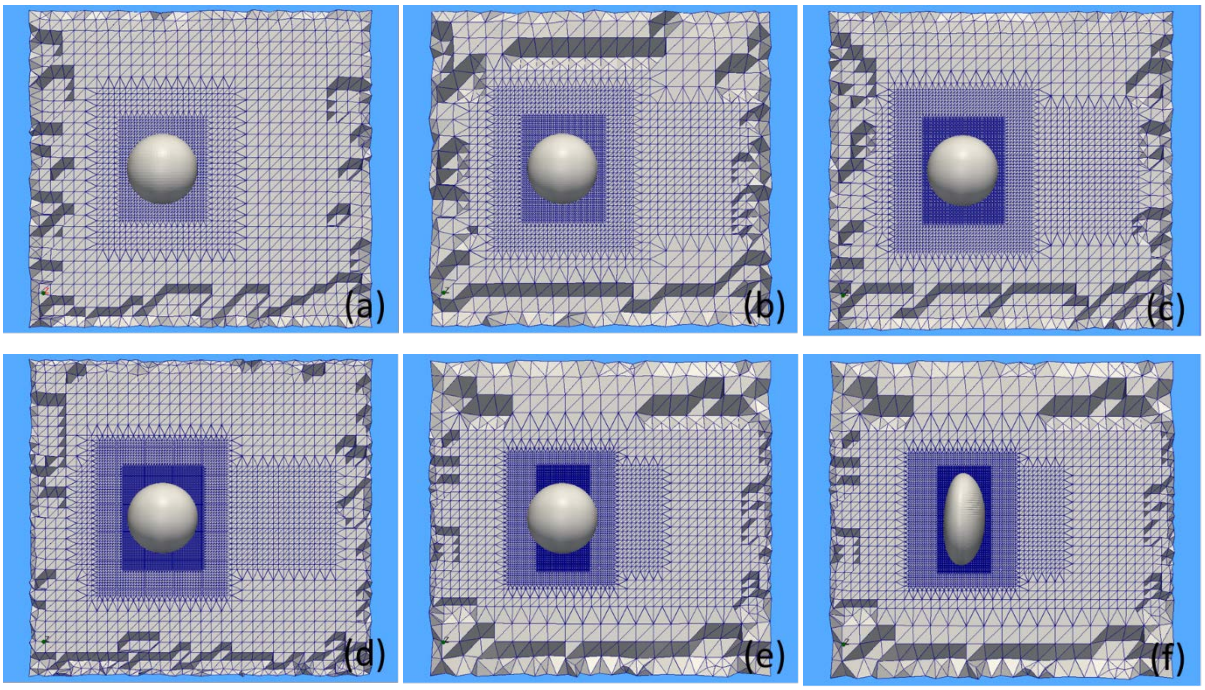

Figure 21. Mesh configuration of the mesh study cases. The images from (a) to (d) represent the case with 25, 35, 45 and 55 elements across bubble diameter. Both (e) and (f) represent the case with 65 elements across equivalent spherical bubble diameter.

The comparison of control forces is given in the Figure 22 and Figure 23. It shows that the control force evolution for 25 elements case is slightly different from the other cases. As the resolution increases, the cases reach consistent interfacial force results.

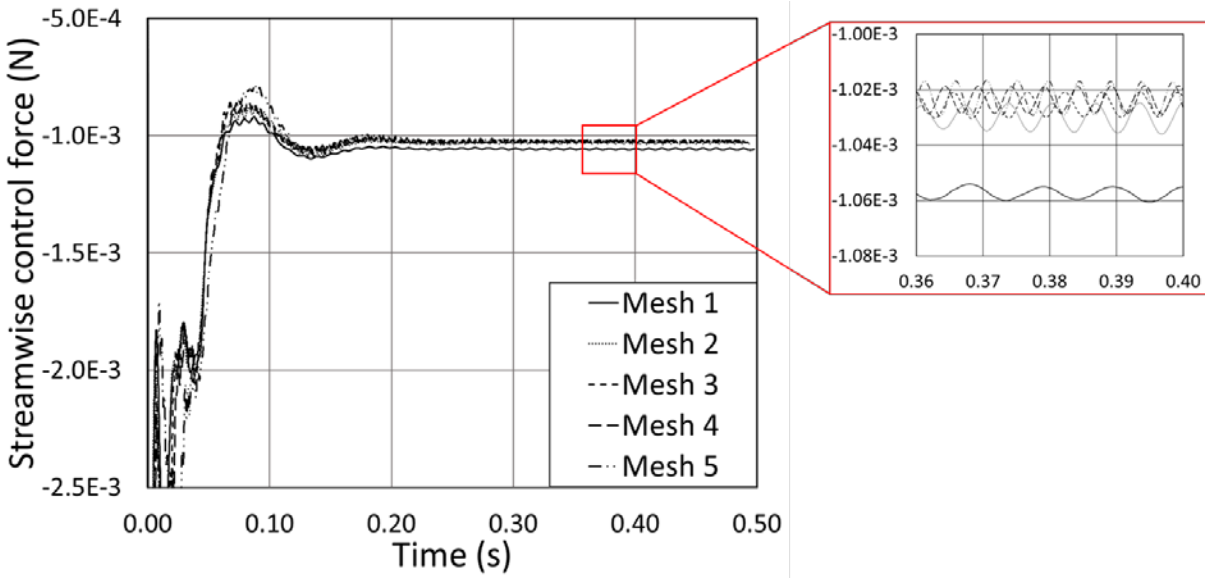

Figure 22. Comparison of control force in streamwise (x) direction for mesh study. Mesh type 1 to 5 represent the 25, 35, 45, 55 and 65 elements across bubble diameter, respectively.

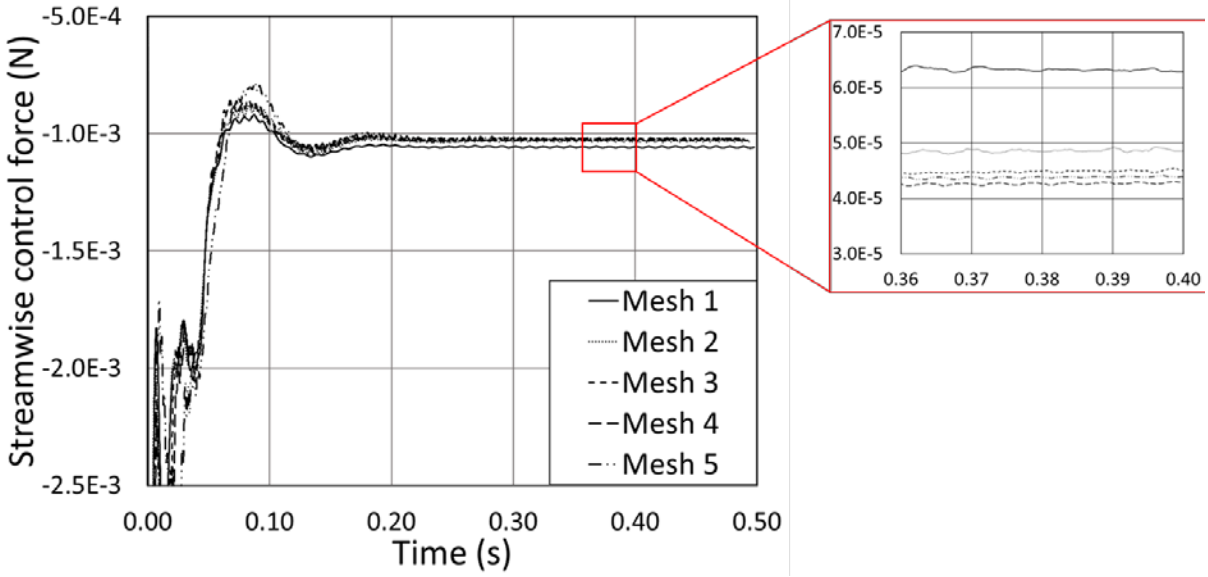

Figure 23. Comparison of lateral control force in lateral (y) direction for mesh study. Mesh type 1 to 5 represent the 25, 35, 45, 55 and 65 elements across bubble diameter, respectively.

The control force is averaged from 0.3 s to 0.5 s, where the bubble reaches a quasi-steady state. The drag and lift coefficients are calculated as well and provided in the Table 4. For 45, 55 and 65 elements resolution cases, the drag coefficient difference among the cases is very small and can be ignored. The lift coefficient variation is within 2.5% for the same cases. Thus, based on the mesh study, 45 elements across bubble diameter is precise enough to ensure that the control forces are converged while maintaining reasonable computational cost.

Table 4. Summary of the mesh study results.

Total mesh size (million)	0.3	1.1	2.3	3.1	3.8
Computational cost (wall-clock hours)	7.0	24.5	64.8	126.7	158.1
Number of elements across bubble diameter	25	35	45	55	65
Number of elements across interface	1.98	2.48	3.20	3.92	4.62
Drag force (10^{-3}N)	1.057	1.030	1.026	1.024	1.023
Lift force (10^{-5}N)	-6.309	-4.881	-4.494	-4.282	-4.400
Drag coefficient	0.788	0.769	0.765	0.763	0.763
Lift coefficient	-0.598	-0.463	-0.426	-0.406	-0.417

The convergence of the results is evaluated using standard grid convergence index (GCI) [173]. This is an approach to examine the spatial convergence of a numerical simulation. The order of grid convergence involves the behavior of the solution error defined as the difference between the discrete solution and the exact solution:

$$E = f(h) - f_{exact} = Ch^p + H.O.T. \quad (91)$$

where C is a constant, h is some measure of grid spacing, p is the order of convergence and *H.O.T.* represents the higher order terms of truncation error. A direct evolution of p can be obtained from three solutions using a constant grid refinement ratio r

$$p = \ln\left(\frac{f_3 - f_2}{f_2 - f_1}\right)/\ln(r) \quad (92)$$

where f_i represents the calculated drag coefficient in the presented research and r represents the ratio of the number of elements across bubble diameter between two adjoint mesh setups.

Roache [174] defines a grid convergence index (GCI) to provide consistent manner in reporting the results of grid convergence studies and it is based upon a grid refinement error estimator derived from the theory of generalized Richardson Extrapolation [175, 176]. The GCI on the fine grid is defined as

$$GCI_{fine} = \frac{F_s|\varepsilon|}{r^p - 1} \quad (93)$$

where F_s is a factor of safety. The factor of safety is recommended to be 3.0 for comparisons of two grids and 1.25 for comparisons over three or more grids. The GCI for the coarser grid is defined as

$$GCI_{coarse} = \frac{F_s|\varepsilon|r^p}{r^p - 1} \quad (94)$$

Based on the Eq. (92) to (94), we calculate the GCI of drag coefficient for different mesh setup and it is shown in Figure 24. As the mesh resolution increases, the results approach the true solution. Based on the mesh study, 45 elements across bubble diameter is enough to ensure that the control force is converged while maintaining reasonable mesh cost. All the

mesh study cases were carried out using 64 processing cores and the computational cost is provided in Table 4.

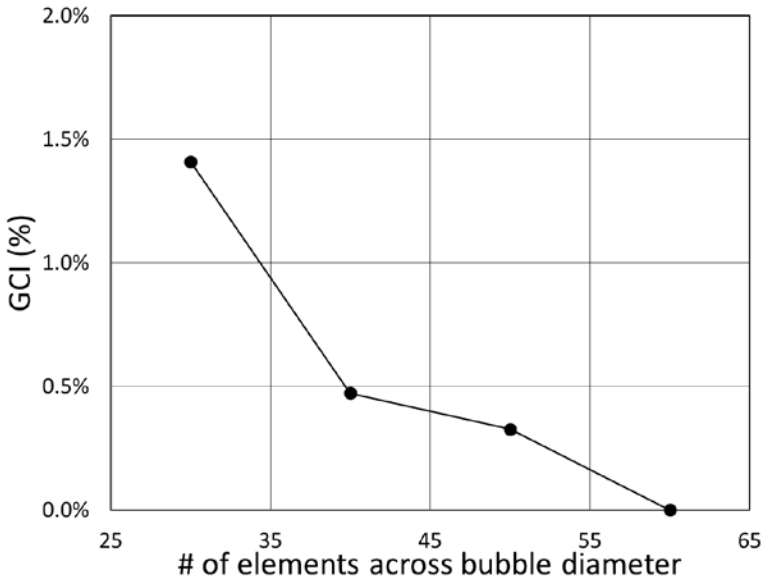

Figure 24. GCI of drag coefficient versus various mesh setups.

3.1.2 Results and discussion

Due to the various bubble sizes, the mesh and geometrical configuration are case dependent while we keep 45 elements across the bubble diameter to get consistent results. The mesh configuration of the unstructured mesh model case with diameter of *2.84 mm* is given in Figure 25. The detailed information of the case setup is given in Table 5. The initial spherical bubble diameter and shear velocity field are created to be exactly same as in experimental conditions. This way, we obtain a direct validation of DNS results with the experimental results.

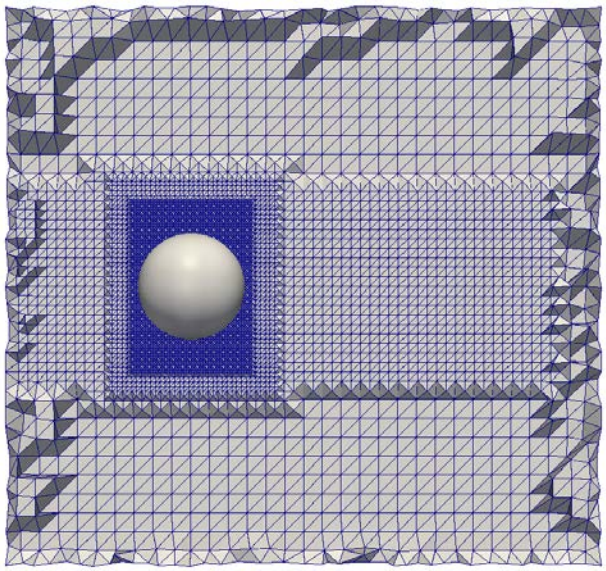

Figure 25. Mesh configuration of the Parasolid model case with D=2.84 mm.

Table 5. Case setup of lift force evaluation study.

Case #	1	2	3	4	5
Bubble diameter (mm)	2.84	3.52	4.16	4.85	5.54
Simulation domain (mm^3)	16×15×15	18×18×18	20×20×20	27×25×25	27×25×25
Number of mesh across bubble diameter	45	45	45	45	45
Total mesh size (million)	2.19	1.84	2.59	2.19	2.33

The PID controller is applied to balance the drag force and lift force. After getting the instantaneous control force history from the controller, we average the control force and calculate the corresponding coefficients based on Eqs. (23) and (31). After the initial transition, the control forces reach a statistically steady state where we extract and average the control forces over a certain amount of simulation time. To discuss the magnitude of bubble deformability, a dimensionless number, i.e., Eotvos number, is calculated based on Eq. (34).

At the same time, some researchers use modified Eo number, Eo_H, for deformable bubble and replace spherical bubble diameter with extended bubble diameter, D_H, in their approach.

The results from the simulation are compared and validated with the experimental measurements and the details are given in Table 6. The extended bubble diameter and Eo number obtained from the simulation are quite close to the experiment. The relative error of the measured extended bubble diameter and Eo number between simulation and experiment are within 1.4% and 9.3%, respectively.

Table 6. Statistics of the simulation and experiment results for the lift force evaluation study.

Case number	Simulation							Experiment		
	V_r(m/s)	D(mm)	D_H(mm)	Eo	g	C_D	C_L	D(mm)	D_H(mm)	Eo
1	0.160	2.84	2.96	1.54	9.86	1.131	0.317	2.84	2.98	1.54
2	0.198	3.52	3.97	2.58	10.74	0.852	0.145	3.52	3.96	2.36
3	0.200	4.16	4.87	3.24	9.65	0.879	0.028	4.16	4.88	3.30
4	0.219	4.85	6.10	4.45	9.73	0.722	-0.173	4.85	6.07	4.48
5	0.220	5.54	7.30	5.96	9.99	0.765	-0.426	5.54	7.20	5.85

The evolution of the control force is given in Figure 26 and Figure 27. Since the drag force is proportional to the bubble cross-sectional area and velocity square which is shown in Eq. (23), the drag force will increase as the bubble size and relative velocity increases. Figure 27 also demonstrates that as the bubble diameter increases which leads to larger Eo value, the bubble becomes more deformable and the migration direction is switched. This is consistent with the experimental data [2, 8].

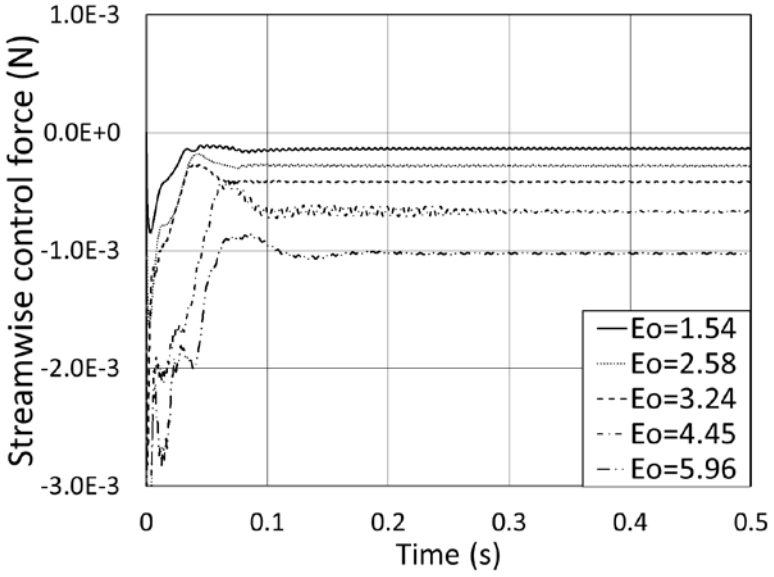

Figure 26. Evolution of control force in streamwise (x) direction for the lift force evaluation study.

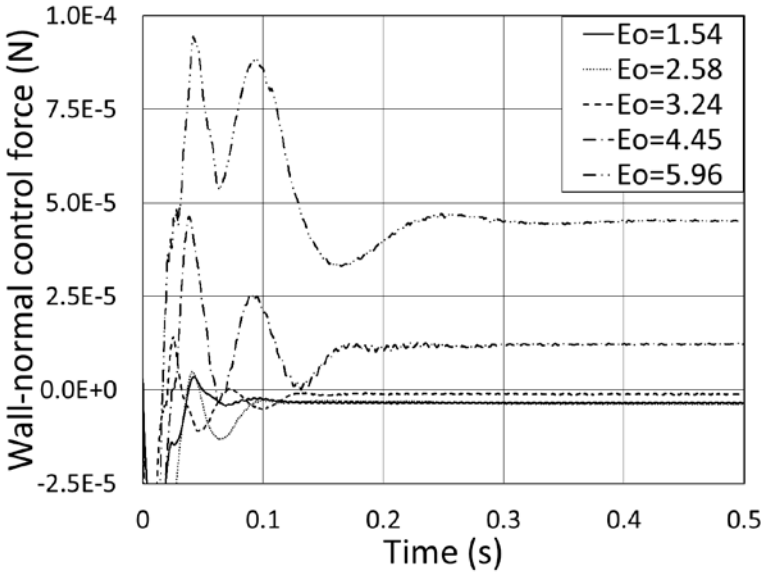

Figure 27. Evolution of control force in lateral (y) direction for the lift force evaluation study.

As the shear flow interacts with the bubble, the streamlines will form vortex in the wake region which serves as an indicator for the direction of the lift force. We used tracer filter in Paraview [162] to show the shape of vortex behind the bubble which is given in Table 7.

Table 7. Comparison of the simulation and experiment results for lift force evaluation study.

Tomiyama's experiment	Simulation results	Streamlines around the bubble	Lift coefficient
	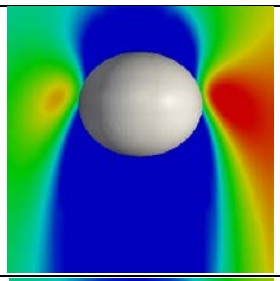	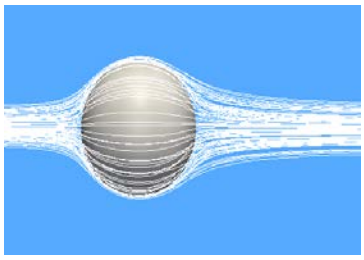	C_L = 0.317
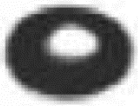	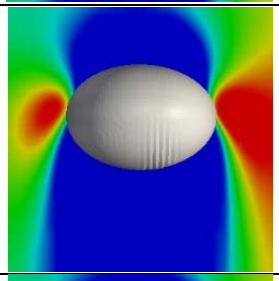	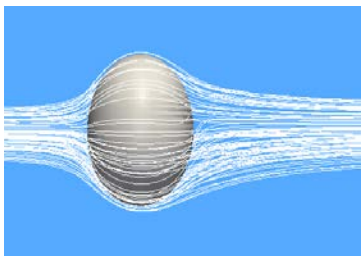	C_L = 0.145
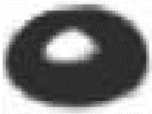	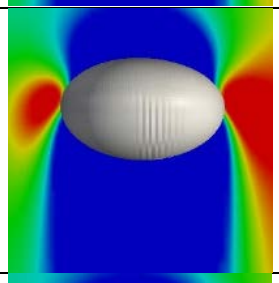	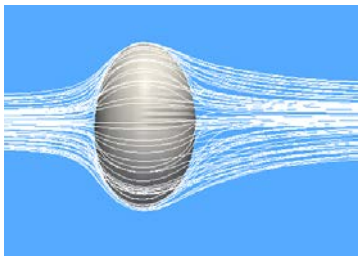	C_L = 0.028
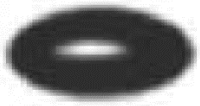	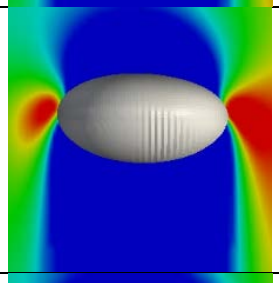	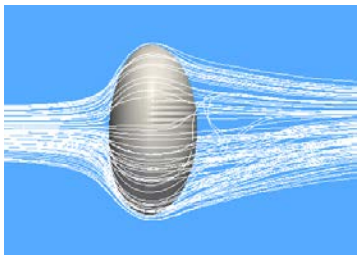	C_L = -0.173
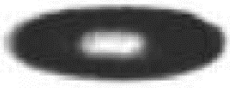	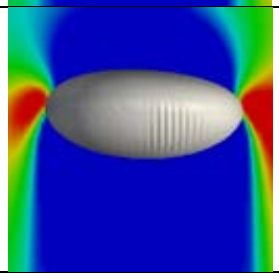	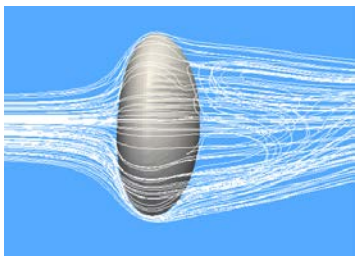	C_L = -0.426

Table 7 shows that for small bubble diameters, i.e., *2.84 mm*, *3.52 mm* and *4.16* mm, the streamlines behind the bubble are almost symmetric along the central line, which indicates small lift force in the y direction which is consistent with the Figure 28. However, for large bubble diameter, i.e., higher *Eo* number, the bubble experiences lift force sign change and tends to migrate in +y direction. It has been shown here that the migration direction change of the bubble in shear field is related to the presence of a slanted wake behind the deformable bubble which is caused by the interaction between the wake and shear field. Comparing the cases with diameter of *4.85 mm* and *5.54 mm*, the strength of vortex is stronger and the magnitude of lift force is increasing. There is no symmetric structure forming behind the deformable bubble. Those observations are consistent with the plot of lift force shown in Figure 27. The lift coefficients for different bubble sizes are provided as well. The bubble shapes from simulation are compared with the images from experiment in Table 7. The results demonstrate very good agreement. The difference of extended bubble diameter between simulation and experiment is within 1.5% for any one of the five cases.

The lift coefficient from our DNS results is compared with Dijkhuizen et al.'s data [8] and Tomiyama et al.'s data [2]. Figure 28 shows that the general trend of lift coefficient versus Eo_{H} follows Tomiyama, however, our results has a slightly lower value of lift coefficient. Tomiyama predicts the transition happens at $Eo_H = 6$, while in our cases it is around 5 with Eo_H. For spherical bubble, our results fit Dijkhuizen data and overpredicts the lift coefficient for more deformable bubble. Dijkhuizen attributed the difference to the surface contamination in the process of shear generation. Experiments often surfer from factors which are difficult to control such as the effect of contaminants, which affects the slip conditions at

the bubble surface. In Dabiri et al.'s simulation [177], the authors used Eo to discuss bubble deformation and the lift sign change was observed at $Eo = 2.5$. In our case, the lift sign change happens at $Eo = 3.4$ shown in Figure 28(b). To summarize, the transverse migration of bubble behavior is observed and validated in our DNS simulations. The trend follows Tomiyama's data and the estimated lift coefficient is slightly smaller compared to Tomiyama's.

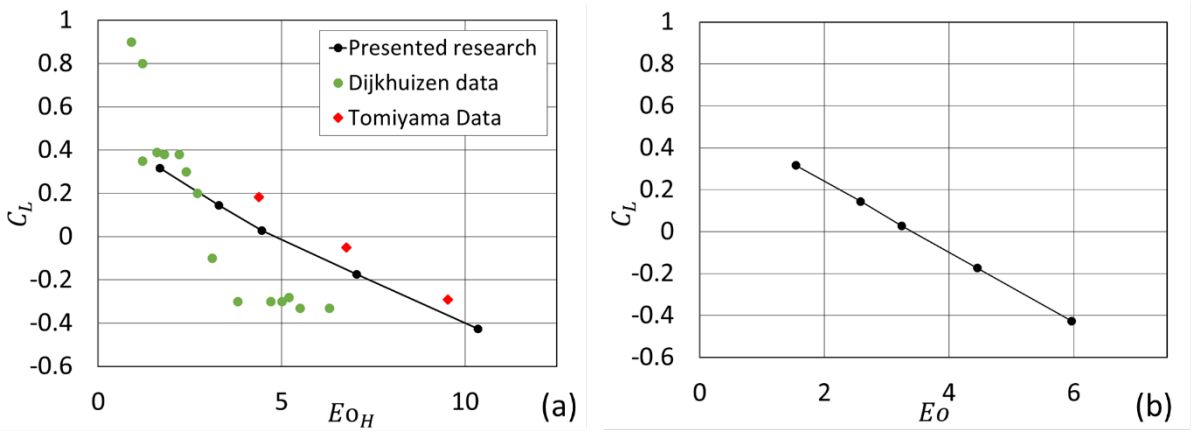

Figure 28. Lift coefficient versus Eotvos number. (a) shows the C_L versus Eo_H for different experiment data and DNS simulation; (b) shows the C_L versus Eo from DNS simulation.

3.2 Evaluation of wall effect under laminar shear flow

In this section, we will expand the scope of the previous study by analyzing the effects of wall presence, bubble Reynolds number and bubble deformability over a wide range of parameters. Those quantities are varied within the range of $0.625 \leq L/D \leq 2.5$, $10.7 \leq Re_b \leq 43.3$, and $0.79 \leq Eo \leq 5.75$. L/D represents the dimensionless wall distance between the bubble center and the solid wall boundary. We apply constant shear flow, $V(x) = \omega \times y + u_r$ as the inflow conditions, constant velocity on the top and bottom surface in wall-normal

direction and symmetric boundary conditions in spanwise direction. The setup of the baseline model is based on the case #2 in Table 5.

3.2.1 The effect of wall distance

The wall distance plays a key role on the magnitude of wall effect on the interfacial forces. Thus, we separately place a single bubble at various distances from the top wall while keeping the same relative velocity between liquid and gas. The details of the case setup can be found in Table 8.

Table 8. Summary of the wall distance cases setup.

Dimensional parameters		Dimensionless parameters	
D (mm)	3.52	Eo	2.58
u_r (m/s)	0.198	Re_b	42.3
ω (s^{-1})	3.8	$\frac{L}{D}$	0.625, 0.75, 0.875, 1, 1.25, 1.5, 2, 2.55

Figure 29 shows the evolution of control forces versus time for different wall distances. The existence of top wall increases the drag force thus increasing the drag coefficient shown in Figure 30. Higher drag force indicates that the bubble's migration in the streamwise direction tends to experience higher resistance from the liquid. Thus the wall presence is found to increase the rise velocity compared to liquid streamwise velocity. As the bubble approaches the wall, lift force sign change is observed at L/D about 1.75 which indicates that the wall force influences the bubble migration direction and the sum of lift force and wall force pushes the bubble away from the wall. Figure 30(b) shows that our results agree with Tomiyama's correlation, Eq. (42), for the small wall distance, $L/D < 1$, while it agrees well with the Hosokawa's correlation, Eq. (43), for the large wall distance.

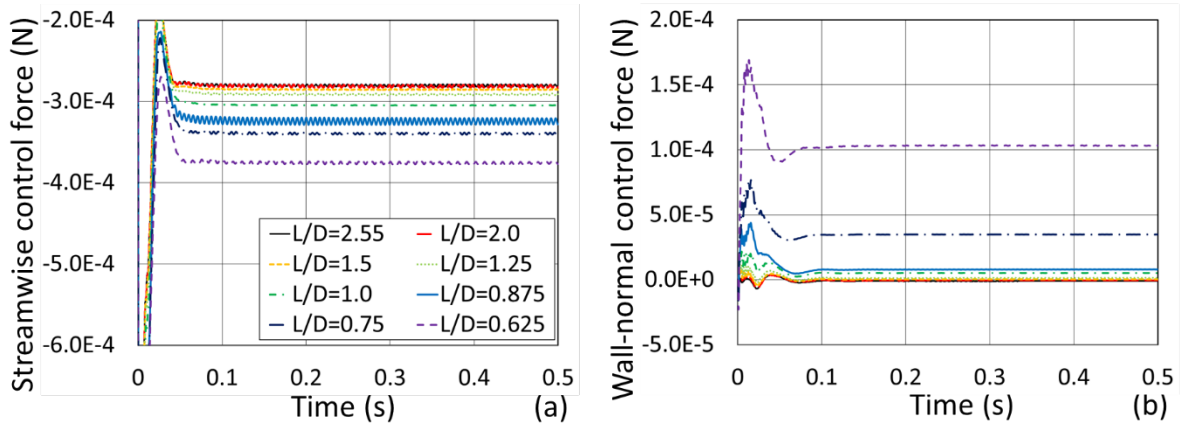

Figure 29. Evolution of the control forces versus different wall distances, L/D.

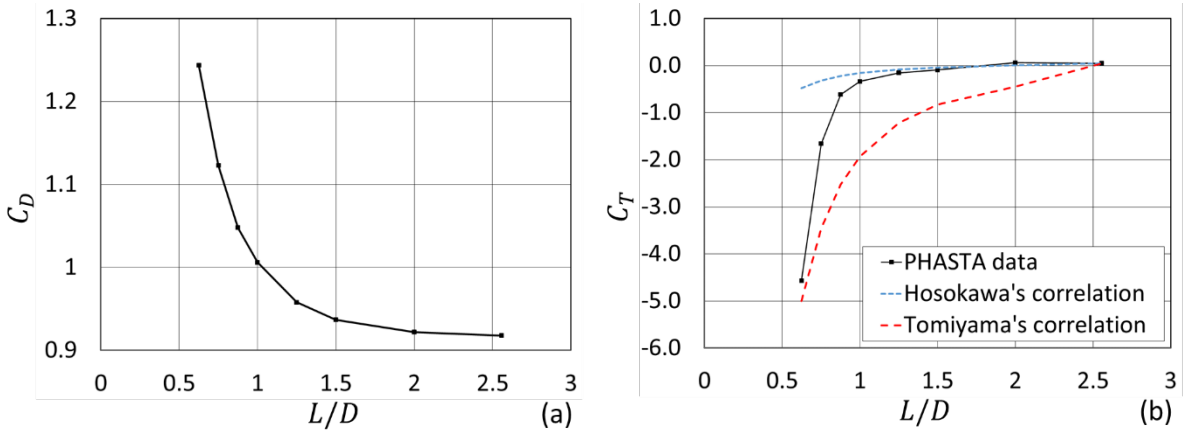

Figure 30. Drag and net lift coefficients (Eq.(46)) versus different wall distances. (a) shows the drag coefficient versus $\frac{L}{D}$. (b) compares the lift coefficient based on the PHASTA data, Hosokawa's correlation, and Tomiyama's correlation.

In Figure 31, we compare the pressure field for selected wall distances. For the bubble located away from the wall, $L/D = 1.25$, the pressure field on the near side and far side of the bubble is quite symmetric. As the bubble approaches the wall, the interaction between the bubble and the wall causes the asymmetric pressure distribution which is responsible for the transverse migration sign change. We also observed that the area of the negative pressure field on the bubble bottom increases as the wall distance decreases. The streamline pattern shown

in Figure 32 demonstrates that a strong vortex is formed below the bubble when the bubble is close to the wall, $L/D = 0.625$. Considering the Bernoulli's equation [178] in incompressible flow, $v^2/2 + gz + p/\rho = constant$, stronger vortex formed below the bubble indicates that higher pressure difference exists across the bubble in the wall-normal direction and the bubble experiences a repulsive force from the wall as it approaches the wall.

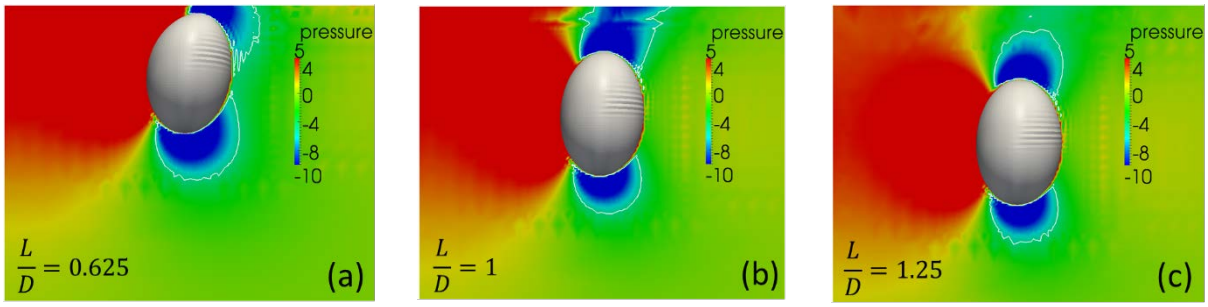

Figure 31. Comparison of the pressure field for different wall distances ($\frac{L}{D} = 0.625$, 1.0 and 1.25) where the white line represents the pressure equal to -5 Pa.

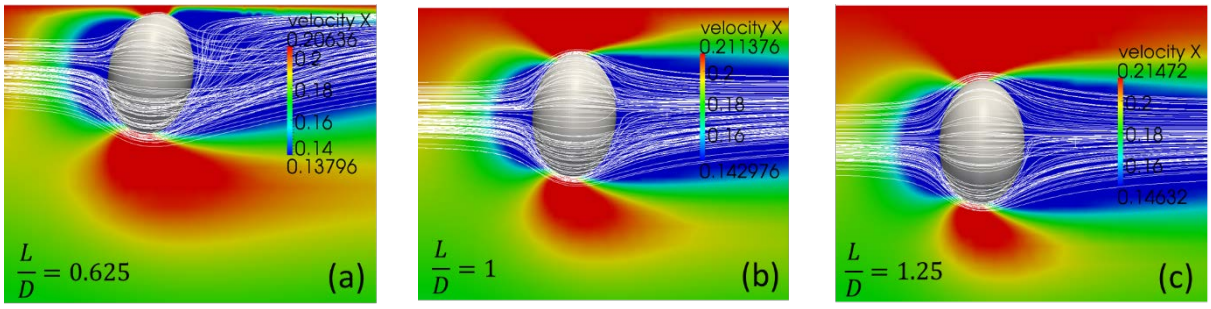

Figure 32. Comparison of the streamline pattern for different wall distances ($\frac{L}{D} = 0.625$, 1.0 and 1.25).

In Figure 31(b), pressure discontinuities are observed near the wall which is due to the transition from fine mesh to coarse mesh. An additional test is performed by extending the refinement region to the wall as shown in Figure 33(b). Figure 34 compares the pressure field for the baseline mesh (1.79 million elements) and the extended refinement mesh (2.23 million

elements). Finer mesh configuration did generate smooth transition of the pressure field. However, a close comparison of the interfacial forces given in Figure 35 demonstrates that the influence of the additional refinement near the wall will not influence the solution. The interfacial forces for these two mesh setups are too close to be differentiated however additional 25% computational cost is needed for the extended refinement case.

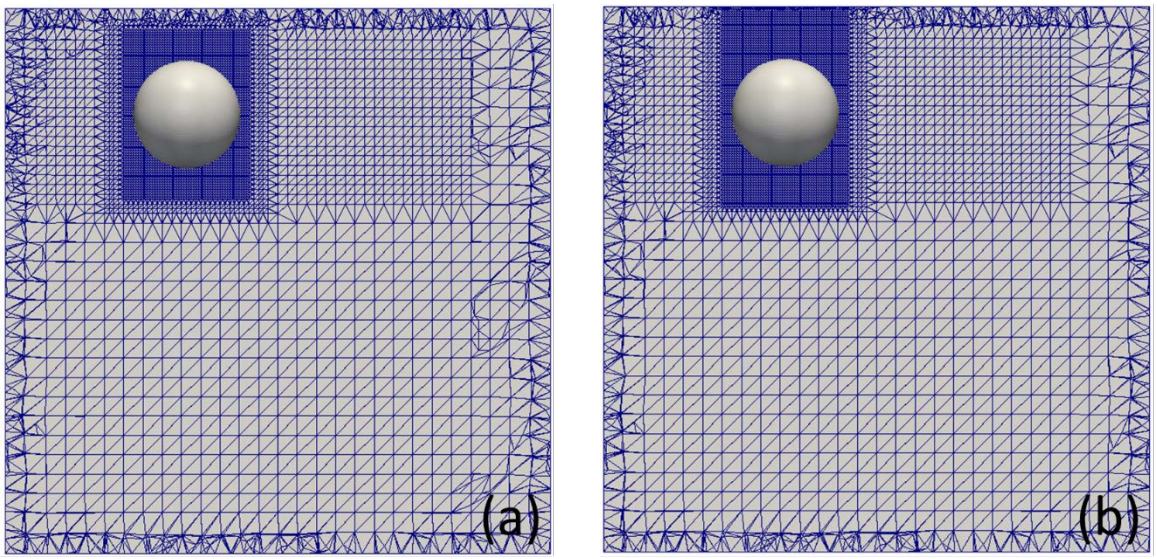

Figure 33. Mesh refinement study. (a) shows the baseline mesh used in the wall distance study. (b) shows the case with extended mesh refinement region.

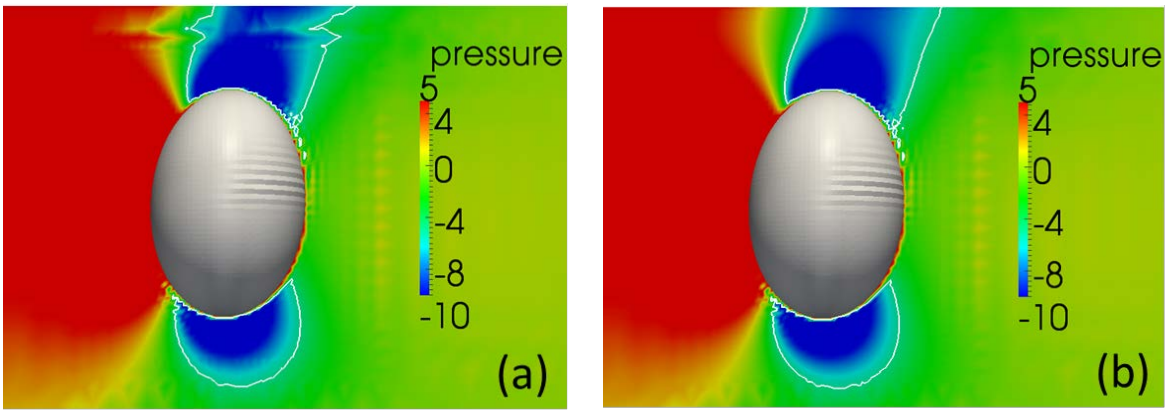

Figure 34. Comparison of the pressure fields for baseline mesh and extended mesh configurations.

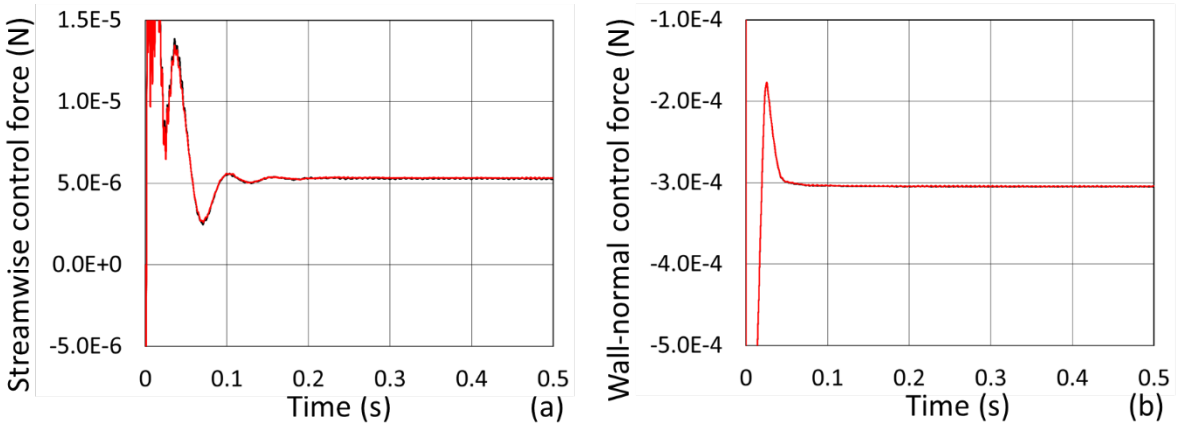

Figure 35. Comparison of the control forces for baseline mesh (black line) and extended mesh (red line) configurations.

3.2.2 The effect of relative velocity

Experimental results [68, 102] indicated that the wall force coefficient is a function of the bubble Reynolds number Re_b and the Eotvos number Eo. In this section we present the study on the bubble Reynolds number effect. We select the case with $L/D = 1$ and apply a series of different relative velocities corresponding to the set of Re_b from 10.7 to 42.3. The surface tension value is adjusted for each case to have constant Weber number of 1.50. Weber number, $We = \rho u_r^2 D/\sigma$, serves as a good measurement for the bubble shape when only the relative velocities are varied [79]. The details about the case setup can be found in Table 9.

Table 9. Summary of the bubble Reynolds number cases setup.

Dimensional parameters		Dimensionless parameters	
D (mm)	3.52	Eo	2.58
u_r (m/s)	0.05, 0.1, 0.15, 0.175, 0.198	Re_b	10.7, 21.4, 32.1, 37.4, 42.3
ω (s^{-1})	3.8	L/D	1

Figure 36 shows the evolution of the control forces for different bubble Reynolds numbers. The drag and net lift coefficients versus bubble Reynolds number is given in Figure

37. In Figure 37(a), we compare the drag coefficient obtained from the PHASTA simulation and the DNS-based drag coefficient closure given in Eq. (107). The discrepancy at high bubble Reynolds number region is due to the wall presence. In Figure 37(b), we observe the sign change of lift coefficient occurs around Re_b of 35. A change of the lift force direction due to the bubble Reynolds number was also experimentally observed by Takemura and Magdaudet [102] and the transition happens at Re_b of 35. Figure 38 compares the velocity field around the bubble with different relative velocities. By keeping the constant Weber number, the bubble shape is nearly identical for those cases. At low Reynolds number, the influence of wall presence dominates the bubble migration direction. However, when the inertia effects are dominant (the increasing high velocity field on the bubble bottom region shown in Figure 38), the velocity field is essentially confined in the boundary layer and the wake of the bubble. Our study shows that the influence of both wall distance and bubble Reynolds number leads to the bubble bouncing behavior near the wall.

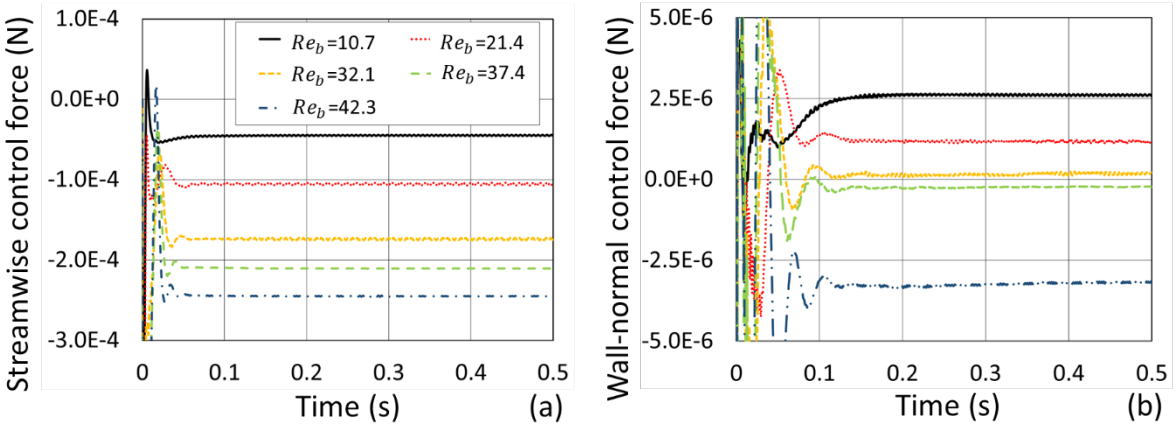

Figure 36. Evolution of control forces versus bubble Reynolds number.

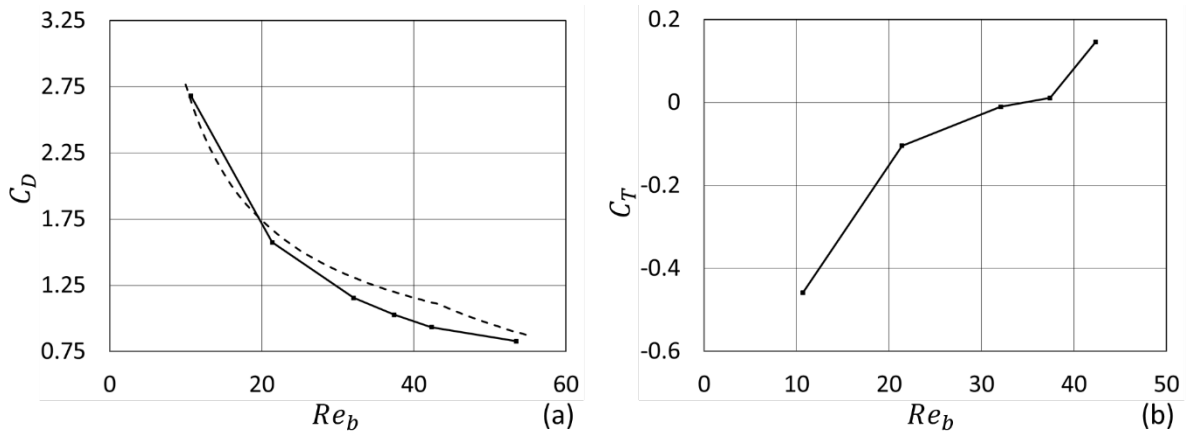

Figure 37. Drag and net lift coefficients versus Re_b. The drag coefficient from PHASTA data (solid line) is compared with the DNS informed correlation (dash line), Eq. (107).

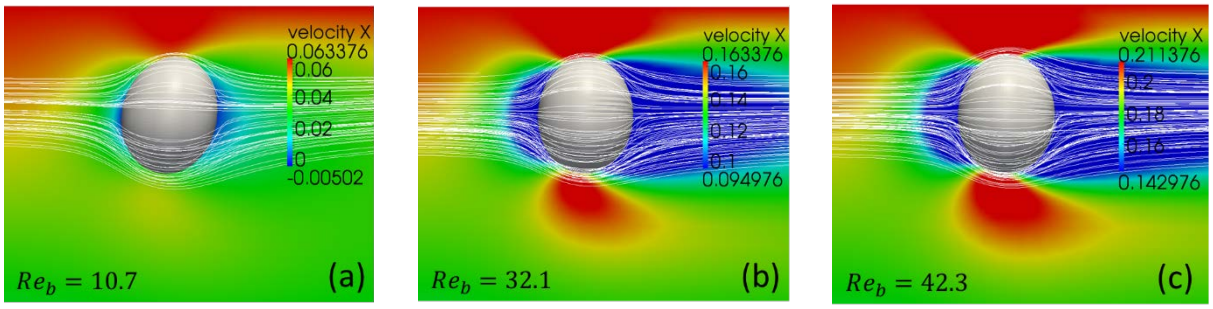

Figure 38. Comparison of velocity field for different bubble Reynolds numbers. The range of legend for each figure is based on the velocity profile, $V = 3.8 \times y + u_r$ and the values of u_r are different for each case.

3.2.3 The effect of bubble deformation

The lift sign change due to the bubble deformation has been reported at $Eo = 3.4$ in the previous study [56] without considering wall effect. The interaction between the bubble and the wake region causes the different migration behaviors of the spherical and deformable bubble. In two-phase upflow, spherical bubble tends to migrate toward the pipe wall whereas the deformable bubble tends to migrate toward the pipe center. As the spherical bubbles

accumulate and coalescence near the wall, the large deformable bubbles are formed and migrate toward the channel center. In this section, we place the bubble at fixed position, $L/D = 1$, with different bubble deformation levels to analyze the integral effect of bubble deformation and wall distance on the interfacial forces. The summary of the case setup is given in Table 10.

Table 10. Summary of the bubble deformation cases setup.

Dimensional parameters		Dimensionless parameters	
D (mm)	3.52	Eo	0.79, 1.76, 2.79, 3.46, 5.75
u_r (m/s)	0.198	Re_b	42.3
Sr (s^{-1})	3.8	L/D	1

Figure 39 compares the control forces for different bubble deformation levels. The control forces reach a steady state and the oscillation is due to the periodic variation of the void fraction. As shown in Figure 40(a), the drag coefficient increases with the bubble deformation because the bubble shape is extended in the wall-normal direction which blocks the flow field and introduces higher drag force. Figure 40(b) compares the net lift coefficient with two wall distances, $L/D = 1$ and 2.55. The transverse migration direction is flipped at $Eo = 2.3$ for the near wall case. Without solid wall boundary, the spherical bubble, $Eo < 3.4$, will migrate toward the channel wall which hydrodynamically corresponds to the top wall in our uniform shear flow simulations. However, the existence of wall repulsive force will push the bubble away from the wall due to the unbalanced pressure field shown in Figure 41. Thus a spherical bubble, $Eo = 2.3$, will experience a change in the lateral force direction near the wall while it will not happen without wall presence. Figure 41 shows that the pressure field in the front of the deformable bubble is tilted and stronger compared to the spherical bubble's. Figure 42 compares the streamline patterns for different bubble deformation levels. Denser streamlines

are formed on the top of spherical bubble while strong vortex is formed behind the deformable bubble.

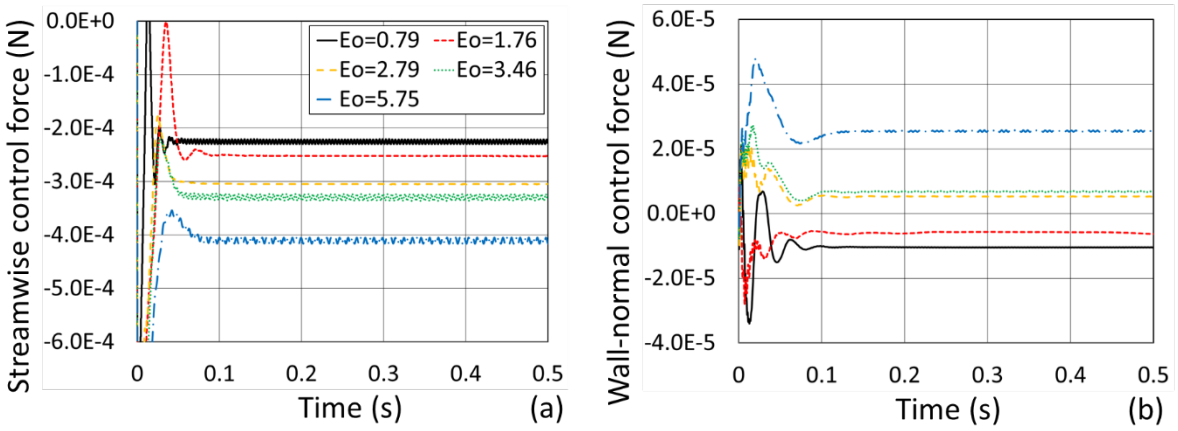

Figure 39. Evolution of the control forces versus bubble deformation levels.

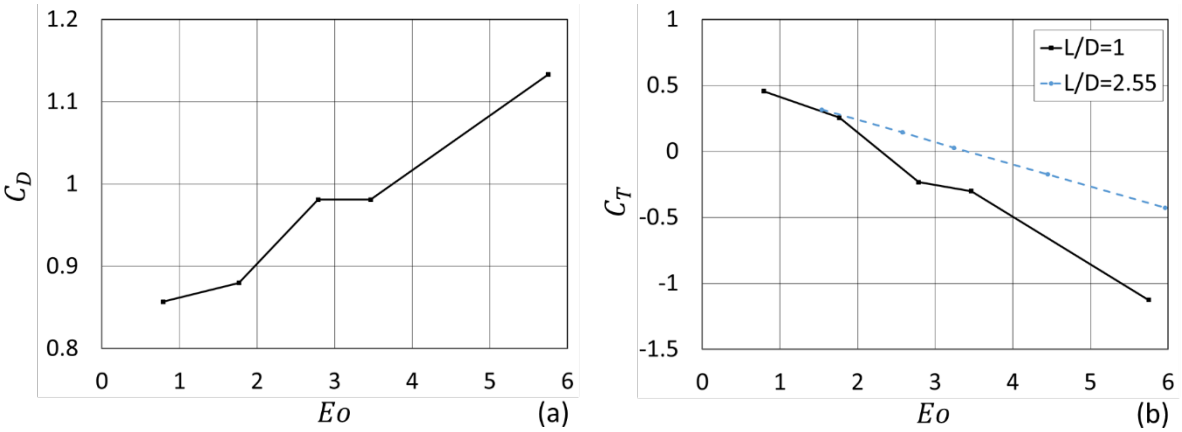

Figure 40. Drag and net lift coefficients versus Eo. (a) shows the drag coefficient versus Eo. (b) compares the lift coefficients with the case where the bubble is far away from the wall, $L/D = 2.55$.

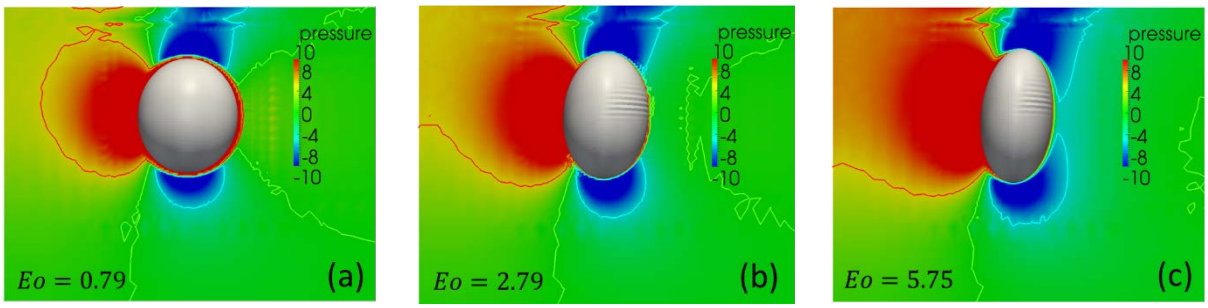

Figure 41. Comparison of pressure fields for different bubble deformation levels. Three pressure contours of 5, 0, and -5 Pa are shown.

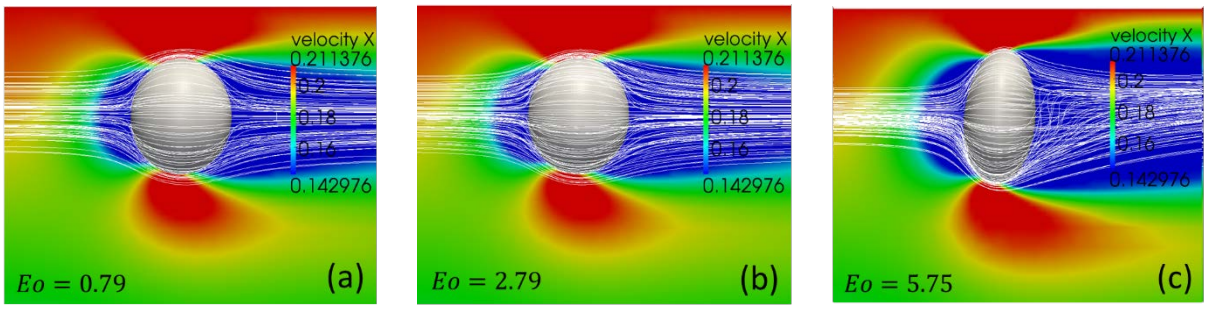

Figure 42. Comparison of streamline patterns for different bubble deformation levels.

The bubble transverse migration behavior is a coupled phenomenon of bubble deformation, wall distance and relative velocity. Figure 43 shows a comprehensive coefficient map as a function of Re_b and Eo for bubble distance $L/D = 1$. In addition to the dataset we mentioned in the previous sections, expanded dataset for high bubble Reynolds number ($50 < Re_b < 100$) and high bubble deformation level ($2.5 < We < 5.0$) are generated to gain a more complete picture. The analytical interpolation generates the following expressions for the prediction of lift coefficient sign

$$\begin{cases} C_L > 0, & if\ Re_b - (30 + 0.6e^{\frac{4}{3}We}) < 0 \\ C_L = 0, & if\ Re_b - (30 + 0.6e^{\frac{4}{3}We}) = 0 \\ C_L < 0, & if\ Re_b - (30 + 0.6e^{\frac{4}{3}We}) > 0 \end{cases} \quad (95)$$

Sugioka and Tsukada's DNS data [101] and Takemura et al.' experimental data [102] for spherical bubble study are also included. Positive and negative lift coefficients are marked with blue and red colors, separately. This map can help us identify the region where the bubble migration direction switches, thus predicting the bubble behavior.

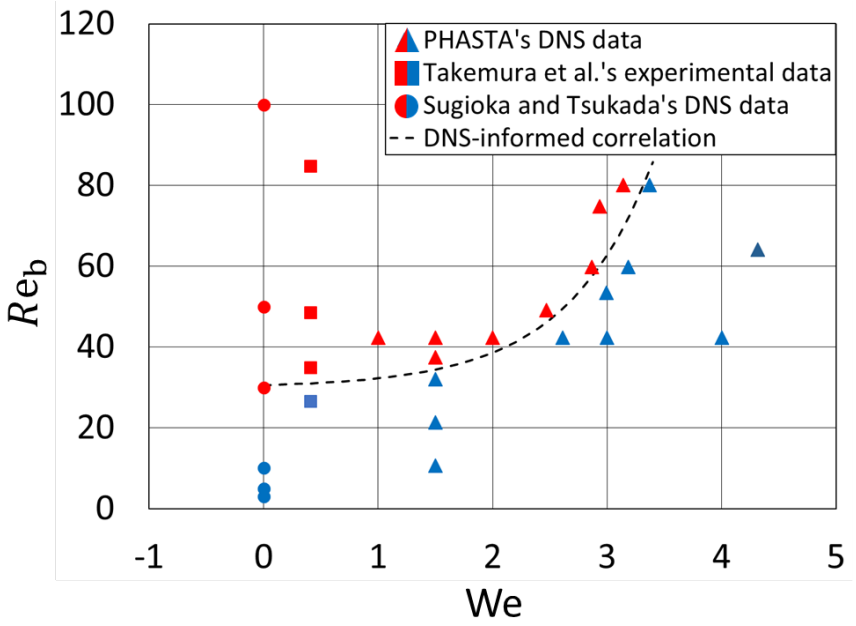

Figure 43. Lift coefficient map $C_L(Re_b, We)$ at $L/D = 1$. Red and blue symbols represent negative and positive lift coefficient, respectively. The data sources are from Sugioka and Sugioka and Tsukada's DNS data (sphere) [101], Takemura et al.'s experimental data (square) [102], and PHASTA's DNS data (triangle).

3.3 Evaluation of drag force under homogeneous turbulent flow

The lift force study provides insight on the transverse migration of bubble in laminar shear flow. Our results are very close to the experimental observation [2]. We now expand our interfacial force study to the turbulent flows, which is a more common flow condition in most engineering applications. We start with the single bubble drag force estimation in homogeneous turbulent flow. Note that in those conditions there is no mean velocity shear and

the only interfacial force acting on the bubble is the drag force. To generate the transient inflow boundary conditions representing fully resolved homogeneous turbulent flow we use the approach described in [80]. To briefly summarize it here, the following steps are performed. First, a single-phase unstructured mesh domain is created with a fully resolved grid of spheres to produce turbulent wakes. We apply a pressure gradient to drive the flow through the grid of spheres to maintain a certain velocity, similar to the typical experimental setup for generating uniform turbulence [16, 63]. Periodic boundary conditions are applied on the inflow and outflow boundaries. After the liquid turbulence level reaches a statistically steady state condition we place a set of virtual probe planes normal to the streamwise direction to record the history of the instantaneous three-dimensional velocity profile. The probes are located at the outflow boundary and the recorded 3D instantaneous velocity field is used as the transient inflow boundary condition for the two-phase single-bubble production simulations. Figure 44 shows the examples of both turbulence-generating (left) and production (right) runs.

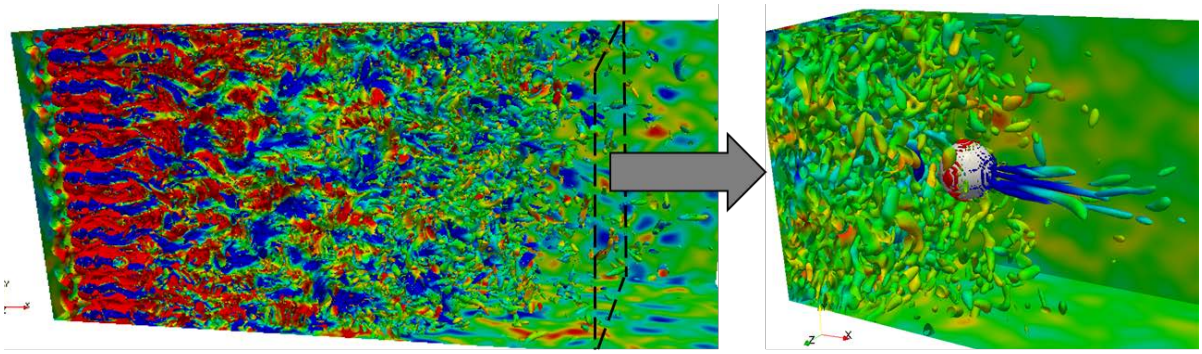

Figure 44. Left image shows the generation of homogeneous turbulent flow. The dashed rectangle indicates the probe plane. The simulation on the right utilizes the inflow recorded on the left.

Uniform distribution of velocity and turbulent kinetic energy (TKE) are observed and shown in Figure 45. The averaged velocity is 0.297 m/s and the averaged turbulent kinetic

energy is 6.74×10^{-5} m^2/s^2. The generation of homogeneous turbulent field was carried out on Mira supercomputer at Argonne Leadership Computing Facilities (ALCF) using 8,192 processing cores over about 100 wall-clock hours. Utilizing the instantaneous velocity profile as inflow condition for two-phase simulation, we are able to analyze the effect of turbulent intensity, bubble deformation and relative velocity on the drag force under homogeneous turbulent flow condition.

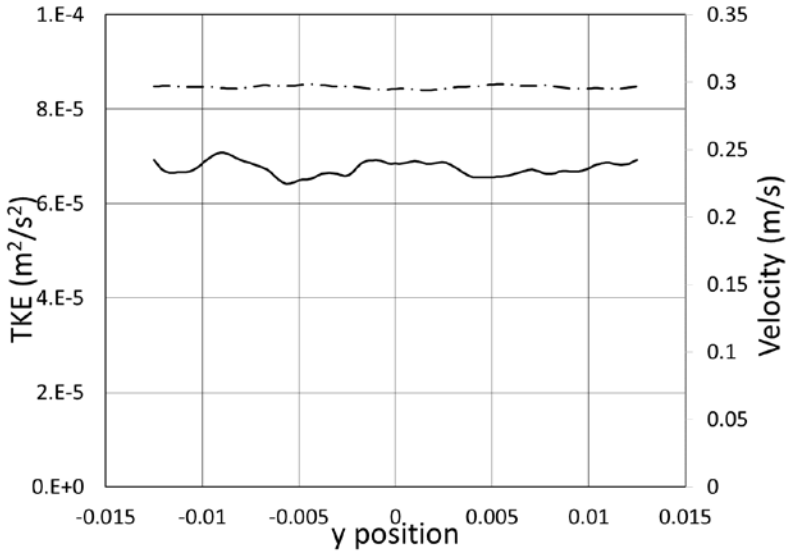

Figure 45. Velocity (dash-dot line) and turbulent kinetic energy (solid line) profiles versus spanwise direction (y) for the single-phase homogeneous turbulent flow.

For the two-phase flow simulation, a single bubble with diameter *D* is placed in the domain with non-dimensional size (*7.5D, 5D, 3D*) as shown in Figure 46. The bubble is located at the center of the normal-to-the-flow plane while the streamwise position is case dependent. For the parametric studies, we keep the mesh configuration identical and only change the flow parameters we want to investigate. Figure 46 shows the simulation domain of the drag force evaluation case together with the mesh configuration of the whole domain.

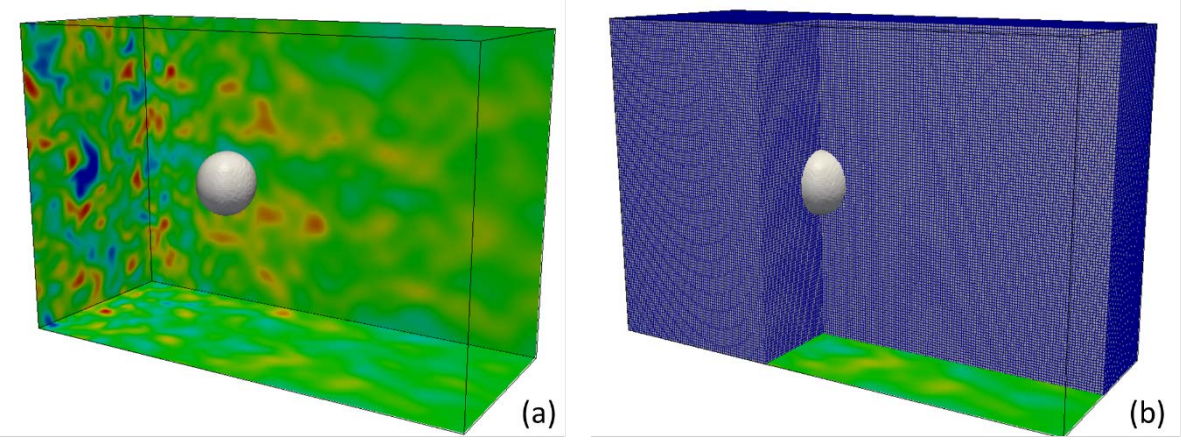

Figure 46. Simulation domain of drag force evaluation case. (a) and (b) show the velocity field and the mesh configuration in the domain.

The domain length is carefully chosen to capture enough flow information upstream and downstream of the bubble. The fluid properties of the simulation cases correspond to water and air at normal temperature and pressure conditions (Table 11).

Table 11. Fluid properties summary for drag force evaluation case.

	Liquid	Gas
Density(kg/m^3)	996.5	1.161
Viscosity ($kg/m \cdot s$)	8.544×10^{-4}	1.845×10^{-5}

PID approach used in our simulation effectively varies the gravity in the domain to maintain the bubble position via buoyancy force. While simulated bubble size is 5 mm, this does not correspond to the realistic bubble size in Earth gravity conditions. To obtain the corresponding bubble size in real physical experiment, we compare the values of the dimensionless number, *Eo*, in both simulated and Earth gravity conditions as shown in the following equations:

$$Eo_r = Eo_s \quad (96)$$

$$\frac{\Delta\rho_r g_r D_r^2}{\sigma_r} = \frac{\Delta\rho_s g_s D_s^2}{\sigma_s} \quad (97)$$

$$D_r = D_s \sqrt{\frac{g_s}{g_r}\frac{\sigma_r}{\sigma_s}} \quad (98)$$

where subscript r represents the real experiment and s is the numerical simulation. Based on the given fluid properties, bubble size and relative velocity, the corresponding bubble diameter in the physical experiment has a range of 0.45~ 1.66 *mm* shown in Table 12, which is close to the range of bubble sizes expected in the light water reactor cores.

Based on our previous research experience [94], the interface tracking method will lead to consistent results with at least 20 elements across the bubble diameter. In this paper, since we will deal with a deformable bubble (1.66 *mm*), we decide to place 25 elements across the bubble diameter to better capture the curvature behavior. The total mesh size is 1.73 million for all the homogeneous two-phase turbulent flow cases.

A PID bubble controller was previously implemented into the PHASTA code to control the bubble at fixed position (with respect to all three axis) and extract the interfacial forces in all three directions. Typically when the bubbles are experimentally observed rising in a standing fluid, they develop wake instabilities and the trajectories of those bubbles are not vertical, but include a transverse motion as well [5]. In order to quantify if the transverse motion of the bubble has an effect on the drag force, a separate simulation has been performed in the presented research by removing the lateral PID control of the bubble. This allows the bubble to freely move in the lateral direction and compare the resultant drag force with the bubble controlled in all 3 directions. Figure 47, Figure 48, and Figure 49 compare the evolution

of bubble position with lateral control force on and off. The drag force results are very close in both cases shown in Figure 50. Based on the mean control force, the drag coefficients are consistent and the relative error is within 2%.

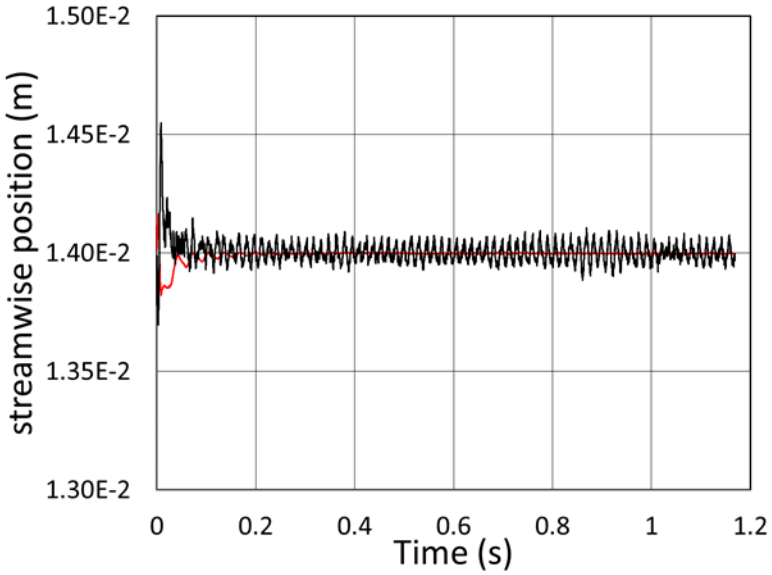

Figure 47. Comparison of the bubble position evolution in streamwise (x) direction with lateral control force (black line) and without lateral control force (red line) for the validation of PID bubble controller.

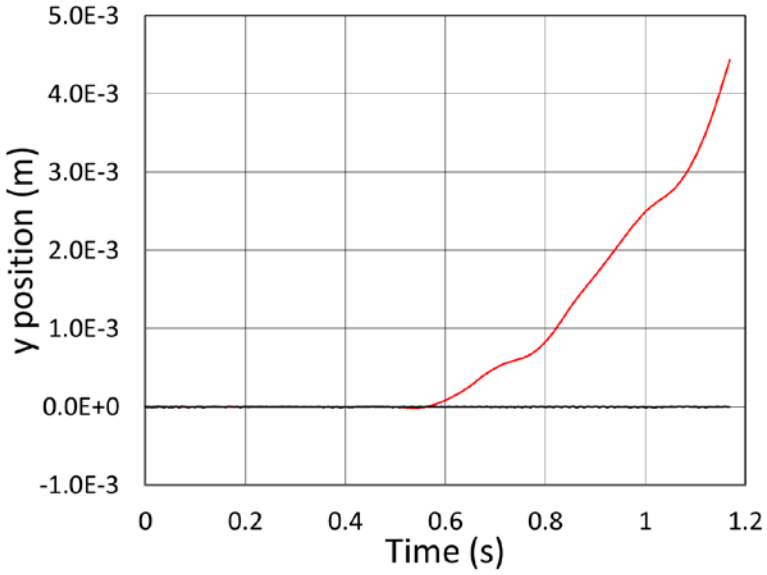

Figure 48. Comparison of the bubble position evolution in y direction with lateral control force (black line) and without lateral control force (red line) for the validation of PID bubble controller.

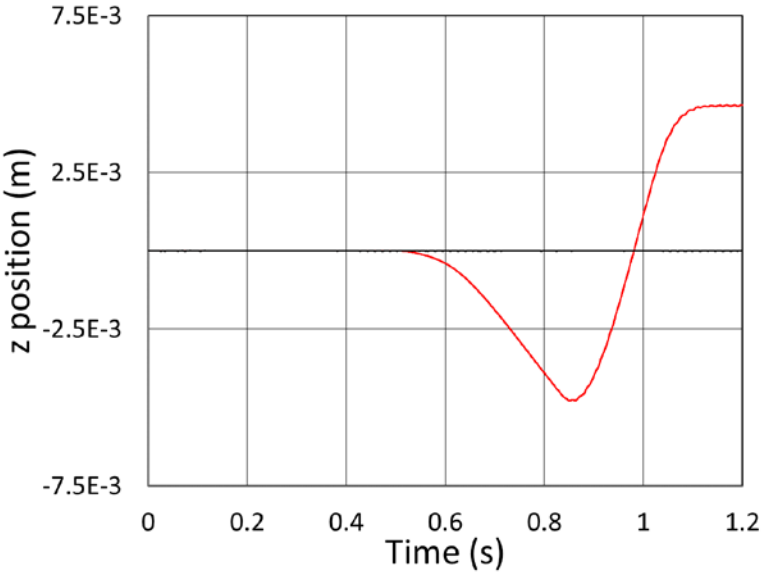

Figure 49. Comparison of the bubble position evolution in z direction with lateral control force (black line) and without lateral control force (red line) for the validation of PID bubble controller.

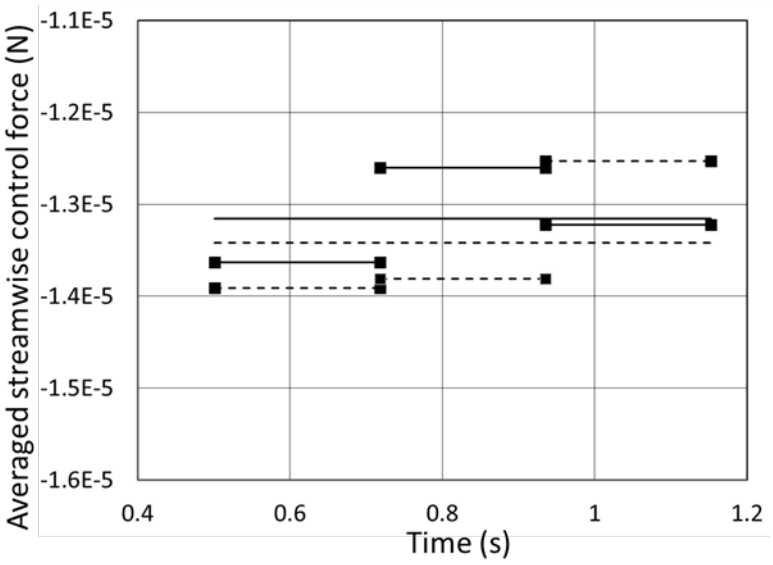

Figure 50. Comparison of the streamwise (x) direction control force with lateral control force (solid line) and without lateral control force (dash line) for the verification of PID bubble controller. The control forces are averaged over separate windows (square symbols) and over the whole time range (no symbols), respectively.

In the following sections we will present the results on the effects of turbulent intensity, bubble deformability and relative velocity on the drag force experienced by the bubble.

3.3.1 The effect of turbulent intensity

Since the homogeneous turbulent flow follows the power decay law as shown in Figure 58, we can separately put a single bubble in different streamwise positions to get various turbulence intensities at the bubble location. When implementing the instantaneous velocity history as the inflow boundary conditions, the BCT capabilities enable us to add an arbitrary shift velocity, u_{shift}, to the original instantaneous velocity, u. The adjusted instantaneous velocity, u_{bct}, is expressed as

$$u_{bct} = u - u_{shift} \quad (99)$$

Then the mean velocity, U_{bct}, is

$$U_{bct} = \overline{u - u_{shift}} = \bar{u} - u_{shift} \quad (100)$$

The calculated fluctuating velocity, u'_{bct}, is given below which is identical to the original fluctuating velocity.

$$u'_{bct} = u_{bct} - U_{bct} = \left(u - u_{shift}\right) - \left(\bar{u} - u_{shift}\right) = u - \bar{u} = u' \quad (101)$$

Using this technique, we can reduce the mean inflow velocity from 0.3 *m/s* to 0.1 *m/s* while keeping the same Reynolds stress in the two-phase simulation to achieve the desired relative velocity between the liquid and the bubble. Note that the new shifted velocity field still satisfies single-phase Navier-Stokes equations. And we use fixed bubble Weber number value of 0.68. Weber number reflects the relative importance of the fluid's inertia compared to its surface tension. It is defined as

$$We = \frac{\rho u_r^2 D}{\sigma} \quad (102)$$

where ρ is the liquid density, u_r is the relative velocity, D is the bubble diameter and σ is the surface tension. The corresponding bubble Reynolds number is 583. The turbulent intensity is defined as

$$I = \frac{u'}{U} \quad (103)$$

where u' is the root-mean-square of the turbulent velocity fluctuations and U is the mean velocity. In this case, the mean velocity is 0.1 m/s. The u' can be computed as

$$u' = \sqrt{\frac{1}{3}\left(u_x'^2 + u_y'^2 + u_z'^2\right)} = \sqrt{\frac{3}{2}k} \quad (104)$$

Figure 51 shows the separate bubble positions and the turbulent eddies surrounding the bubble, i.e., Q-criterions. Q-criterion [179] is defined as

$$Q = \frac{1}{2}[|\Omega|^2 - |S|^2] \quad (105)$$

where $\Omega = \frac{1}{2}[\nabla v - (\nabla v)^T]$ is the vorticity tensor and $S = \frac{1}{2}[\nabla v + (\nabla v)^T]$ is the rate of strain tensor. In Figure 51 we have used the contour values of ± 20.

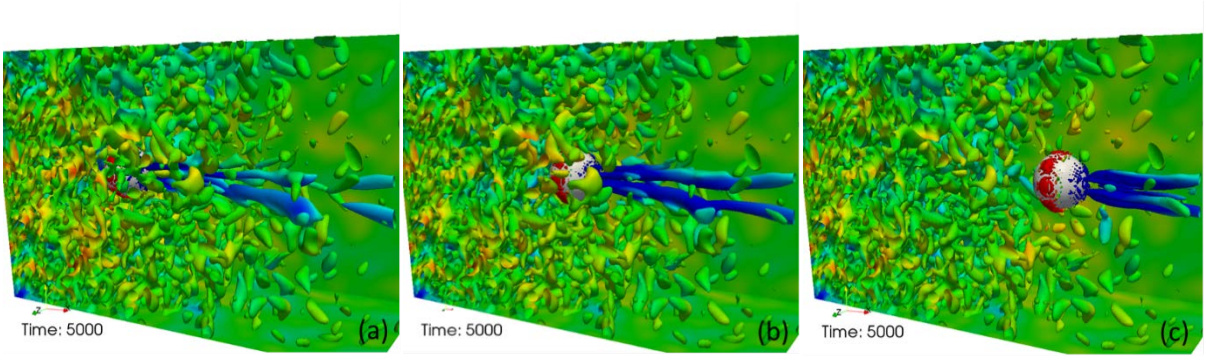

Figure 51. Different bubble positions for the turbulent intensity effect study. Bubble local turbulent intensities from left to right are, 3.44%, 2.86% and 2.34%, respectively.

In the present study, the bubble local turbulent intensities vary from 2.34% to 3.44% (Figure 51). Higher turbulent intensities would lead to stronger interactions between the bubble and liquid turbulent eddies. Higher intensities create additional challenges to steadily control the bubble using the PID approach. Figure 52 compares the control force evolution with different turbulent intensities. The control force fluctuation is defined and calculated as follows

$$\Delta CF = \frac{\sum_{i=1}^{N} |CF_i - \overline{CF}|}{N} \quad (106)$$

where CF_i is the instantaneous control force at timestep i and $\overline{CF}$ is the time-averaged control force.

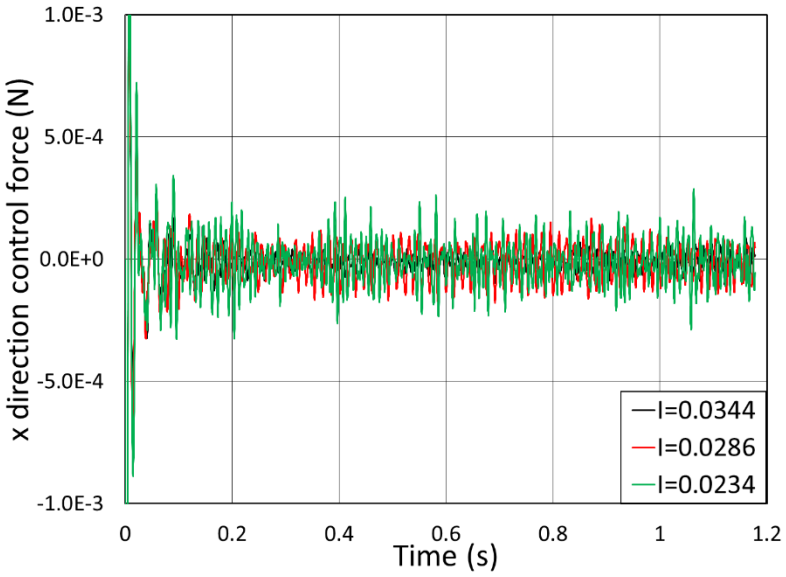

Figure 52. Evolution of streamwise direction (x) control force for the turbulent intensity effect study.

The magnitude of control force fluctuation are 2.46×10^{-5}, 5.83×10^{-5} and 7.04×10^{-5} N, and it increases with turbulent intensity. However, the averaged control forces for different turbulent intensities are quite close and the drag coefficients are 0.0965, 0.0970, and 0.0930, respectively. It supports the hypothesis that the drag coefficient does not strongly depend on the turbulent intensity at least over the range we investigate in this research. Figure 53 shows the plot of the drag coefficient versus turbulent intensity. The relative difference is within 2.6%. Based on Tomiyama's correlation [1], the drag coefficient is estimated at 0.0823 for laminar conditions.

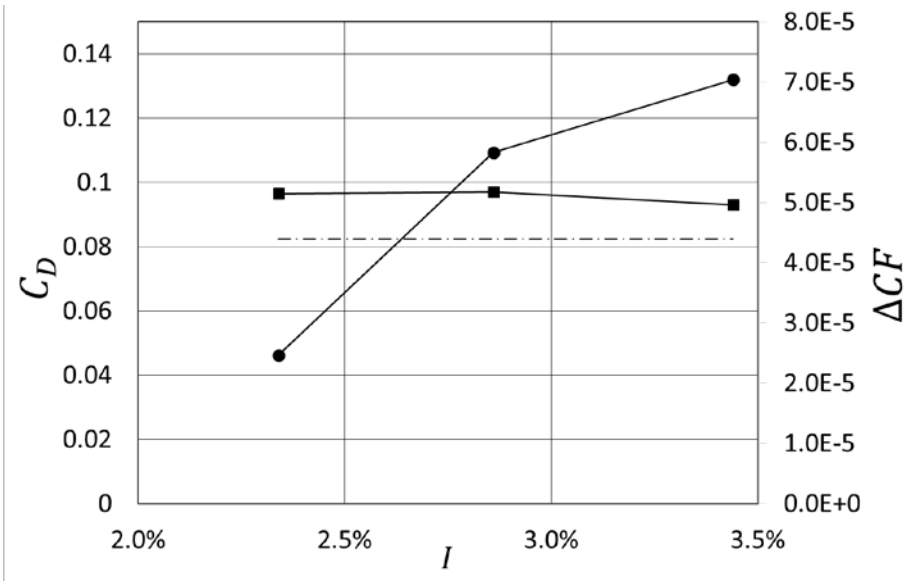

Figure 53. Comparison of the drag coefficient from PHASTA simulation (square symbols), the drag coefficient from Tomiyama's correlation (dash-dot line) and the control force fluctuation (circles) as a function of turbulent intensity.

3.3.2 The effect of bubble deformability

To study the bubble deformability effect we only modify the surface tension in our simulations while keeping the other parameters fixed. We perform simulations with five different Weber numbers (0.34, 0.68, 1.35, 2.03 and 2.71) to represent different bubble deformation levels. The corresponding bubble size in physical experiment (at Earth gravity conditions) is given in Table 12. After the flow field around bubbles reaches a quasi-steady state, the deformable bubble has a stable bubble shape as shown in Figure 54.

Table 12. Summary of the bubble deformability study.

Case #	1	2	3	4	5
We	0.34	0.68	1.35	2.03	2.71
Spherical bubble diameter (mm)	0.45	0.64	0.91	1.16	1.66
Extended bubble diameter (mm)	0.45	0.67	0.95	1.30	2.00

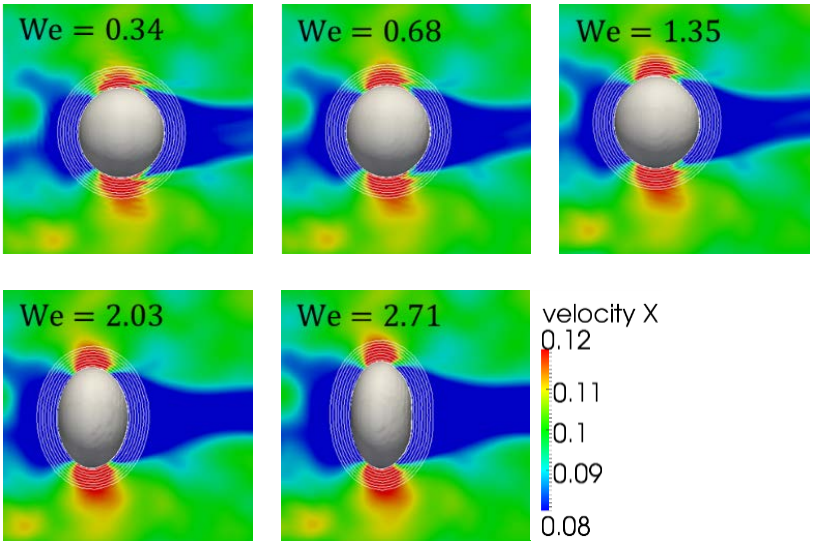

Figure 54. Velocity field around different deformable bubble with level-set contours.

Since the bubble has a wide range of deformation level, it would be a wrong to use the spherical bubble diameter to calculate the frontal area of the bubble to estimate the drag coefficient based on the drag force obtained in the simulation. Considering the bubble deformation, the frontal area is calculated based on the extended bubble diameter (D_H). Figure 55 shows the drag force and drag coefficient versus different bubble deformation level. The bubble cross-sectional area increases with the bubble deformability from $0.25\,\pi D^2$ to $0.30\,\pi D^2$. Since the drag force is proportional to the cross-sectional area shown in Eq. (23), the drag force increases with bubble deformability. However, the drag coefficient increases sharply and reaches the maximum for the most deformable bubble. It may be due to the effect

of bubble-induced turbulence which causes the violent convective and temporal acceleration between the liquid and gas. Legendre and Magnaudet [92] pointed out that the presence of liquid velocity gradient increases the drag force acting on the bubble. Since the liquid velocity gradient around the deformable bubble is higher compared to a spherical bubble, the observed increase in drag force is consistent with the experiment.

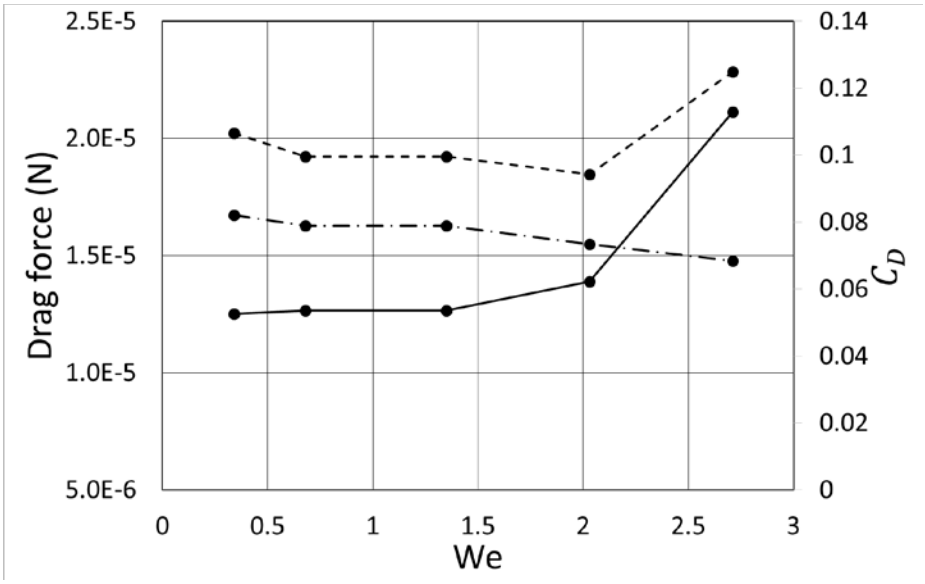

Figure 55. Comparison of the drag force (solid line), the drag coefficient for homogeneous turbulent flow condition (dash line) and the drag coefficient for laminar flow condition (dash-dot line) versus different bubble deformation levels.

3.3.3 The effect of relative velocity

In addition to the bubble deformability and local turbulent intensity studies, the relative velocity effect is also investigated in our research. Four values of relative velocities, 0.08 m/s, 0.10 m/s, 0.12 m/s and 0.15 m/s, are chosen. The bubble in each case is placed at the position where the turbulent intensity is expected to be the same in each case. We also keep the same bubble deformation level ($We = 0.68, D = 0.64\ mm$), by changing the surface tension. The

summary of the case setups is given in Table 13. Figure 56 confirms that the bubble shape is very close when we maintain the same Weber number. It validates the appropriateness of using Weber number on the analysis of droplets and bubbles' formation.

Table 13. Summary of the relative velocity study.

Case #	1	2	3	4
We	0.68	0.68	0.68	0.68
Relative velocity (m/s)	0.08	0.10	0.12	0.15
Surface tension (N/m)	0.0471	0.0735	0.1059	0.1654

Figure 57 provides the comparison of the drag coefficient as a function of bubble Reynolds number. It shows that the drag coefficients calculated from PHASTA simulation are quite close to the experiment-based correlation under the turbulent flow condition. However, the difference increases with higher bubble Reynolds number. A modified closure model is proposed to predict the drag coefficient at this Reynolds number range. As shown in the Figure 57, the proposed model fits well with the drag coefficient data point from both laminar and turbulent flow conditions. It is supposed to be valid below the Re_b of 900.

$$C_D = \min\left[\frac{16}{Re_b}(1 + 0.15Re_b^{0.687}), \frac{48}{Re_b}(1 + 3 \times 10^{-10}Re_b^{3.3189})\right] \quad (107)$$

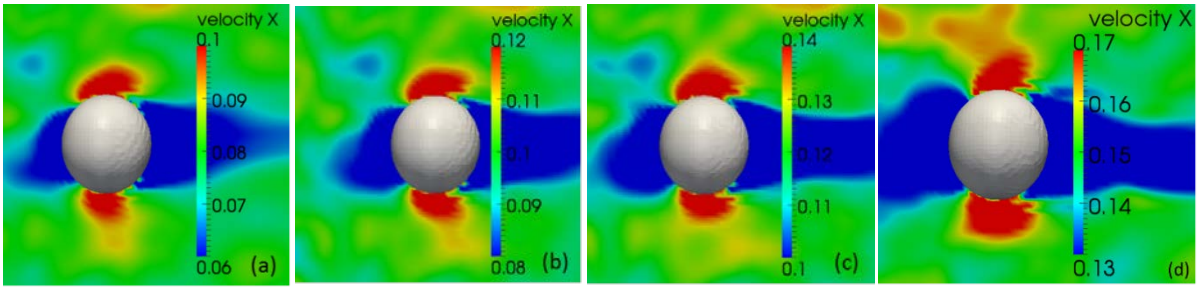

Figure 56. Comparison of bubble shape for different relative velocities.

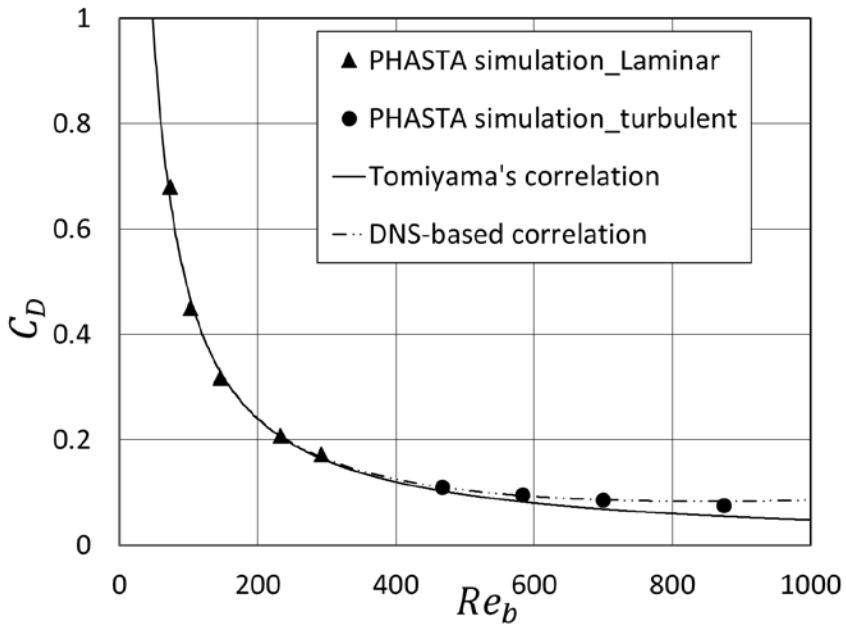

Figure 57. Drag coefficient comparison between Tomiyama's correlation and DNS-based correlation. Data point from laminar flow simulation has been reported in [56].

CHAPTER 4. BUBBLE-INDUCED TURBULENCE

4.1 Evaluation of BIT in homogeneous turbulent flow

The single phase homogeneous turbulent flow is generated by applying constant pressure gradient force to drive the flow past the obstacles. Two grid planes with 6×10 spheres array are placed at $x = 2$ mm and $x = 3$ mm positions to leave enough distance to develop the homogeneous turbulence (see section 2.3).

We use set of virtual probes arranged in 2D planes normal to the flow direction to extract the instantaneous velocity histories. The position of the probe plane is carefully chosen to make sure that both the velocity profile and the turbulent kinetic energy are homogeneous and are not directly affected by the shape and spanwise distribution of the turbulence generating grid. The probe plane is positioned normal to the streamwise direction, i.e., x direction, contains 125 (nodes in y direction) $\times 75$ (nodes in z direction) probes which are used to extract the instantaneous velocity information at those points over time and allows us to determine the level of turbulent kinetic energy.

We have performed the mesh study (section 2.3) to demonstrate that the choice of mesh resolution is appropriate to resolve all the turbulent scales in the region of interest. As shown in the Figure 58, after averaging the data in z direction, the velocity and turbulent kinetic energy are plotted for different mesh configurations. Uniform distribution of velocity and TKE are observed. The results from the two meshes are consistent, which indicates the appropriateness of the coarser mesh for further simulations. The averaged velocity is 0.297 m/s and the

averaged turbulent kinetic energy is 6.74×10^{-5} m^2/s^2. Compared to the coarser mesh case, the finer mesh has almost identical averaged results.

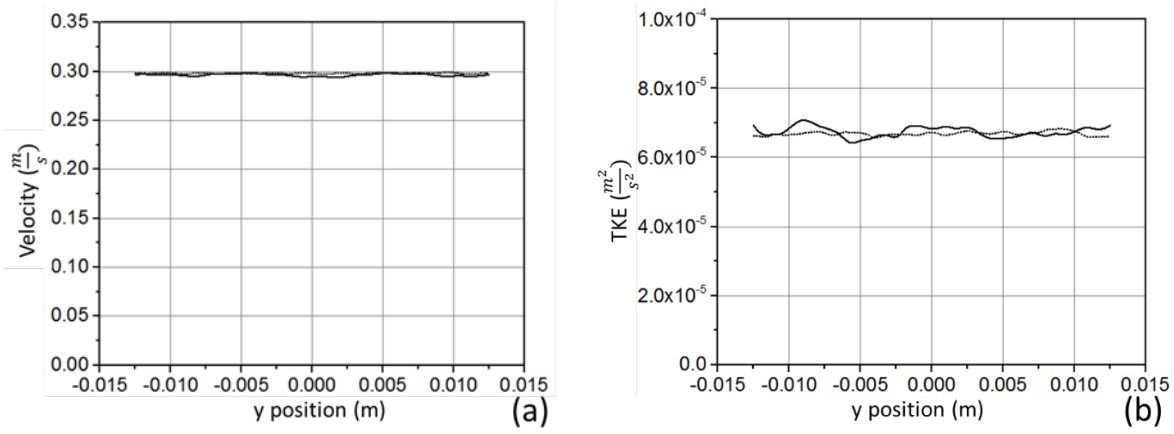

Figure 58. Velocity and turbulent kinetic energy profiles for different mesh refinement. Solid and dotted lines represent 28 million and 129 million mesh cases, respectively.

The decay of homogeneous turbulent flow in our case is consistent with previous observations which demonstrate the validity of our approach. Figure 59 shows that the decay of turbulence agrees well with the power law. The decay exponent is found to be 1.5, which is close to the experiment-based range [58-60].

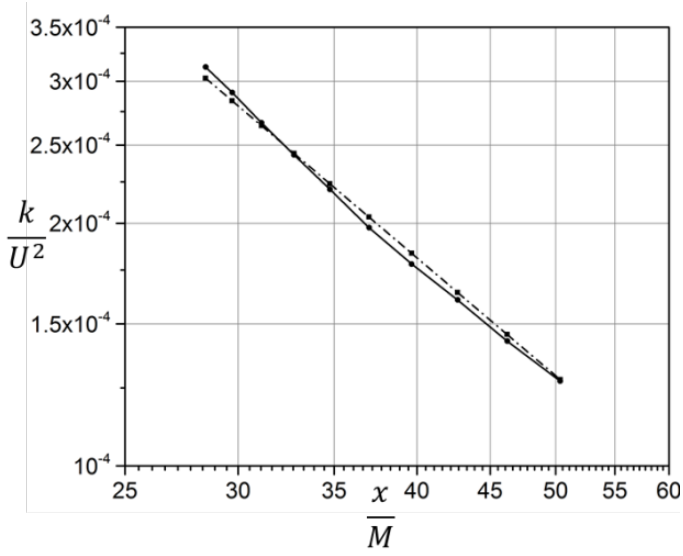

Figure 59. Decay of turbulent kinetic energy as a function of $\frac{x}{M}$. Solid and dash lines represent raw data and power approximation line, respectively.

4.1.1 Validation of level-set approach for BIT problem

The level-set interface tracking method [49, 168] can numerically distinguish the interface between the gas and liquid phases and allows us to capture the bubble motion and shape deformation. The deformable bubble in the two-phase flow simulation can be fully resolved with level-set ITM by putting enough computational points across the bubble diameter to represent the interface curvature. As with any ITM which uses single-fluid approach, the Navier-Stokes solver deals with one fluid which has its properties changed across the interface. The level-set method utilizes a smooth transition (Eqs. (55), (56), and (57)) of the fluid properties from liquid to gas across the interface with typical thickness of 2.5 computational cells. However, the existence of this transitional region may influence the development of turbulent boundary layer and affect the bubble-induced turbulence. We have previously verified that the drag force estimates are not affected by the property transition

region. In this paper we perform an additional study to quantify the effect of this region on the turbulence generated by a single bubble.

The separate study problem is performed using single-phase simulations with a solid sphere (representing a typical bubble) in the domain and introducing various artificial interface thicknesses on the sphere surface. While the level set method is not utilized directly in those simulations, we mimic the property smoothing region by varying the liquid properties near the sphere surface as shown in Figure 61. The subroutines are provided in Appendix F. As the liquid passes around the sphere, the existence of the artificial interface on the development of turbulent boundary layer is investigated. The sphere diameter is 5 mm and the simulation domain size is $25 \times 25 \times 15$ mm^3. We place 20 elements across sphere diameter and boundary layers on the sphere surface to help capture the development of turbulent boundary layer. Additional refinement region is placed in the wake of the sphere to capture the wake induced turbulence. The case setup parameters are given in Table 14 and the simulation domain is shown in Figure 60. The distance to the probe plane is measured in the sphere diameters (D).

Table 14. Geometrical and mesh configuration of the level-set validation cases.

Domain size (mm^3)	25×25×15	
Bulk mesh size (mm)	0.5	
Mesh setup of sphere boundary layer	Mesh resolution on the surface (mm)	0.2
	First layer thickness (mm)	1×10^{-2}
	Boundary layer total thickness (mm)	1.55
Mesh size in the wake region (mm)	0.2	
Distance from the probe plane to the sphere center	Probe plane 1	1*D*
	Probe plane 2	1.5*D*

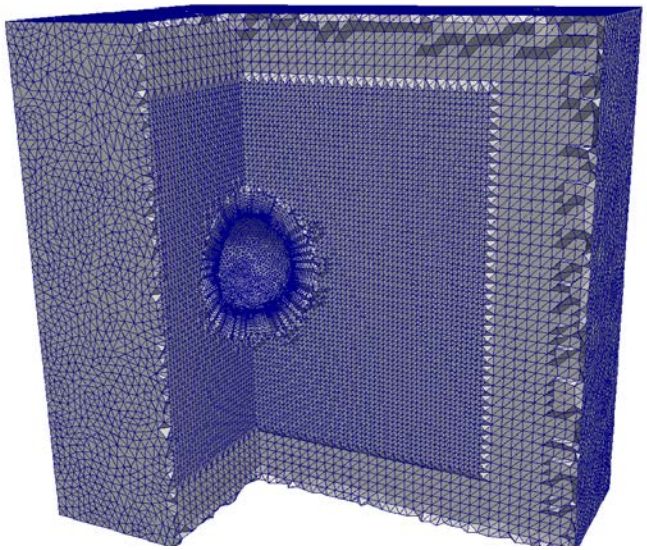

Figure 60. Simulation domain for level-set verification cases.

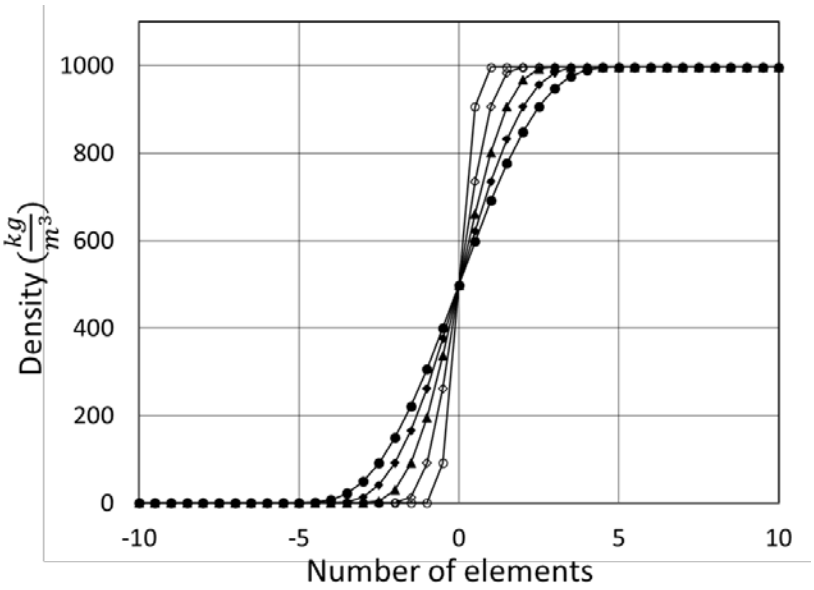

Figure 61. Density evolution across the interface. The width of the transition region are 1 (hollow sphere), 2 (hollow square), 3 (triangle), 4 (square) and 5 (sphere) elements.

Homogeneous turbulent flow with mean velocity of 0.05 $\frac{m}{s}$ is utilized as the inflow boundary condition to perform the study. The corresponding Reynolds number based on sphere diameter is 292 which is typical for a bubble Reynolds number in bubble-induced turbulence studies [24, 166, 180]. Two probe planes are placed in the wake region to record the instantaneous 3D velocity information. The distance between the probe planes and the sphere center are 1 and 1.5 sphere diameter, D, which are described in Table 14. Figure 62 compares the averaged TKE profile versus several artificial interface thicknesses. For the wake region which contains the sphere projected area on the probe plane, except the thickest interface thickness which is the half sphere diameter, the TKE results agree well with the case having no properties transition region. For the region away from the sphere, the TKE profile agrees perfectly. Figure 63 compares the velocity profile versus various interface thicknesses. As the

interface thickness increases, the depth of the velocity valley behind the sphere decreases which is caused by the existence of transition region.

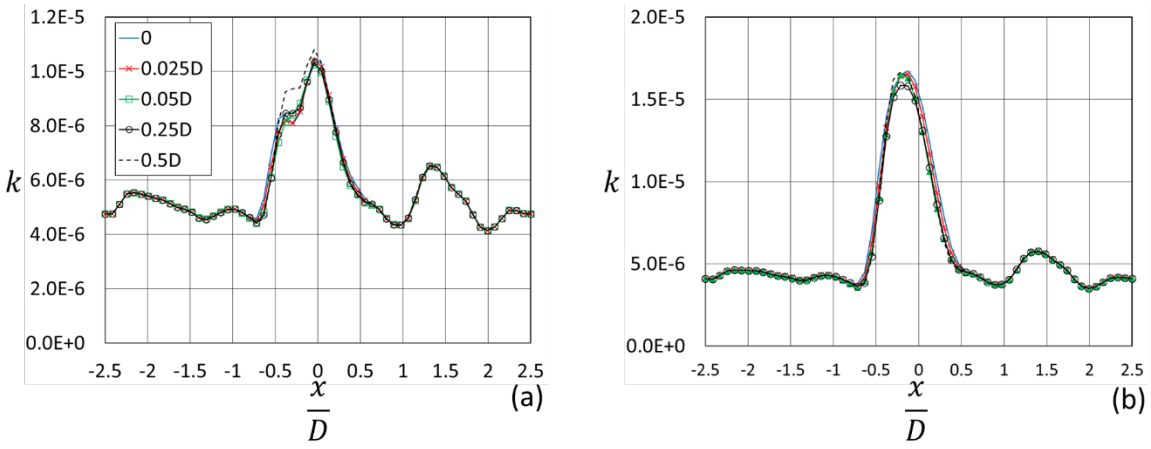

Figure 62. TKE profile from probe plane 1 versus different artificial interface thicknesses, 0 (no interface), 0.025 *D*, 0.05 *D*, 0.25 *D* and 0.5 *D* where *D* is the sphere diameter. Left (a) and right (b) represent the plot at probe plane 1 and 2 (described in Table 14), respectively.

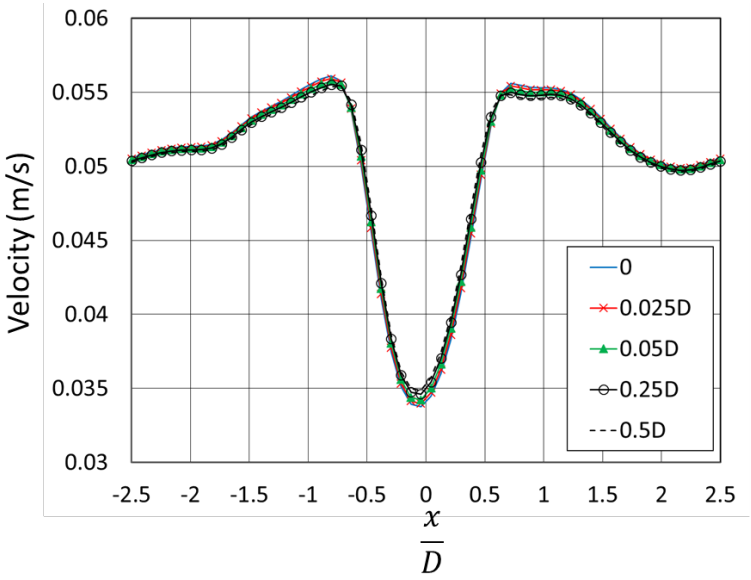

Figure 63. Velocity profile versus different artificial interface thicknesses for probe plane 1.

The relative error for the TKE versus interface thickness is calculated as follows

$$Error = \frac{\sum_{i=1}^{N}\left(TKE_i^{(0)} - TKE_i^{(n)}\right)}{\sum_{i=1}^{N} TKE_i^{(0)}} \quad (108)$$

where $TKE_i^{(n)}$ is the averaged TKE at spanwise position i and the interface thickness is n. $TKE_i^{(0)}$ is the TKE data point for the case without interface thickness. Using the Eq. (108), we plot the relative error versus interface thickness. The relative error for the first probe plane is within 3% and the second probe plane is within 5%. One drawback of the single-fluid approach is the introduction of the transition region. This results in the smearing of the flow properties and variables, forcing them to be continuous at the interface regardless of the appropriate jump condition. Our studies reveal that the influence of level-set method on the turbulent boundary layer development is minimal. As the width of the transition region decreases, the results are expected to approach the ideal situation.

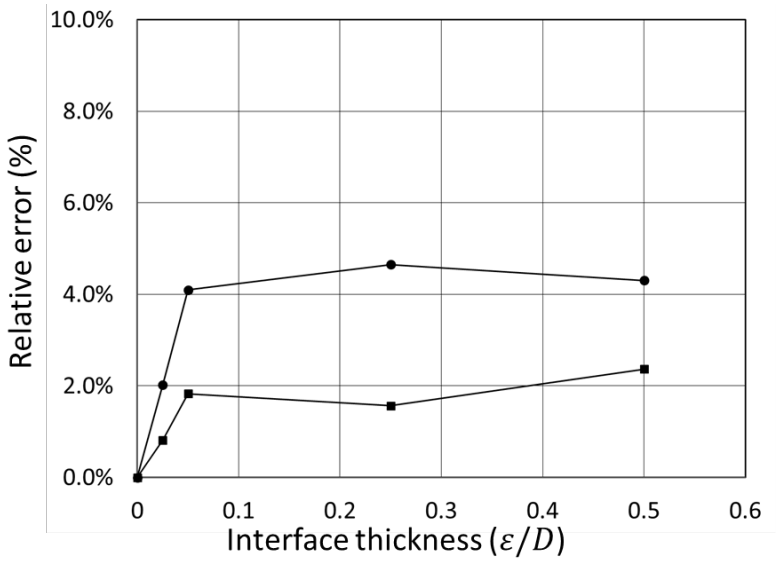

Figure 64. Relative error versus artificial interface thickness for two locations in the wake of the sphere. The distance between the probe plane and sphere center are 1D (sphere) and 1.5D (circle). “D” represents the bubble diameter.

The studies described above introduce artificial interface thicknesses on the solid sphere surface, which is important for the understanding of the influence of properties

transition region on the bubble-induced turbulence. However, the transition region inside the bubble is not considered for the solid sphere case. A supplemental test is performed for a two-phase case with varying interface thickness, ε/D =0.96, 0.16, and 0.24 (the pressure field is shown in Figure 65). The turbulent intensity versus different interface thicknesses is given in Figure 66. The comparison shows that influence of interface thicknesses on the bubble-induced turbulence is minimal. The turbulent intensity, bubble deformation and relative velocity will play a more important role on the interaction between the turbulent eddies and the bubble.

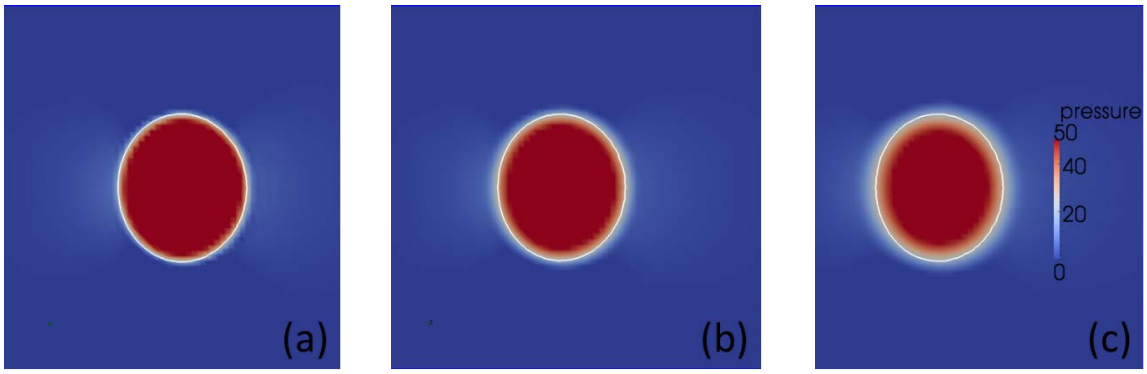

Figure 65. Comparison of pressure field for different interface thicknesses, $\frac{\varepsilon}{D}$ =0.96, 0.16, and 0.24.

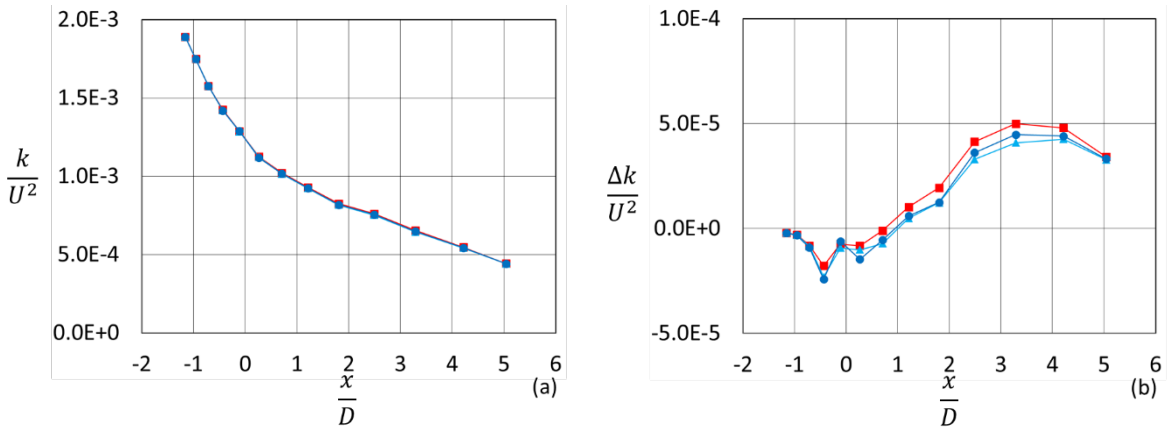

Figure 66. Turbulent intensity versus position for different interface thicknesses cases, $\frac{\varepsilon}{D}$ =0.96 (square), 0.16 (triangle), and 0.24 (sphere), where x/D=0 represents the streamwise position of the bubble center.

4.1.2 The effect of turbulent intensity

As we know, the homogeneous turbulent flow follows the power decay law. We can separately put single bubble in different stream-wise positions (x/D), 2.00, 3.14 and 4.93, to get different turbulence intensities at the bubble location while keeping the relative velocity fixed at 0.1 m/s and using fixed bubble Weber number value of 0.68. Figure 67 shows the turbulent intensity plot with different local bubble turbulent intensities. The bubble positions are shifted to the origin to directly reflect the influence of turbulence intensity on BIT. The liquid flow turbulence is reduced locally at the bubble location. As mentioned before, the gas-liquid interface would absorb the liquid turbulence by deforming their shape which brings about an increase of the surface energy and also an increase of energy dissipation in the vicinity of the interfaces through turbulence eddy/interface interactions. In the meantime, the turbulent

kinetic energy in the liquid phase is increased by the wake induced by the bubble. The larger bubble local turbulent intensity, like 3.44% and 2.86%, would experience a deeper energy sink and introduce larger turbulence enhancement behind the bubble.

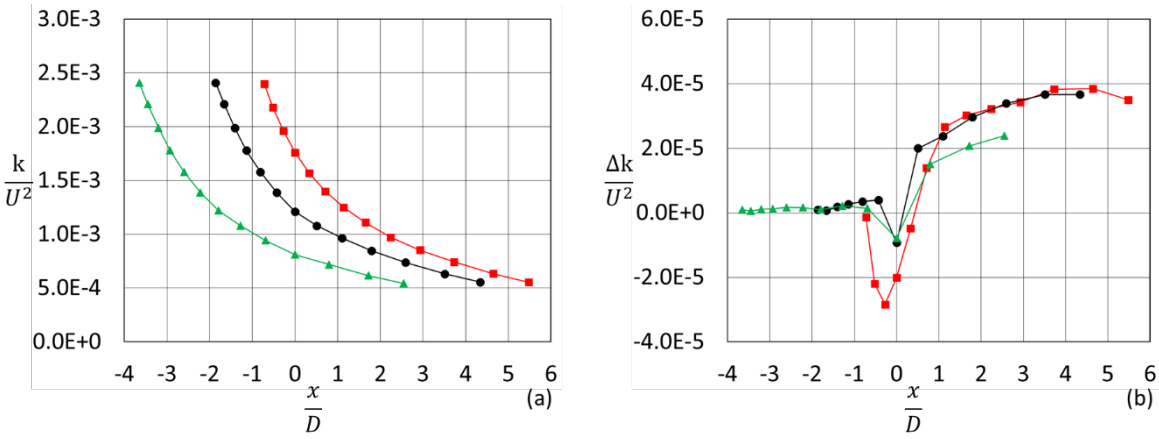

Figure 67. Turbulent intensity versus position for different bubble local turbulent intensity cases, 3.44% (square), 2.86% (circle) and 2.34% (triangle). The center of the bubble corresponds to the $\frac{x}{D} = 0$.

The turbulence isotropy level with and without bubble are investigated as well. The turbulent kinetic energy k is defined and calculated as

$$k = \frac{1}{2}(u'u' + v'v' + w'w') \qquad (109)$$

where u', v' and w' are the turbulent velocity fluctuations in x, y and z direction.

Figure 68 shows comparison of Reynolds stress components to evaluate the turbulence isotropy evolution. Figure 68 (a) shows the decay of $u'u'$, $v'v'$ and $w'w'$ components in the stream-wise direction. Through the block-induced turbulence generation method, we are able to generate homogeneous turbulent flow while the three Reynolds stress components are not identical. Although the turbulent flow is homogeneous, it is not isotropic. The $u'u'$ is 1.35 and 1.88 times as large as $v'v'$ and $w'w'$, respectively, at the first data point. Comte-Bellot and

Corrison's experiment [58] shows that the u'^2 is 10% greater than the v'^2 and w'^2 and the symmetry in the ideal experiment dictated that v'^2 and w'^2 are equal. As flow passes through the domain, the $v'v'$ and $w'w'$ components tend to become more identical. The trend of u'^2, v'^2 and w'^2 development in our study are reasonable and the ratio of u'^2 to v'^2 or w'^2 depends on the setup. The proportion of $u'u'$ to the total kinetic energy steadily increases. Figure 68 (b), (c) and (d) show the turbulent kinetic energy difference between the two-phase case and single-phase case for different turbulence intensity scenarios. The streamwise direction Reynolds stress component $u'u'$ contributes to the energy drop when the turbulent eddies interact with the bubble and fluctuations in y and z direction are slightly influenced at the bubble position. Then, the $v'v'$ and $w'w'$ components reach a peak in the front part of the wake region which is around 1 bubble diameter away from the bubble. The peaks in the wake region may come from the redistribution of $u'u'$ other than being transferred to the bubble. After that $v'v'$ and $w'w'$ components gradually drop and the streamwise fluctuation $u'u'$ starts to play a dominant role in the bubble-induced turbulence in the tail of wake region which is more than 1.5 bubble diameters long. Clearly, the analysis of velocity fluctuation components provides insight on the mechanism of the interaction between the bubble and liquid turbulent flow, which has the potential for the application of turbulent bubbly flow. Future work can include the interaction between a single bubble and higher intensity turbulence. The oscillation of bubble shape may occur and energy absorption by the bubble may be observed.

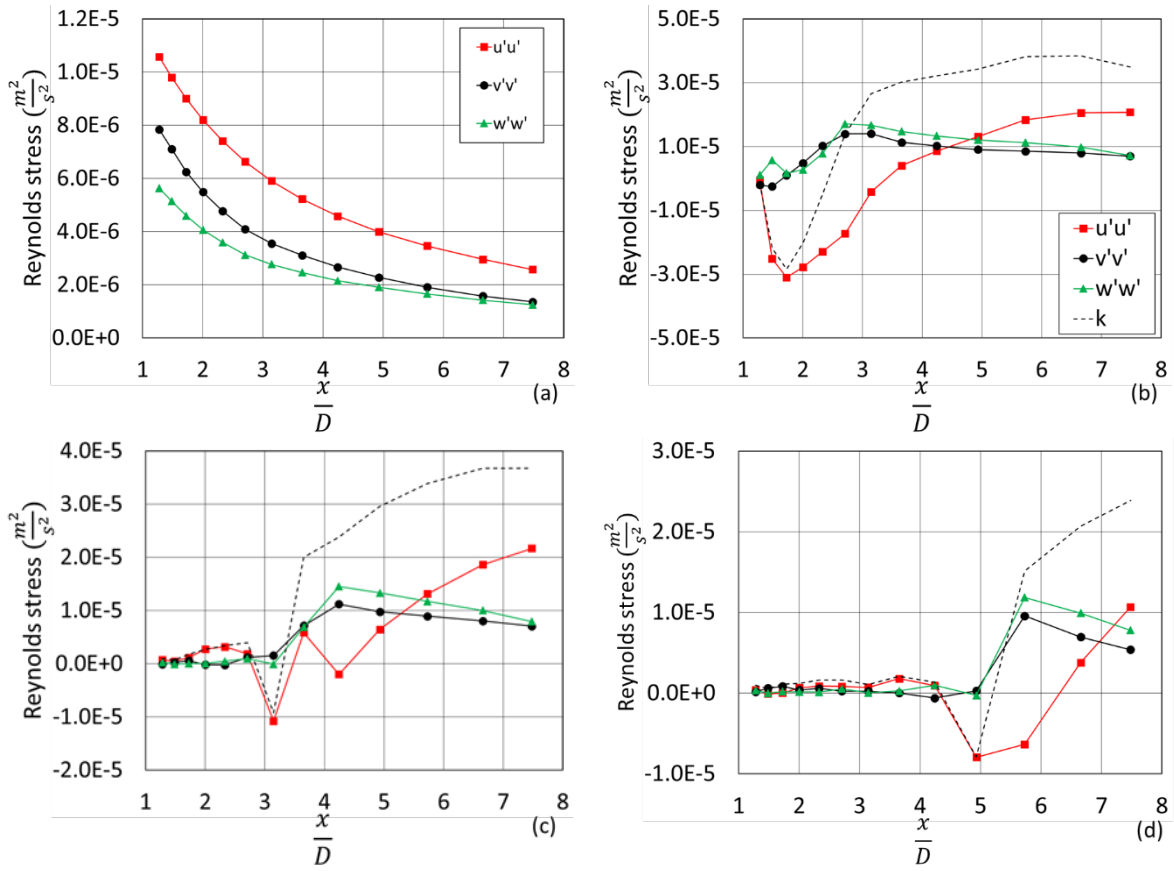

Figure 68. Turbulent isotropy comparison for different turbulent intensities. Bubble positions are 2.00, 3.14 and 4.93 for different turbulent intensities cases.

4.1.3 The effect of bubble deformability

After obtaining the instantaneous velocity history from the single-phase homogeneous turbulent flow, the PHASTA code has an important capability that enables us to implement the instantaneous transient velocity field as the inflow boundary condition for the two-phase flow simulation. For the two-phase flow simulation, a single bubble with diameter *D* of 5 mm is placed in the center of the domain with non-dimensional size (*7.5D, 5D, 3D*) as shown in Figure 46. The detailed description of the case setup is given in section 3.3.2.

We have reduced the mean inflow velocity from 0.3 m/s to 0.1 m/s while keeping the same Reynolds stress in the two-phase simulation to achieve the desired relative velocity between the liquid and the bubble. The corresponding bubble Reynolds number for the two-phase flow case is 583. After the flow field around bubbles reaches a quasi-steady state, i.e., the deformable bubble has a stable bubble shape as shown in Figure 54, we put 13 virtual probe planes normal to the stream-wise direction with 60×36 probes on each plane to extract the instantaneous velocity information before, across and behind the bubble.

The averaging time window is 0.70 s and during this time period the flow passes through the whole domain 1.87 times. Both the liquid turbulent intensity and the turbulence intensity difference compared to single phase simulation versus dimensionless bubble position (x/D) are plotted in Figure 69.

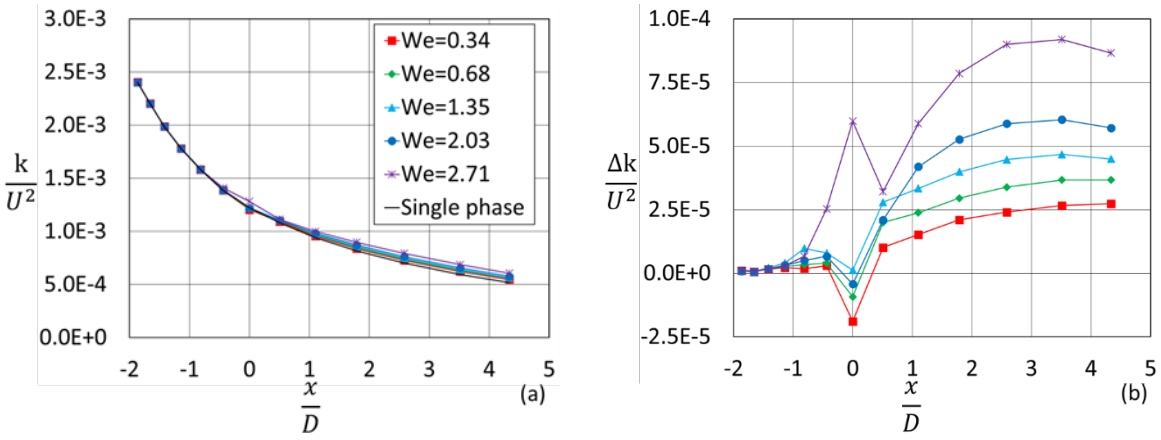

Figure 69. Turbulent intensity versus non-dimensional position with different bubble deformation levels. The center of the bubble corresponds to the $x/D = 0$.

When the turbulent flow reaches the bubble, the liquid transfers some portion of the turbulent kinetic energy through the bubble surface into the gas inside the bubble. The bubble acts as an energy absorber and the energy is dissipated by the recirculation of the gas within

the bubble. However, the existence of the bubble creates additional turbulent eddies behind it, and we expect to observe turbulence enhancement in the wake region. As bubble becomes more deformable, more turbulent kinetic energy is generated as the bubble generates more vorticity compared to spherical bubble and the deformable bubble has relatively larger cross-sectional area which leads to the increased drag force. The vorticity of the liquid surrounding the bubbles increases considerably.

The bubble-induced turbulence is analyzed by comparing the difference of liquid turbulent kinetic energy with and without a bubble. Figure 69(a) shows the overall TKE for different deformable bubble cases compared to the single-phase case and Figure 69(b) shows the TKE difference between the different deformable bubble two-phase cases and the single-phase case. Generally, the liquid turbulent kinetic energy experiences a drop when the liquid turbulent eddies approach the bubble. However, for the most deformable bubble, i.e. $\mathrm{We} = 2.71$, the TKE peak occurs at the bubble location which indicates the additional generation counteracts the dissipation of turbulence energy. And in the tail of wake region, we observe that the bubble induced turbulence increases as the bubble becomes more deformable.

To analyze the effect of highly deformable bubble on the bubble-induced turbulence, an additional test with $We = 3.39$ is performed. For the highly deformable bubble, the simulation results show that the bubble behavior under homogeneous turbulent flow has two modes, stable and variable shape modes. Here we define the bubble diameter time as the number of times one Lagrangian particle passes through the distance equivalent to one bubble diameter. During the simulation time, up to 0.75 s (this corresponds to 15 bubble diameter times), the bubble shape is observed to be steady as shown in Figure 70. After that, the bubble

shape starts to oscillate over time which produces additional turbulent eddies in the wake. Figure 71 compares the streamline pattern around the spherical bubble ($We = 0.34$) and highly deformable bubble ($We = 3.39$). The spherical bubble maintains a constant bubble shape and the streamline pattern around the bubble is stable. However, the highly deformable bubble exhibits an unsteady mode which significantly contributes to the turbulent kinetic energy addition as shown in Figure 73. Further investigation reveals that the unsteady mode for the highly deformable bubble follows a certain time period shown in Figure 72. The large turbulent eddies, shown by Q-criterion, are periodically generated on the bubble surface and the time interval is about 0.16 s (about 3.2 bubble diameter times) and it is identical to the period of bubble shape oscillation mode. The significant liquid turbulence addition is certainly correlated to the time varying high surface curvature of highly deformable bubble. The oscillation of bubble shapes under the influence of liquid-phase turbulence is therefore an important aspect in the understanding of the motion of bubbles in turbulent fields.

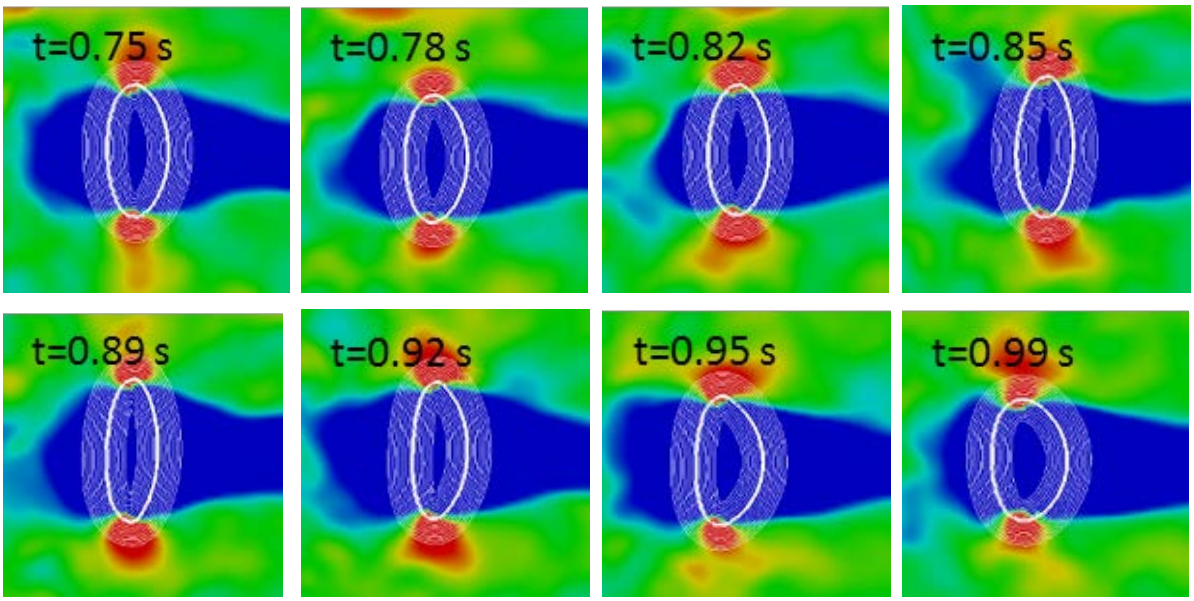

Figure 70. Bubble shape evolution over time. Bubble shape remains stable until time t = 0.82 s and becomes unstable after that.

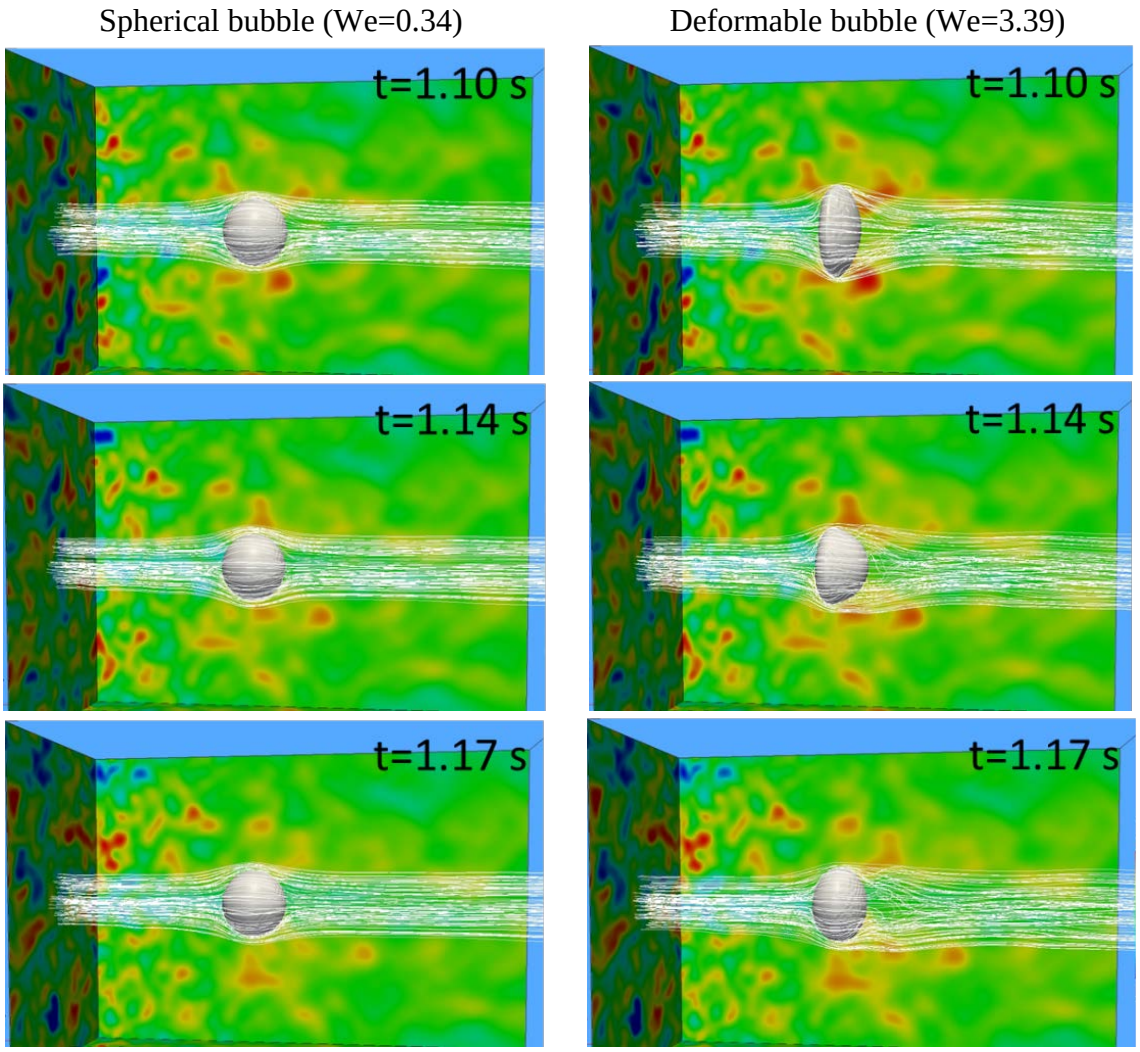

Figure 71. Comparison of streamline pattern around spherical and deformable bubble.

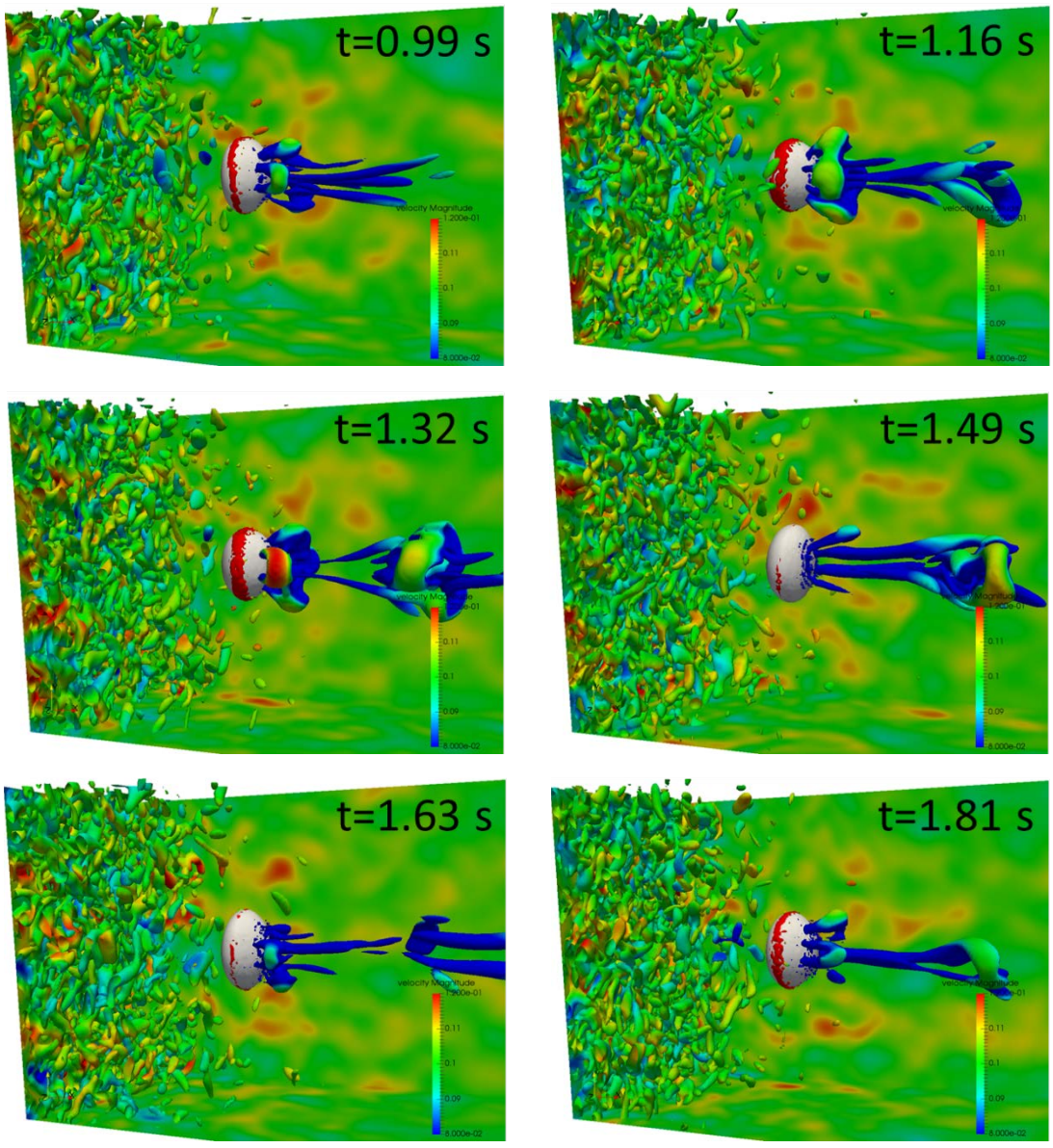

Figure 72. Turbulent eddies generation on the highly deformable bubble surface. The contour is plotted using Q-criterion with value of 100.

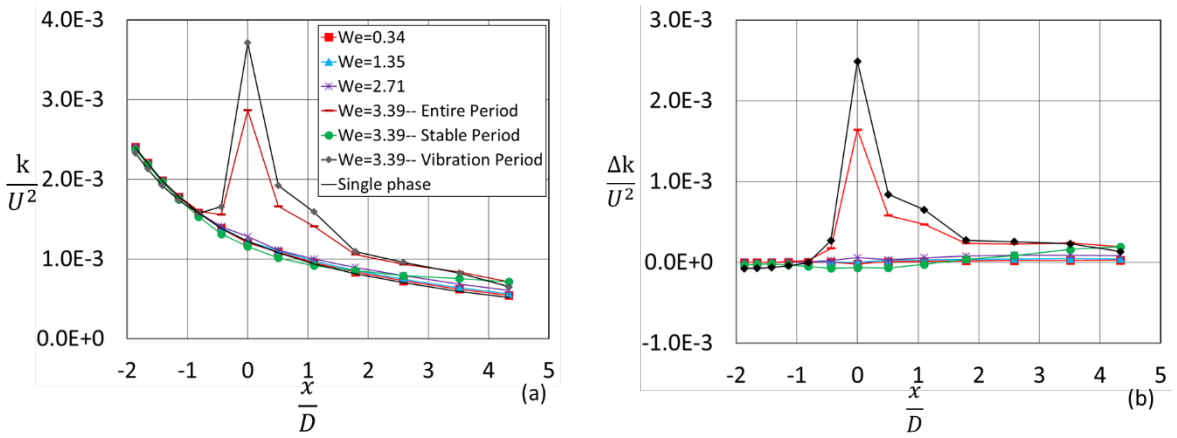

Figure 73. Comparison of turbulent intensity versus position with different bubble deformation levels. For the highly deformable bubble, We=3.39, the stable period, shape oscillation period and the entire period containing both stable and vibration periods are plotted respectively.

4.1.4 The effect of relative velocity

Apart from the bubble deformability and local turbulent intensity, the relative velocity also plays an important role on the energy transfer between gas and liquid. Three values of relative velocities, $0.08\,m/s$, $0.10\,m/s$ and $0.12\,m/s$, are chosen. Numerical simulation enables us to discuss the influence of single variable on the bubble induced turbulence which is difficult in real experiment. The bubbles are separately placed at the positions where the turbulent intensities are expected to be the same.

The bubble positions are shifted to the origin, $x/D = 0$, to directly reflect the influence of relative velocity on the liquid turbulence. 8 probe planes, x/D =-1.5, -1, -0.5, 0, 0.5, 1, 2 and 3, are selected and placed in the domain to extract the instantaneous velocity information before, across and behind the bubble. Figure 74(a) shows the total turbulent kinetic energy considering different relative velocities and the existence of bubble. Figure 74(b) shows the turbulent kinetic energy difference between single phase and two-phase flow. As the liquid

turbulent flow encounters the bubble, part of the energy from liquid is transferred to the gas and surface tension energy by deforming bubble's shape and the existence of stationary bubble also causes the energy dissipation in the vicinity of the interface through turbulence eddies/interface interactions. The magnitude of the energy drop at the bubble location increases as the relative velocity increases. In the meantime, the turbulence energy in the liquid phase is increased by the wake induced by the bubble. It also increases with relative velocity. Since the identical turbulent eddies travel with different velocities to interact with the single bubble, higher relative velocities will lead to different turbulence eddy/interface interactions within the same given time. As shown in Figure 74(b), the ratio of the energy drop peak at the bubble position for different relative velocity cases to the case with relative velocity of 0.10 $\frac{m}{s}$ are 0.83, 1.00 and 1.29. As described in Sato's model [72], the bubble-induced turbulence viscosity term is proportional to the relative velocity which results in the higher dissipation rate around the bubble for higher relative velocity.

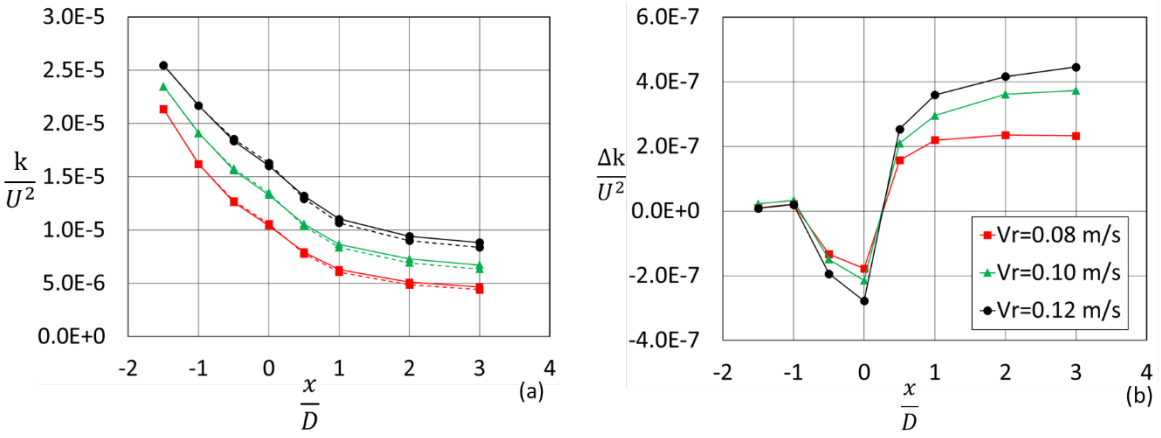

Figure 74. Turbulent intensity versus position with different relative velocity. Solid and dash lines represent the two-phase and single-phase cases, respectively.

CHAPTER 5. SHEAR TURBULENT FLOW

In this chapter, we summarize the results of the numerically generated shear turbulence ranging from ~10 to ~10^3 s^{-1}. In low shear turbulent flow, the central line shear rate, $(du/dy)_{center}$, is from 13.3 to 24.4 s^{-1} which is achievable in laminar shear flow field. In high shear turbulent flow, we emphasis on the generation of near wall shear field, $(du/dy)_{wall}$~10^3 s^{-1}, which is close to the reactor condition. Convergent solutions are obtained which can be utilized for the future work of bubble-induced turbulence in shear turbulent flow.

5.1 Low shear turbulent flow

A set of low shear turbulent flow cases with initial shear rate of 30, 45, and 60 s^{-1} are created. As mentioned in section 2.4, the shear turbulent flow can be self-sustained due to the wall shear. In this part, we apply constant shear velocity field, $\omega \times y + u_r$, on the top and bottom surfaces in wall-normal direction, periodic boundary conditions in streamwise and spanwise directions as shown in Figure 75. An array of obstacle spheres are temporally introduced to create unsteady velocity field and accelerate the turbulence generation process. Figure 76 shows the evolution of velocity field.

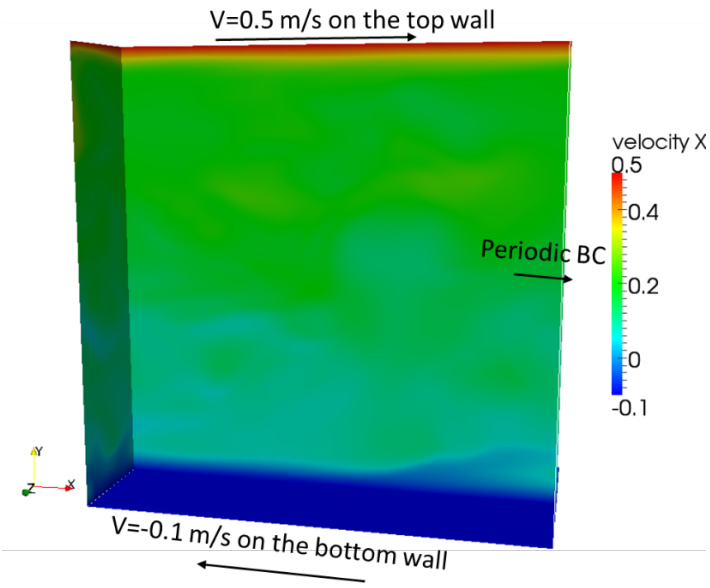

Figure 75. Illustration of the boundary conditions for the generation of shear turbulent flow.

The domain size is $0.02 \times 0.02 \times 0.01$ m^3 and the number of elements is 0.52 million for all the three cases. After the removal of obstacle spheres, the instantaneous velocity information is recorded after around 50 flow-throughs. The collected velocity information covers an averaging window of 2 s corresponding to 20 flow-throughs. Table 15 summarizes the results of the low shear single phase turbulent flow cases. The turbulent intensity ranges from 9.7% to 20.1% and the center line shear rate ranges from 13.3 to 24.4 s^{-1}. By implementing the turbulent velocity field as inflow boundary conditions, we can directly compare the bubble-induced turbulence between shear turbulent flow and laminar flow with same shear rate. Figure 77 compares the overall turbulent kinetic energy and velocity profile for different shear rates. It is observed that the magnitude of the TKE peak near the wall will decrease with the shear rate, i.e., Re_τ. Figure 78 compares the turbulence isotropy for selected

initial shear rate of 45 and 60 s^{-1}. The streamwise TKE component, $u'u'$, contributes to the majority of the TKE and is responsible to the turbulent generation near the wall.

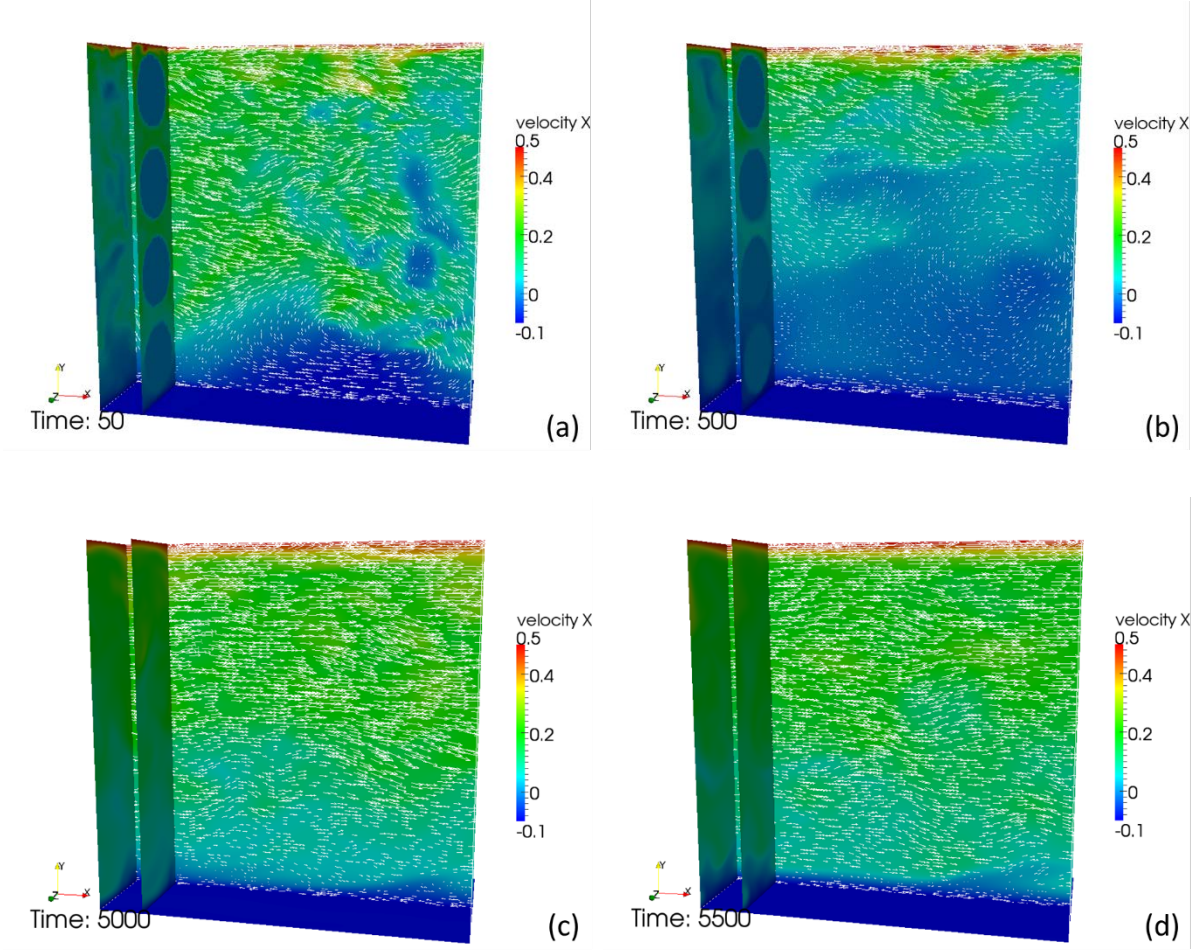

Figure 76. Evolution of velocity field for shear turbulent flow cases with initial shear rate of 30 s^{-1}. (a) and (b) shows the velocity field when a 2×4 array of obstacle spheres are present.

Table 15. Summary of the low shear single phase turbulent flow cases.

Initial shear rate (s^{-1})	Central-line relative velocity (m/s)	Re_τ	y^+ (first layer on the wall)	$\left(\frac{du}{dy}\right)_{wall}$	$\left(\frac{du}{dy}\right)_{center}$	Turbulent intensity I (%)
30	0.2	334.0	1.28	239.1	13.3	9.7
45	0.2	456.8	1.76	447.3	16.3	14.8
60	0.2	547.9	2.11	643.4	24.4	20.1

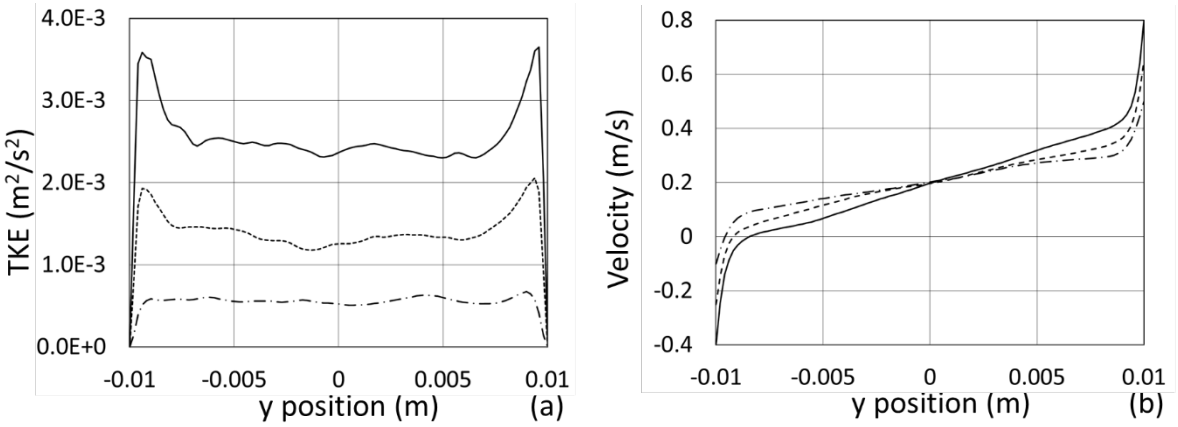

Figure 77. Comparison of TKE and velocity profiles for different initial shear rates, 30 (dash-dot line), 45 (dash line), and 60 (solid line).

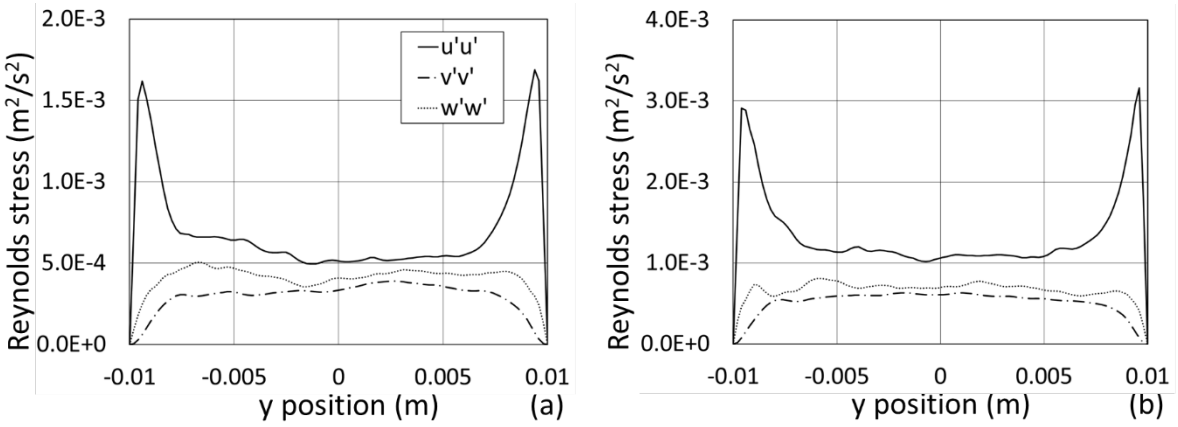

Figure 78. Comparison of turbulent isotropies for different initial shear rates, 45 (left figure), and 60 (right figure) s^{-1}.

5.2 High shear turbulent flow

The low shear turbulent flow simulations generate the central line shear rates, $\left(\frac{du}{dy}\right)_{center}$, from 13.3 to 24.4 s^{-1} which are comparable to the laminar shear flow. Thus we can directly compare the influence of turbulence on the interfacial forces in shear flow conditions. Now we want to extend the study to the high shear turbulent flow. When the bubble departs from a nucleate boiling point on a fuel rod surface, the bubble experiences a high shear rate on the order of ~10^3 s^{-1} [167]. This is the motivation of the high shear turbulent flow study. Block-induced turbulence algorithm is adopted as well. To resolve the near wall turbulent length scale and maintain reasonable computational cost, the simulation domain is adjusted from $0.2 \times 0.2 \times 0.1$ m^3 to $0.1 \times 0.1 \times 0.05$ m^3 and refinement boundary layers are added to the solid wall boundary as shown in Figure 79. The statistics of high shear turbulent flow cases are given in Table 16. Law of the wall profiles are shown in Figure 80 with coefficient $\kappa = 0.41$. With the value of coefficient *B* ranging from 5.2 to 6, good agreement is found between the DNS data and the log law (Eq. (11)).

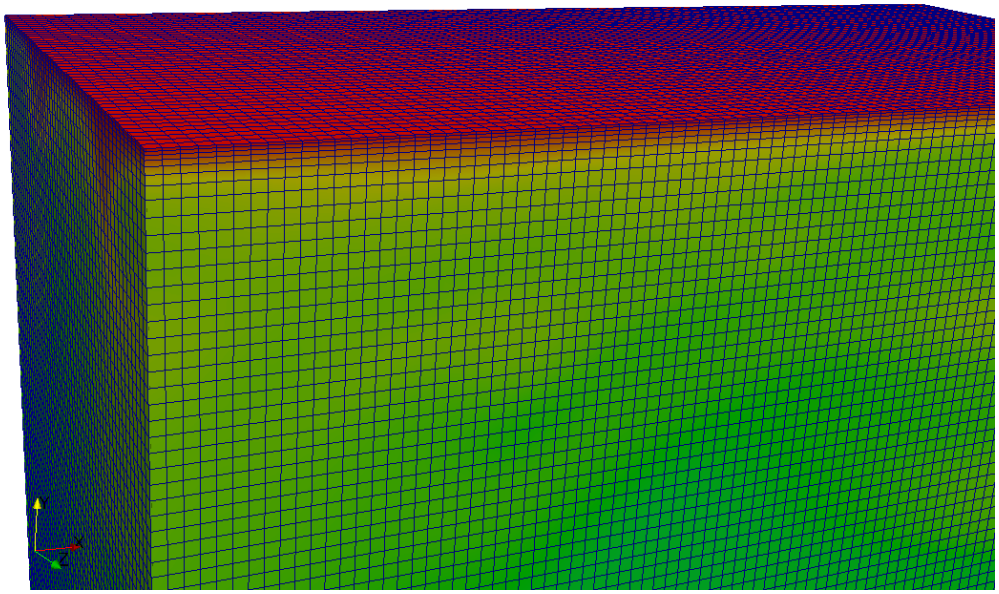

Figure 79. Refinement boundary layers near the wall for high shear turbulent flow simulations.

Table 16. Summary of the high shear single phase turbulent flow cases.

Initial shear rate (s^{-1})	Central-line relative velocity (m/s)	Re_τ	y+ (first layer on the wall)	$\left(\frac{du}{dy}\right)_{wall}$	$\left(\frac{du}{dy}\right)_{center}$
100	0.0	299.3	0.50	768.2	36.3
125	0.0	353.5	0.59	1071.2	47.7
150	0.0	390.4	0.65	1307.0	63.7

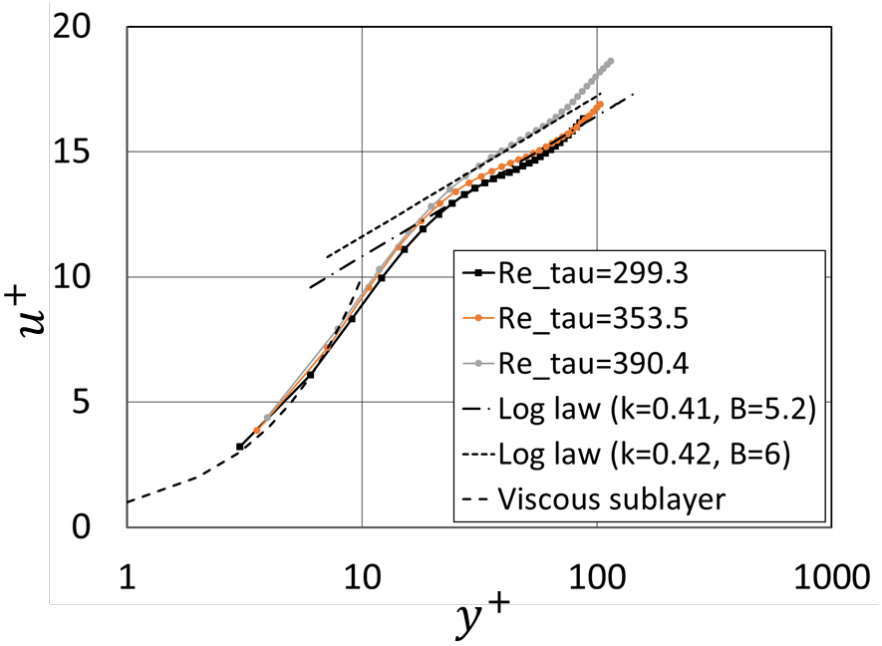

Figure 80. Law of the wall profile for high shear turbulent flow simulations.

Figure 81 compares the turbulent eddies with the identical Q-criterion value of $\pm$25000. As expected, high turbulent shear rate will induce more violent turbulent field. As first-principle based approach, DNS allows the capture of all the turbulent length scales. In Figure 82 and Figure 83, similar to the observation of low shear turbulent flow, $u'u'$ has a wall peak distribution while the $v'v'$ and $w'w'$ components are uniform across the lateral direction except the near wall region. Figure 84 shows the generation of a turbulent eddy near the wall due to the high shear velocity field and then this turbulent eddy is dissipated into the mainstream. Part of the future work is to implement the tracking capability of the turbulent eddies to the PHASTA. Then we can get a straightforward view of the eddies' generation and dissipation mechanism.

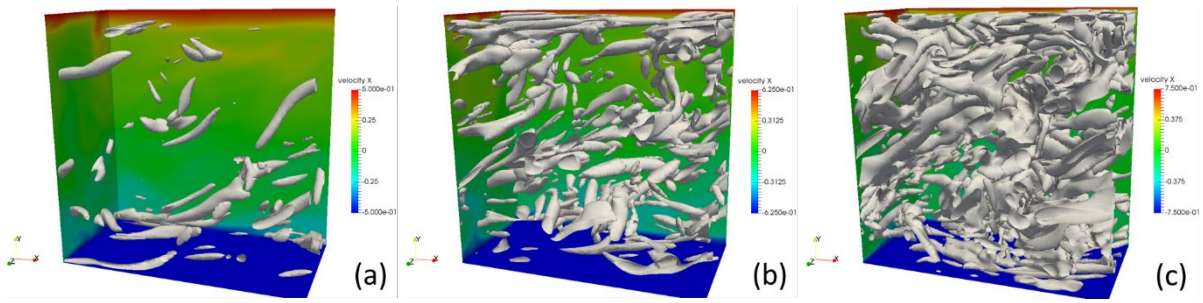

Figure 81. Comparison of turbulent eddies for different high shear turbulent flow cases. (a) to (c) represent the near wall shear rate, $\left(\frac{du}{dy}\right)_{wall}$, from 768.2 to 1307.0 s^{-1}. The contours are plotted by Q-criterion with value of ± 25000.

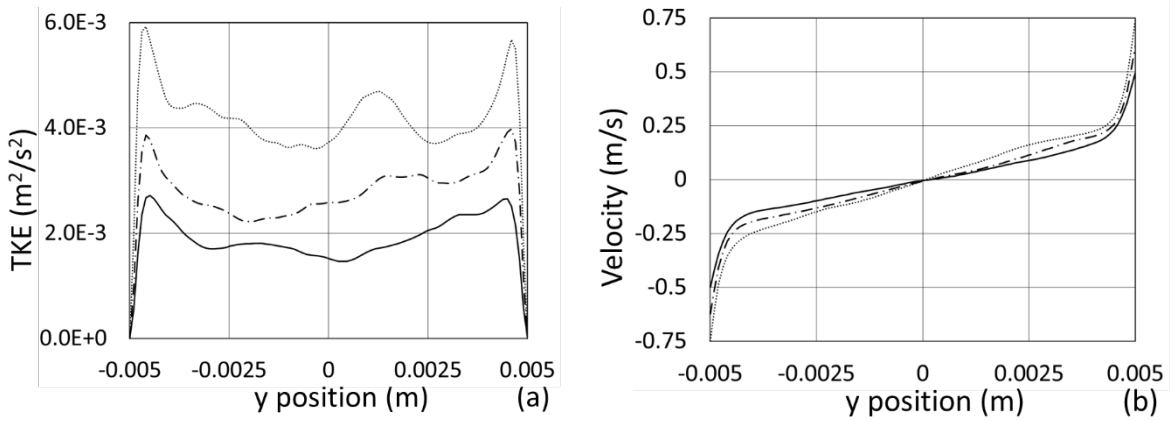

Figure 82. Comparison of TKE and velocity profiles for different near wall shear rates, 768.2 (solid line), 1071.2 (dash-dot line) and 1307.0 (dot line) s^{-1}.

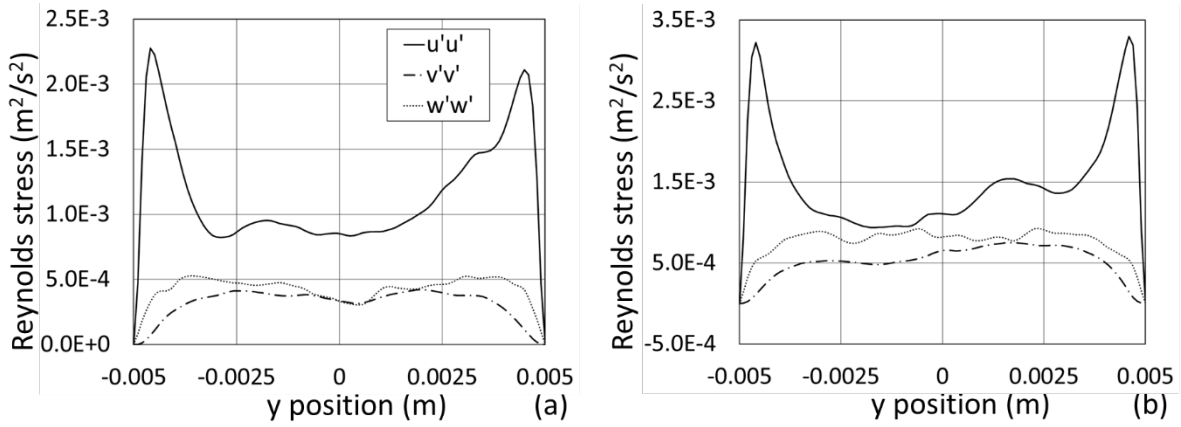

Figure 83. Comparison of turbulent isotropies for different near wall shear rates, 768.2 and 1071.2 s^{-1}.

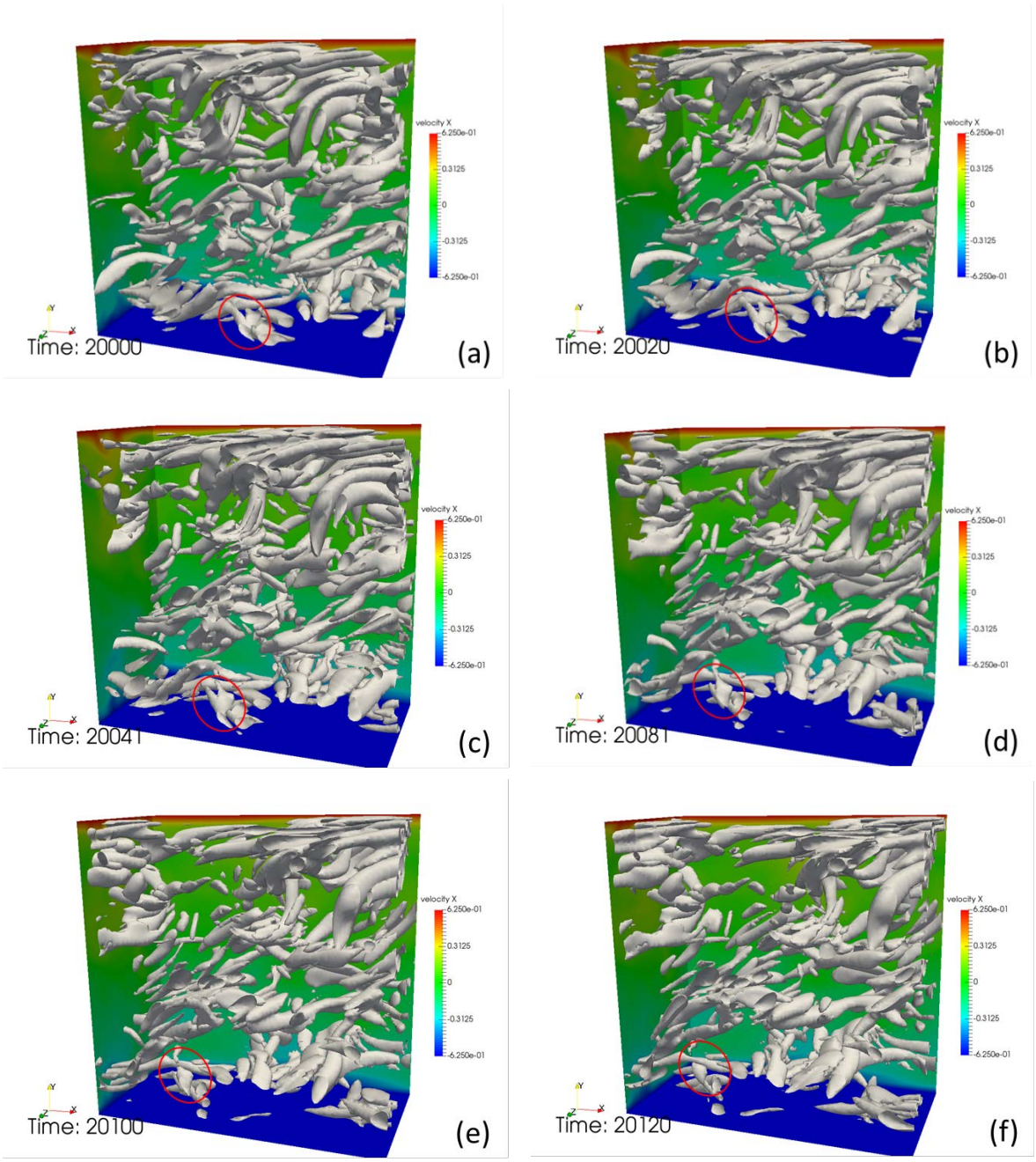

Figure 84. Evolution of a near wall turbulent eddy.

CHAPTER 6. CONCLUSIONS

In the present thesis, we evaluate the bubble-induced turbulence and interfacial forces using interface tracking approach. Advanced finite-element based flow solver (PHASTA) with level-set method is utilized to perform these studies. Several novel PHASTA techniques are developed and utilized. A PID bubble controller has been used to keep the bubble at fixed position to extract the interfacial forces. BCT parallel computing capability is developed as well by the author to accelerate the simulation and reduce the computational cost. The block-induced turbulence approach has been implemented to generate both homogeneous and shear singe-phase turbulent flows which are utilized as the inflow conditions for the production two-phase flow simulations.

The interfacial forces are evaluated under both laminar and turbulent flow conditions. The drag coefficient agrees well with the experiment-based correlation for spherical bubble. For laminar shear flow, we numerically simulate the two-phase shear flow with the exactly same setup of experiment and obtain fully consistent results. The sign change of bubble lateral motion direction is observed and it happens at $Eo_H = 5$. The bubble migration behavior near the wall is also investigated. The lift sign change is a coupled effect of wall distance, bubble deformation and bubble Reynolds number. We present the study on the effect of turbulent flow on the drag force experienced by a single bubble covering a parametric space which includes bubble deformability, relative velocity and turbulent intensity. A new DNS-informed correlation is proposed to predict the drag coefficient over the range we discussed and expected to be valid for bubble Reynolds number up to 900.

In addition to interfacial force terms, the bubble-induced turbulence is investigated under homogeneous turbulent flow condition. First, the homogeneous turbulent flow is generated using block-induced turbulence method on a very fine mesh to capture all the turbulent length scales. The quality of the generated turbulence is verified by comparing the rate of decay of homogeneous turbulence with the experiment-based correlations. A set of parametric studies has been conducted to evaluate the relationship between BIT and typical two-phase turbulent flow parameters, including relative velocity, turbulent intensity and bubble deformation level. Some insights are obtained regarding the energy transfer between turbulent eddies and bubble. The bubble-induced turbulence is observed to have a transition from liquid energy sink to enhancer as the bubble becomes more deformable. We also provide the preliminary results of shear turbulent flow study. The single phase shear turbulence are numerically generated over the range of ~10 s^{-1} to 10^3 s^{-1}. Good agreement between the DNS data and the "log law" is achieved with $k = 0.42$ and B ranging from 5.2 to 6.0. Fully resolved DNS study enables the observation of the process of turbulent eddies generation and dissipation in the shear turbulent field.

The studies presented in this thesis will result in the following key outcomes: (i) new high fidelity model of BIT incorporating dependencies on typical two-phase turbulent flow parameters; (ii) evaluation of interfacial forces for high-quality prediction of bubble distribution and dispersion in both laminar and turbulent flow scenarios; (iii) new microphysics-informed approach to the M-CFD closure laws.

CHAPTER 7. FUTURE WORK RECOMMENDATIONS

The present thesis summarizes the work have been done related to the simulation and modeling of the interactions between turbulent flow and bubbles and the evaluation of interfacial closures. The current research efforts can be expanded to the following topics to enhance our understanding on the physics behind the multiphase flow.

7.1 In-line motion of two bubbles and wake interaction

In the present thesis, we mainly focus on the evaluation of bubble-induced turbulence and interfacial closures on a single bubble which is important to the fundamental understanding. However, additional research effects should be placed on the multi-bubble interactions which is more widespread in the real experiment. In addition, the study of the interaction of two or multiple bubbles in a flow is a necessary step in the derivation of averaged equations for the multiphase flow. The existence of leading bubble will influence the migration of the trailing bubble. Yuan and Prosperetti [181] investigated the in-line motion of two spherical bubbles with a mixed spectral/finite-difference scheme for bubble Reynolds number up to 200. They found that those two bubbles will reach an equilibrium distance at which the wake effect and the inertial repulsion balance. Ruzicka [182] observed that the wake of the leading bubble influences the hydrodynamics of the trailing bubble, reducing the drag force of the latter and increasing its rise velocity. At certain distance and bubble Reynolds number, the sign change of drag force on the trailing bubble may occur. Currently, the PID bubble controller is adopted to apply the control forces on a single bubble. We can extend the bubble

control capability to control multiple bubble based on Jun's bubble tracking capability [166]. As a simplified example, a preliminary study about the mutual interaction between a lead solid hemisphere and a trailing bubble has been conducted. The evolution of the interaction between the single bubble and the wake region of hemisphere is given in Figure 85 where the bubble Reynolds number based on inflow velocity is 583. Figure 86 shows the evolution of streamwise control force (opposite of drag force). Positive control force is observed in the majority of the simulation which means that the bubble experiences the sign change of drag force and tends to migrate toward the hemisphere. Due to the high Re_b, the flow field is highly unstable and the wake region behind the hemisphere is time-dependent. Further investigations on the in-line motion of two bubbles need to add modification of the PID bubble controller and refine the mesh and flow properties setup.

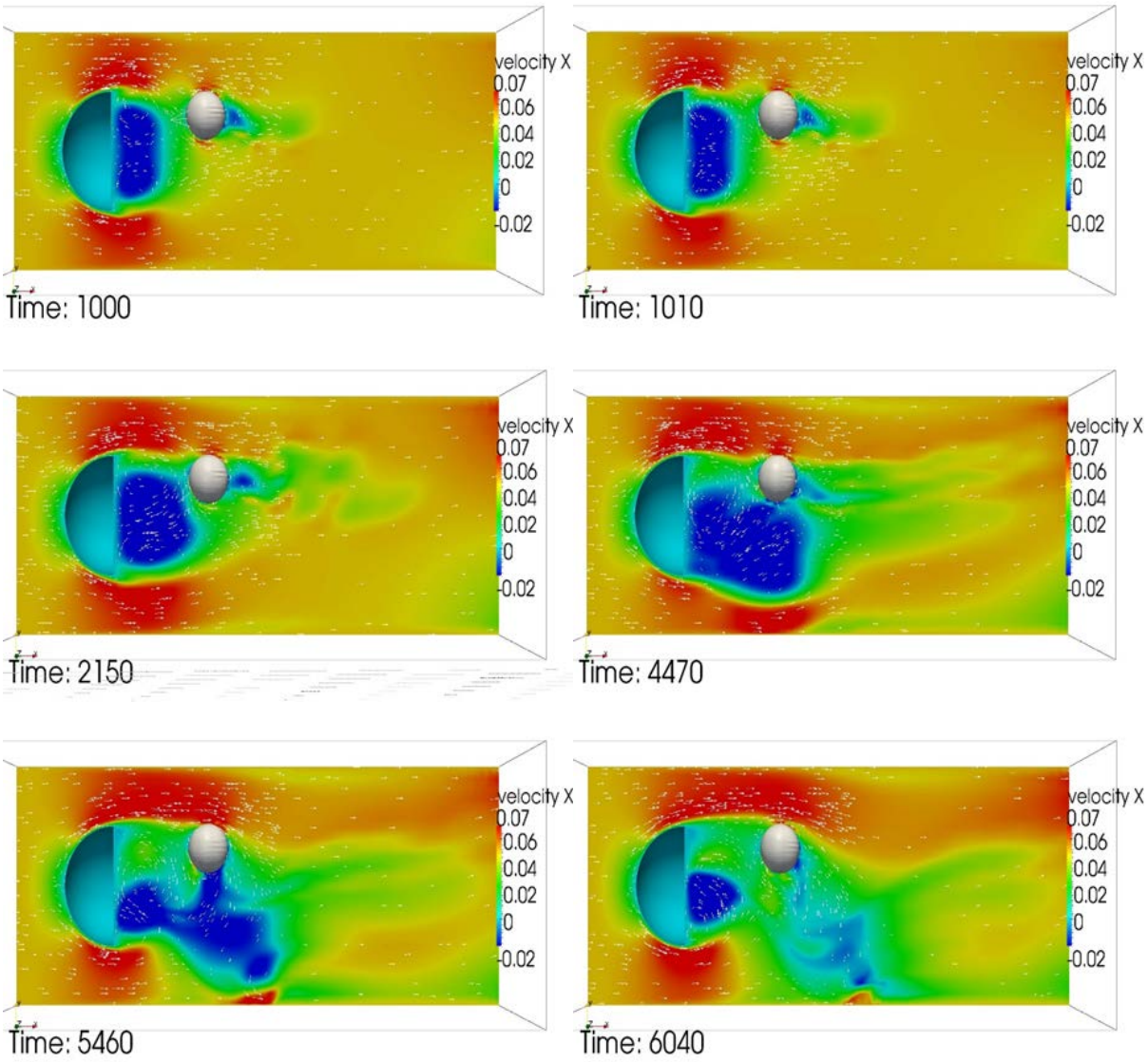

Figure 85. Evolution of the interaction between the bubble and wake region of hemisphere.

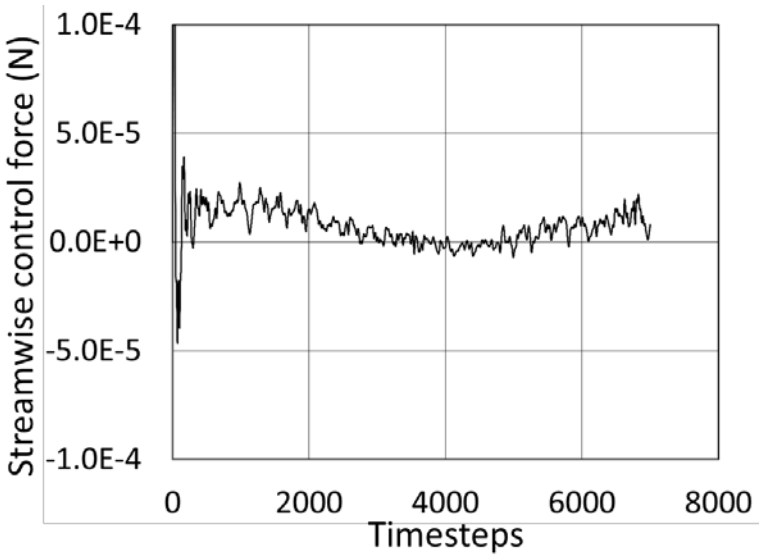

Figure 86. Evolution of streamwise control force for the study of the interaction between leading hemisphere and trailing bubble.

7.2 Interfacial forces of single bubble in turbulent boundary layers

In pipe flow or channel flow, the liquid flow has a parabolic velocity profile. Assuming the shear rate over a finite width in wall normal direction is constant, we can numerically evaluate the interfacial forces by assigning constant shear flow as boundary condition. However, there is an abrupt change of velocity gradient for the high shear velocity field near the wall which makes the measurement of shear rate challenging and creates difficulties for the PID bubble controller. The existence of solid wall boundary will make the problem more complex. Based on the author's knowledge, no literature has reported the interfacial closures of bubble under the abrupt change of velocity gradient. Figure 87 shows a full 3D replica of the boundary conditions from a large simulation domain with high shear turbulent flow. The BCT capability is improved to capture all the six surfaces of a small region in the large domain.

The recorded instantaneous velocity information is then identically translated as the boundary conditions for the small domain where we can introduce the bubble later. Figure 88 shows the velocity profile for the high shear turbulent flow which is generated using the block-induced turbulence algorithm. As shown in the plot, the near wall shear rate is about 5813 s^{-1} and the central line shear rate is about 207 s^{-1}. Abrupt change of velocity is observed in the dash square region and we want to investigate the bubble behavior in this region. In the presented research, we only use the low order control terms, dx, dx^2 and v, in the PID bubble controller in Eq. (63). To deal with this challenging problem, higher order control terms can help control the bubble. Additionally research efforts may need to improve the PID bubble controller algorithm and the conservation of the level-set contours.

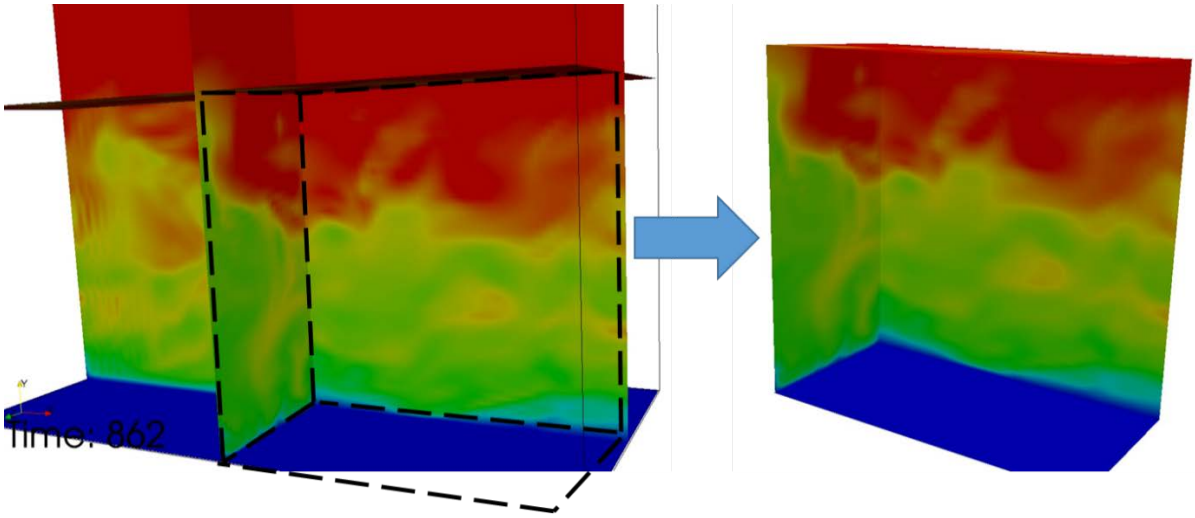

Figure 87. Full 3D replica of boundary conditions using BCT capability.

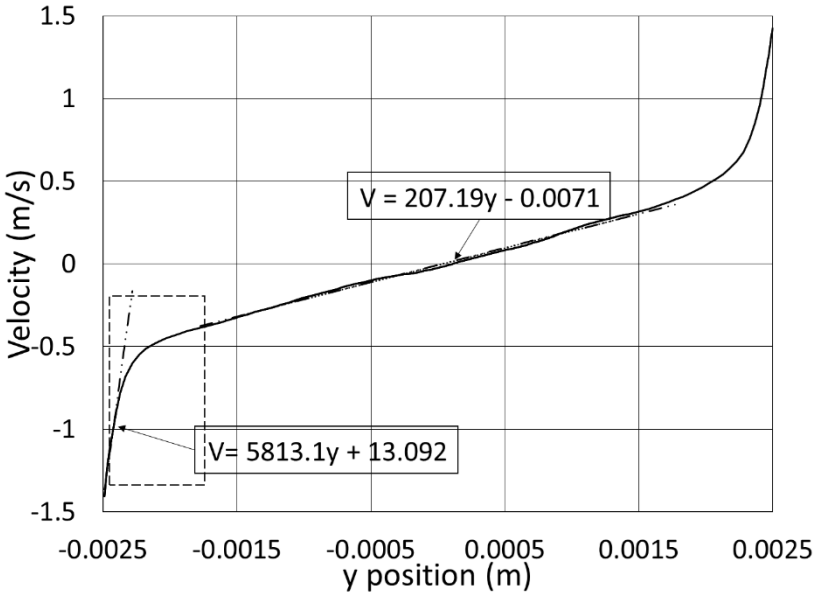

Figure 88. Wall normal velocity profile of high shear turbulent flow.

7.3 Data-driven analysis on the wall effect study

As discussed in the thesis, the modification of interfacial closures near the wall is strongly correlated to the wall distance, bubble deformation and relative velocity. The traditional linear regression approach is not able to obtain explicit closure laws due to the non-linear relationship between those parameters. Recently, the data-driven techniques, especially machine learning, advances rapidly and have been applied to two-phase flow modeling in several different contexts. Ling and Templeton[183] used machine learning to compare RANS results with DNS and LES predictions to identify regions of high uncertainty, presumably where the assumptions behind the RANS model no longer hold. Ma et al. [184] used neural networks to obtain closure relationships for laminar bubbly upflow in fully periodic domains from DNS results and found that the relationships allowed us to predict the evolution of

different initial conditions (velocity and void fraction profiles) using a simple two-fluid model for the average flow. Then Ma et al. [185] explored more complex scenario with the presence of wall in laminar bubbly upflows. They found that the average equations with the neural network closure reproduce the main aspects of the DNS results, including the generally rapid change initially, unsteadiness remaining after the initial adjustment and the final steadiness state. For the wall effect study, we can vary the crucial flow parameters and generate a series of cases within the typical range, i.e, $L/D \leq 2$, $1 \leq Eo \leq 10$ and $0.1 \leq Re_b \leq 100$. To ensure enough accuracy, the neural network shown in Figure 89 usually requires at least thousands of training cases. To save the computational cost, the author will recommend to only keep the "reserved" region shown in Figure 90 which will result in a total mesh size about 1.5 million. As a reference, it takes about 10,000 timesteps to obtain fully converged control forces which is an 18 hour simulation running on 64 cores. If we are able to run 1000 cases on 16,384 cores and assume the computational efficiency on a single core is identical as 64 cores' case, the wall-clock time is 2.95 days and the corresponding core-hours, i.e., the number of cores times the number of wall-clock hours, is 1.16×10^6 hours. So it is computationally feasible to perform this type of analysis using machine learning techniques.

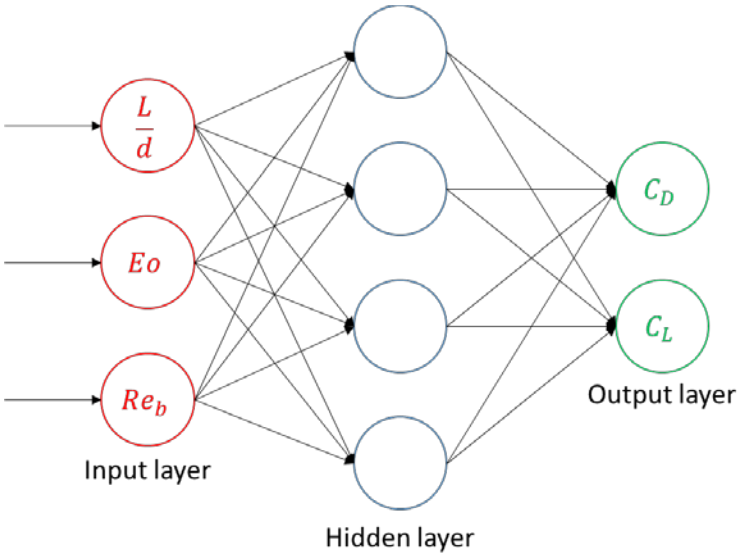

Figure 89. Illustration of neural network layout for wall effect study.

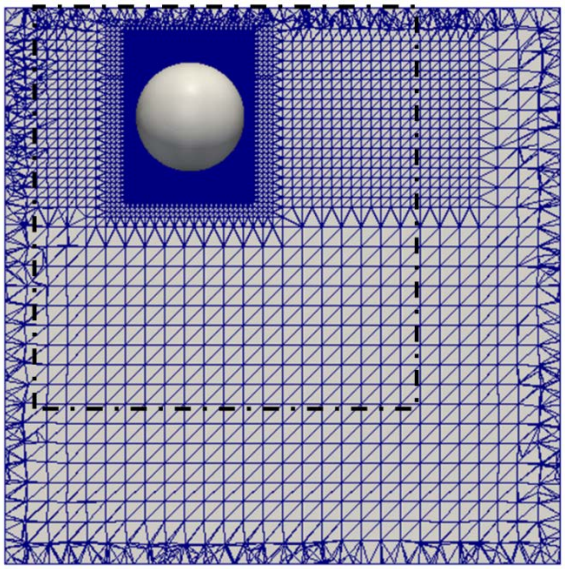

Figure 90. Mesh configuration of the wall effect study where the dash-dot rectangle represents the reserved region for future neural network study.

7.4 BIT in shear turbulent flow field

In the Chapter 5, the results of the single phase shear turbulent flow are presented. We numerically generate shear turbulent flow with near wall shear rate from ~10^2 s^{-1} to ~10^3 s^{-1} and the central line shear rate from ~10 s^{-1} to ~10^2 s^{-1}. As a bubble departs from a nucleate boiling point on a fuel rod surface, the bubble experiences a high shear rate on the order of ~10^3 s^{-1} [167]. It is important to understand the BIT under shear turbulent flow conditions and develop the correlation for the reactor relevant conditions. However, due to the nature of bubble-turbulence interaction and high shear rate shown in Figure 91, the control forces will oscillate much more dramatically than for the low shear laminar cases which leads to non-consistent drag and lift coefficients. The current PID bubble controller needed to be improved and the author suggest to incorporate an offset mechanism which considers the velocity gradient or vorticity near the bubble surface.

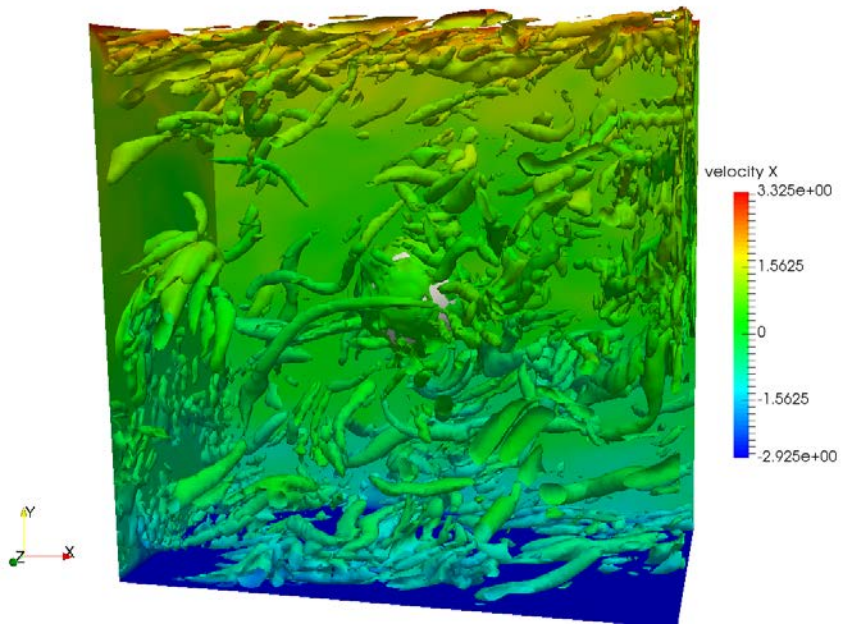

Figure 91. Single bubble immersed in high shear turbulent flow field where the initial shear rate is 1250 s^{-1}. The contour is plotted by Q-criterion and has constant value as $\pm 6\times10^{6}$ m/s^{2}

7.5 Verification of incompressibility assumption

The incompressible version of the PHASTA code is adopted for all the studies and the densities of both liquid and gas are assumed to be constant. However, all materials, whether gas, liquid or solid exhibit some change in volume when subjected to a compressive stress. If the incompressibility assumption is made in which densities are assumed to remain constant, it is important to know whether this assumption is valid or not. In some extreme conditions, like deformable bubble immersed in high shear turbulent flow, the pressure field inside the bubble may severely change over time. The proposed approach to verify the incompressibility assumption is to dynamically measure the integral of the pressure field inside the bubble over

time. The ideal gas law (given in Eq. (110)) states that the pressure, volume, and temperature in most gases are related as follows:

$$PV = nRT \qquad (110)$$

where P, V, and T are the pressure, volume and absolute temperature of the gas, respectively. n is the amount of substance of gas. R is the ideal gas constant.

In the adiabatic simulations where the temperature is constant, we can determine the gas volume fluctuations by measuring the integral of the pressure inside the bubble. We propose to compare the integral pressure field inside the bubble under both laminar and turbulent velocity scenarios to determine whether the existence of turbulent field will deteriorate the incompressible assumption. Another proposed plan is to investigate the influence of bubble deformation on incompressibility in turbulent flow field. The hypothesis is that the incompressibility assumption is valid and the pressure field fluctuation inside the bubble has minimal influence on the bubble volume. The evolution of the pressure field will elucidate the compressive stress inside the bubble, thus verifying the incompressibility assumption.

7.6 Closure law development—virtual mass and turbulent dispersion forces

We have spent significant research efforts on the interfacial closures, especially the drag and lift coefficient. The modifications of lift coefficient due to the wall presence are investigated as well. In Eq. (19), the accurate modeling of the other two interfacial forces, i.e, virtual mass force and turbulent dispersion force, are required for the complete M-CFD model. The virtual mass force comes into play when the dispersed phase, like spherical particle, is

accelerated through an inviscid fluid. Both drag force and virtual mass force act in the streamwise direction while the virtual mass force only exists during the transient period. The PID bubble controller takes the difference between the current bubble position and the proposed bubble position as an input and applies the full 3D control forces on the bubble by balancing the interfacial forces. To evaluate the virtual mass force, the author would add modification to the PID bubble controller. A constant control force, F_{xf}, is defined instead of automatically balancing the drag force. So the bubble will be released from the initial position and migrate with a certain acceleration. The trajectory of the single bubble is illustrated in Figure 92 and can be measured at each timestep. By extracting the streamwise overall control force and subtracting the drag force, the virtual mass force can be successfully obtained. However, the mesh configuration in the streamwise direction has to be homogeneous due to the bubble migration. To allow for enough bubble migration distance, the simulation domain has to be long enough or uses periodic boundary conditions in streamwise direction.

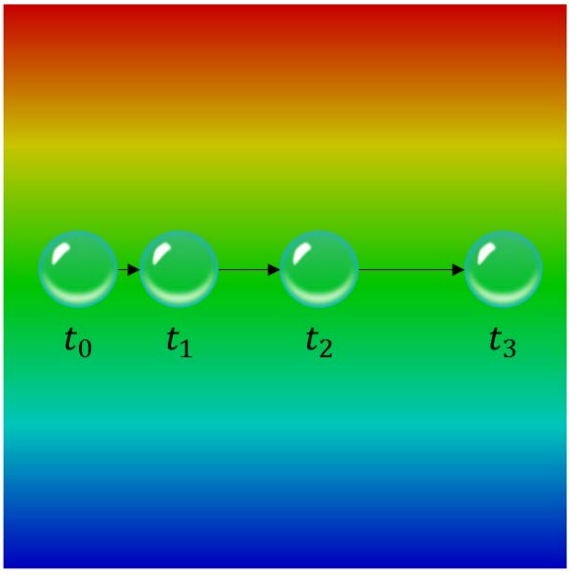

Figure 92. Trajectory of single bubble with constant acceleration in streamwise position.

The turbulent dispersion force is the result of the turbulent fluctuations of liquid velocity. The lift force, turbulent dispersion force and wall force act on the transverse direction. Their actions on the bubbles are as follows: the wall force drives the bubbles away from the wall, the lift force either push them toward the wall or pull them away from the wall based on the flow properties and the turbulent dispersion force tends to even out the void fraction gradient. Liquid turbulence and the void fraction gradient are closely related to the turbulent dispersion force as shown in (47). The author would suggest designing the two-phase shear turbulent flow cases with shear rates comparable to the laminar flow cases. Figure 93 shows a single bubble in low shear turbulent flow field and the centerline shear rate is around 16.8 s^{-1}. By comparing the wall-normal control forces between turbulent and laminar flow cases, we can gain insight on the influence of liquid turbulence on the interfacial forces.

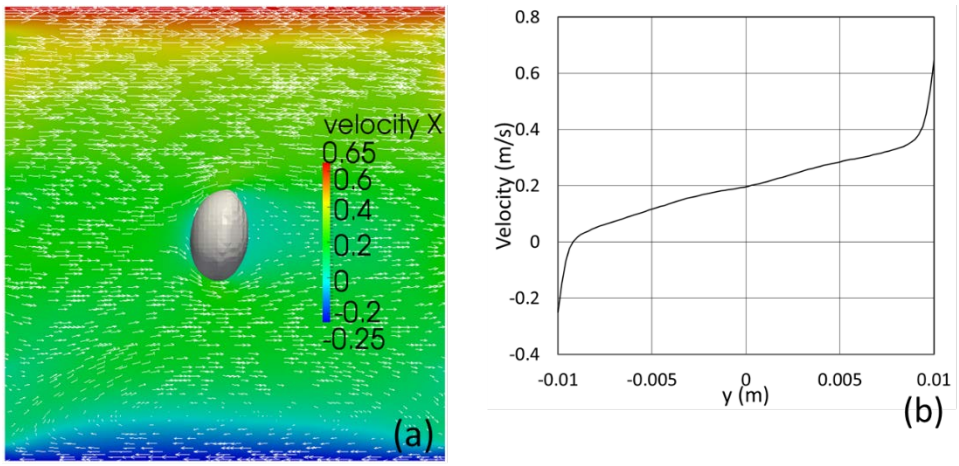

Figure 93. Single bubble in low shear turbulent flow field. (a) shows the shear velocity field around the bubble and (b) shows the single-phase streamwise velocity profile versus wall-normal position (y).

The influence of the void fraction gradient can be analyzed using simplified setup shown in Figure 94. We can place one pair of bubbles in the wall-normal direction with different top bubble sizes. In this way, we can simulate different void fraction distributions.

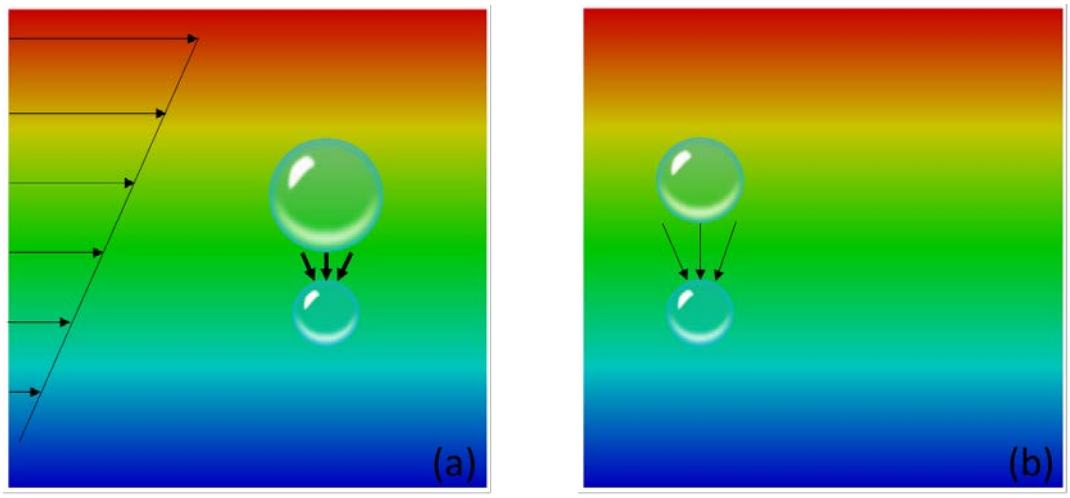

Figure 94. Illustration of bubble-bubble interaction in shear turbulent flow field. (a) and (b) represent higher and lower void fraction gradient near the bottom bubble, respectively.

REFERENCES

[1] Tomiyama, A., I. Kataoka, I. Zun and T. Sakaguchi, (1998). "Drag coefficients of single bubbles under normal and micro gravity conditions" *JSME international journal.Series B, fluids and thermal engineering*, 41(2), 472-479.

[2] Tomiyama, A., H. Tamai, I. Zun and S. Hosokawa, (2002). "Transverse migration of single bubbles in simple shear flows" *Chemical Engineering Science*, 57(11), 1849-1858.

[3] Zun, I., (1980). "Transverse migration of bubbles influenced by walls in vertical bubbly flow" *Int. J. Multiphase Flow*, 6, 583-588.

[4] Liu J., T., (1993). "Bubble size and entrance length effects on void development in a vertical channel" *Int.Journal of Multiphase Flow*, 19(1), 99-113.

[5] Hibiki, T. and M. Ishii, (1999). "Experimental study on interfacial area transport in bubbly two-phase flows." *Int. J. Heat Mass Transfer*, 42, 3019-3035.

[6] Hibiki, T., M. Ishii and Z. Xiao, (2001). "Axial interfacial area transport of vertical bubbly flows" *Int. J. Heat Mass Transfer*, 44, 1869-1888.

[7] Lu, J. and G. Tryggvason, (2008). "Effect of bubble deformability in turbulent bubbly upflow in a vertical channel" *Physics of Fluids (1994-present)*, 20(4), 040701.

[8] Dijkhuizen, W., M. van Sint Annaland and J. Kuipers, (2010). "Numerical and experimental investigation of the lift force on single bubbles" *Chemical engineering science*, 65(3), 1274-1287.

[9] Rzehak, R. and E. Krepper, (2013). "CFD modeling of bubble-induced turbulence" *Int. J. Multiphase Flow*, 55, 138-155.

[10] Sato, Y., M. Sadatomi and K. Sekoguchi, (1981). "Momentum and heat transfer in two-phase bubble flow—I. Theory" *Int. J. Multiphase Flow*, 7(2), 167-177.

[11] Lahey, R.T. and D.A. Drew, (2001). "The analysis of two-phase flow and heat transfer using a multidimensional, four field, two-fluid model" *Nucl. Eng. Des.*, 204(1), 29-44.

[12] Hill, D., D. Wang, A. Gosman and R. Issa, (1995). *"Numerical prediction of two-phase bubbly flow in a pipe" Proc. Second Int. Conf. Multiph. Flow,.*

[13] Kataoka, I. and A. Serizawa, (1989). "Basic equations of turbulence in gas-liquid two-phase flow" *Int. J. Multiphase Flow*, 15(5), 843-855.

[14] Pfleger, D. and S. Becker, (2001). "Modelling and simulation of the dynamic flow behaviour in a bubble column" *Chemical Engineering Science*, 56(4), 1737-1747.

[15] Hibiki, T., S. Hogsett and M. Ishii, (1998). "Local measurement of interfacial area, interfacial velocity and liquid turbulence in two-phase flow" *Nucl. Eng. Des.*, 184(2), 287-304.

[16] Lance, M. and J. Bataille, (1991). "Turbulence in the liquid phase of a uniform bubbly air–water flow" *J. Fluid Mech.*, 222, 95-118.

[17] Wang K., S., S. Lee J., O. Jones C. and R. Lahey T., (1987). "3-D turbulence structure and phase distribution measurements in bubbly two-phase flows" *Int. J. Multiphase Flow*, 13(3), 327-343.

[18] Ervin, E. and G. Tryggvason, (1997). "The rise of bubbles in a vertical shear flow" *Journal of Fluids Engineering*, 119(2), 443-449.

[19] Bunner, B. and G. Tryggvason, (2002). "Dynamics of homogeneous bubbly flows Part 1. Rise velocity and microstructure of the bubbles" *J. Fluid Mech.*, 466, 17-52.

[20] Batchelor, G.K., (2000) "An Introduction to Fluid Dynamics" Cambridge university press.

[21] Stewart, C., (1995). "Bubble interaction in low-viscosity liquids" *Int. J. Multiphase Flow*, 21(6), 1037-1046.

[22] Brücker, C., (1999). "Structure and dynamics of the wake of bubbles and its relevance for bubble interaction" *Physics of Fluids (1994-present)*, 11(7), 1781-1796.

[23] Bunner, B. and G. Tryggvason, (2003). "Effect of bubble deformation on the properties of bubbly flows" *J. Fluid Mech.*, 495, 77-118.

[24] Ilic, M., M. Worner and D. Cacuci G, (2004). "Balance of Liquid-phase Turbulence Kinetic Energy Equation for Bubble-train Flow" *J Nucl Sci Technol*, 41(3), 331-338.

[25] Lahey Jr, R.T. and D.A. Drew, (2000). *"An analysis of two-phase flow and heat transfer using a multidimensional, multi-field, two-fluid computational fluid dynamics (CFD) model" Japan/US Seminar on Two-Phase Flow Dynamics*, 5-8.

[26] Prosperetti, A., G. Tryggvason, (2007) "Computational Methods for Multiphase Flow" Cambridge university press.

[27] Pope, S.B., (2000) "Turbulent Flows" Cambridge university press.

[28] Prandtl, L., (1925). "Uber die ausgebildete Turbulenz" *ZAMM*, 5, 136-139.

[29] Boussinesq, J., (1877). "Theorie de l'Ecoulement Tourbillant" *Mem.Presentes par Divers Savants Acad.Sci.Inst.Fr*, 23, 46-50.

[30] Hinze, J.O., (1975) "Turbulence", 2nd ed. McGraw-Hill, New York.

[31] Kolmogorov, A.N., (1942). "Equations of Turbulent Motion of an Incompressible Fluids" *Izvestia Academy of Sciences, USSR, Physics*, 6(1-2), 56-58.

[32] Jones, W. and B. Launder, (1972). "The prediction of laminarization with a two-equation model of turbulence" *Int. J. Heat Mass Transfer*, 15(2), 301-314.

[33] Wilcox, D.C., (2002) "Turbulence Modeling for CFD" DCW Industries.

[34] Drew A., D., S. Passman L., (1998) "Theory of Multicomponent Fluids" Springer, New York.

[35] Podowski, M., (2009). "On the consistency of mechanistic multidimensional modeling of gas/liquid two-phase flows" *Nucl. Eng. Des.*, 239(5), 933-940.

[36] Ishii, M., T. Hibiki, (2006) "Thermo-Fluid Dynamics of Two-Phase Flow" Springer.

[37] Lahey Jr, R.T., (2005). "The simulation of multidimensional multiphase flows" *Nucl. Eng. Des.*, 235(10), 1043-1060.

[38] Kim, J., P. Moin and R. Moser, (1987). "Turbulence statistics in fully developed channel flow at low Reynolds number" *J. Fluid Mech.*, 177, 133-166.

[39] Lee, M. and R.D. Moser, (2015). "Direct numerical simulation of turbulent channel flow up to Re_tau 5200" *J. Fluid Mech.*, 774, 395-415.

[40] Bolotnov A., I., J.T. Lahey R., D. Drew A., K. Jansen E. and A. Oberai A., (2008). "A spectral turbulent cascade model for single- and two-phase uniform shear flows" *J.Turbulence*, 9(26), 1-18.

[41] Bolotnov, I.A., J. Lahey R.T., D.A. Drew, K.E. Jansen and A.A. Oberai, (2009). "Spectral Cascade Modeling of Turbulent Flow in a Channel" *Japanese Journal of Multiphase Flow*, 23(2), 190-204.

[42] Bolotnov, I.A., J. Lahey R.T., D.A. Drew, K.E. Jansen and A.A. Oberai, (2010). "Spectral Analysis of Turbulence Based on the DNS of a Channel Flow" *Comput. Fluids*, 39, 640-655.

[43] Scardovelli, R. and S. Zaleski, (1999). "Direct numerical simulation of free-surface and interfacial flow" *Annu. Rev. Fluid Mech.*, 31, 567-603.

[44] Hirt, C.W. and B.D. Nichols, (1981). "Volume of fluid (VOF) method for the dynamics of free boundaries" *Journal of computational physics*, 39(1), 201-225.

[45] Bunner, B. and G. Tryggvason, (2003). "Effect of bubble deformation on the properties of bubbly flows" *J. Fluid Mech.*, 495, 77-118.

[46] Unverdi, S.O. and G. Tryggvason, (1992). "A front-tracking method for viscous, incompressible, multi-fluid flows" *Journal of computational physics*, 100(1), 25-37.

[47] Sussman, M. and P. Smereka, (1997). "Axisymmetric free boundary problems" *J. Fluid Mech.*, 341, 269-294.

[48] Bolotnov, I.A., K.E. Jansen, D.A. Drew, A.A. Oberai and J.T. Lahey R., (2011). "Detached Direct Numerical Simulation of Turbulent Two-phase Bubbly Channel Flow" *Int. J. Multiphase Flow*, 37, 647-659.

[49] Sethian, A.J., (1999) "Level Set Methods and Fast Marching Methods" Cambridge University Press.

[50] Ilic, M., M. Worner and D. Cacuci G, (2007). *"Evaluation of energy spectra in bubble driven liquid flows from direct numerical simulations" International conference on Multiphase Flow, July 9-13, 2007,*.

[51] Tryggvason, G., S. Dabiri, B. Aboulhasanzadeh and J. Lu, (2012). *"Multiscale Issues in DNS of Multiphase Flows" Japan-U.S. seminar on Two-Phase flow Dynamics,*.

[52] Lu, J., S. Biswas and G. Tryggvason, (2006). "A DNS study of laminar bubbly flows in a vertical channel" *Int. J. Multiphase Flow*, 32(6), 643-660.

[53] Bolotnov, I.A., (2013). "Influence of Bubbles on the Turbulence Anisotropy" *ASME J. Fluids Eng.*, 135(5), 051301.

[54] Feng, J. and I.A. Bolotnov, (2016). *"Evaluation of bubble-induced turbulence using direct numerical simulation" International Topical Meeting on Advances in Thermal Hydraulics 2016*, New Orleans, LA.

[55] Bolotnov, I.A., F. Behafarid, D. Shaver, S. Antal P., K. Jansen E. and M. Podowski Z., (2012). "Coupled DNS/RANS Simulation of Fission Gas Discharge during Loss-of-Flow Accident of Gen-IV Sodium Fast Reactor" *Nuclear Technology Journal*, in press.

[56] Feng, J. and I.A. Bolotnov, (2017). "Interfacial force study on a single bubble in laminar and turbulent flows" *Nucl. Eng. Des.*, 313, 345-360.

[57] Richardson, L., (1922). "Weather prediction by numerical methods".

[58] Comte-Bellot, G. and S. Corrsin, (1966). "The use of a contraction to improve the isotropy of grid-generated turbulence" *J. Fluid Mech.*, 25(04), 657-682.

[59] Mohamed, M.S. and J.C. LaRue, (1990). "The decay power law in grid-generated turbulence" *J. Fluid Mech.*, 219, 195-214.

[60] Kolmogorov, A.N., (1941). *"Dissipation of energy in locally isotropic turbulence" Dokl. Akad. Nauk SSSR*, 32, 16-18.

[61] Kang, H.S., S. Chester and C. Meneveau, (2003). "Decaying turbulence in an active-grid-generated flow and comparisons with large-eddy simulation" *J. Fluid Mech.*, 480, 129-160.

[62] Samtaney, R., D.I. Pullin and B. Kosović, (2001). "Direct numerical simulation of decaying compressible turbulence and shocklet statistics" *Phys. Fluids*, 13(5), 1415-1430.

[63] Rose, W., (1966). "Results of an attempt to generate a homogeneous turbulent shear flow" *J. Fluid Mech.*, 25(01), 97-120.

[64] Ishii, M. and K. Mishima, (1984). "Two-fluid model and hydrodynamic constitutive relations" *Nucl. Eng. Des.*, 82(2), 107-126.

[65] Ishii, M. and T. Chawla, (1979). "Local drag laws in dispersed two-phase flow" Argonne National Lab., IL (USA).

[66] Drew, D. and R. Lahey, (1987). "The virtual mass and lift force on a sphere in rotating and straining inviscid flow" *Int. J. Multiphase Flow*, 13(1), 113-121.

[67] Antal, S., R. Lahey and J. Flaherty, (1991). "Analysis of phase distribution in fully developed laminar bubbly two-phase flow" *Int. J. Multiphase Flow*, 17(5), 635-652.

[68] Tomiyama, A., A. Sou, I. Zun, N. Kanami and T. Sakaguchi, (1995). "Effects of Eötvös number and dimensionless liquid volumetric flux on lateral motion of a bubble in a laminar duct flow" *Advances in multiphase flow*, 1995, 3-15.

[69] Podowski, M.Z., (2008). "Multidimensional modeling of two-phase flow and heat transfer" *Int. J. Numer. Methods Heat Fluid Flow*, 18(3/4), 491-513.

[70] Lopez de Bertodano, Martin A, (1998). "Two fluid model for two-phase turbulent jets" *Nucl. Eng. Des.*, 179(1), 65-74.

[71] Lahey, R., M.L. de Bertodano and O. Jones, (1993). "Phase distribution in complex geometry conduits" *Nucl. Eng. Des.*, 141(1), 177-201.

[72] Sato, Y. and K. Sekoguchi, (1975). "Liquid velocity distribution in two-phase bubble flow" *Int. J. Multiphase Flow*, 2(1), 79-95.

[73] Troshko, A. and Y. Hassan, (2001). "A two-equation turbulence model of turbulent bubbly flows" *Int. J. Multiphase Flow*, 27(11), 1965-2000.

[74] Hosokawa, S., A. Tomiyama, S. Misaki and T. Hamada, (2002). *"Lateral migration of single bubbles due to the presence of wall" ASME 2002 Joint US-European Fluids Engineering Division Conference*, 855-860.

[75] Odar, F., C. Murray, R. Shumway, M. Bolander, D. Barber and J. Mahaffy, (2003). "TRAC/RELAP Advanced Computational Engine (TRACE) V4. 0 User's Manual".

[76] Allison, C. and E. Johnson, (1990). "RELAP5/MOD3 code manual".

[77] George, T.L., (2001). "GOTHIC Containment Analysis Package Installation and Operations Manual " Numerical Applications, Inc.

[78] Salko, R.K. and M. Avramova, (2015). "CTF theory manual".

[79] Feng, J. and I.A. Bolotnov, (2017). "Evaluation of Bubble-Induced Turbulence Using Direct Numerical Simulation" *Int. J. Multiphase Flow*, 93, 92-107.

[80] Fang, J., J. Feng and I.A. Bolotnov, (2016). *"Integral and separate effect simulations of bubbly flows using interface tracking approach" CFD4NRS-6 Workshop*, Cambridge, MA.

[81] Fukuta, M., S. Takagi and Y. Matsumoto, (2008). "Numerical study on the shear-induced lift force acting on a spherical bubble in aqueous surfactant solutions" *Physics of Fluids (1994-present)*, 20(4), 040704.

[82] Launder E., B., D. Spaulding B., (1972) "Mathematical Models of Turbulence" Academic Press, London.

[83] Karman, T.V., (1937). "The fundamentals of the statistical theory of turbulence" *Journal of the Aeronautical Sciences*, 4(4), 131-138.

[84] Smagorinsky, J., (1963). "General circulation experiments with the primitive equations: I. The basic experiment" *Mon. Weather Rev.*, 91(3), 99-164.

[85] Lee, S., R. Lahey and O. Jones, (1989). "The Prediction of Two-Phase Turbulence and Phase Distribution Phenomena Using a K-κ Model" *混相流*, 3(4), 335-368.

[86] VARAKSIN, A.Y. and L.I. ZAICHIK, (2001). *"Effect of particles on the turbulence intensity of a carrier phase for gas-solid pipe flow" International symposium on multi-phase flow and transport phenomena*, 64-69.

[87] Anglart, H., O. Nylund, N. Kurul and M. Podowski, (1997). "CFD prediction of flow and phase distribution in fuel assemblies with spacers" *Nucl. Eng. Des.*, 177(1), 215-228.

[88] Ishii, M. and K. Mishima, (1980). *Study of two-fluid model and interfacial area*.

[89] Kurul, N. and M. Podowski, (1991). *"On the modeling of multidimensional effects in boiling channels" Proceedings of the 27th national heat transfer conference*, 301-314.

[90] Hadamard, J.S., (1911). "Mouvement permanent lent d'une sphere liquide et visqueuse dans un liquide visqueux" *C. R. Acad. Sci.*, 152, 1735.

[91] Moore, D., (1963). "The boundary layer on a spherical gas bubble" *J. Fluid Mech.*, 16(02), 161-176.

[92] Legendre, D. and J. Magnaudet, (1998). "The lift force on a spherical bubble in a viscous linear shear flow." *J. Fluid Mech.*, 368, 81-126.

[93] Bagchi, P. and S. Balachandar, (2003). "Effect of turbulence on the drag and lift of a particle" *Physics of Fluids (1994-present)*, 15(11), 3496-3513.

[94] Thomas, A.M., J. Fang, J. Feng and I.A. Bolotnov, (2015). "Estimation of shear-induced lift force in laminar and turbulent flows" *Nucl Technol*, 190(3), 274-291.

[95] Nagrath, S., K. Jansen, R.T. Lahey Jr and I. Akhatov, (2006). "Hydrodynamic simulation of air bubble implosion using a level set approach" *Journal of Computational Physics*, 215(1), 98-132.

[96] Drew, D., L. Cheng and R. Lahey, (1979). "The analysis of virtual mass effects in two-phase flow" *Int. J. Multiphase Flow*, 5(4), 233-242.

[97] Drew, D. and R. Lahey, (1987). "The virtual mass and lift force on a sphere in rotating and straining inviscid flow" *Int. J. Multiphase Flow*, 13(1), 113-121.

[98] Drew, D. and R. Lahey, (1993). "Analytical modeling of multiphase flow" *Particulate two-phase flow*, 509-566.

[99] Jiao, H. and M. Podowski, (2012). "An analysis of multidimensional models of gas/liquid flows" *Transactions of the American Nuclear Society*, 107, 1393.

[100] Shaver, D.R. and M.Z. Podowski, (2015). *"Modeling of interfacial forces for bubbly flows in subcooled boiling conditions" Transactions of the American Nuclear Society,* 113, 1368-1371.

[101] Sugioka, K. and T. Tsukada, (2015). "Direct numerical simulations of drag and lift forces acting on a spherical bubble near a plane wall" *Int. J. Multiphase Flow*, 71, 32-37.

[102] Takemura, F. and J. Magnaudet, (2003). "The transverse force on clean and contaminated bubbles rising near a vertical wall at moderate Reynolds number" *J. Fluid Mech.*, 495, 235-253.

[103] Pourtousi, M., J. Sahu and P. Ganesan, (2014). "Effect of interfacial forces and turbulence models on predicting flow pattern inside the bubble column" *Chemical Engineering and Processing: Process Intensification*, 75, 38-47.

[104] Saffman G., P., (1965). "The lift on a small sphere in a slow shear flow" *J. Fluid Mech.*, 22(2), 385-400.

[105] McLaughlin, J.B., (1991). "Inertial migration of a small sphere in linear shear flows" *J. Fluid Mech.*, 224, 261-274.

[106] Vasseur, P. and R. Cox, (1977). "The lateral migration of spherical particles sedimenting in a stagnant bounded fluid" *J. Fluid Mech.*, 80(3), 561-591.

[107] Cox, R. and S. Hsu, (1977). "The lateral migration of solid particles in a laminar flow near a plane" *Int. J. Multiphase Flow*, 3(3), 201-222.

[108] Clift, R., J.R. Grace, M.E. Weber, (2005) "Bubbles, Drops, and Particles" Courier Corporation.

[109] Ambari, A., B.G. Manuel and E. Guyon, (1983). "Effect of a plane wall on a sphere moving parallel to it" *Journal de Physique Lettres*, 44(4), 143-146.

[110] Nakoryakov, V., O. Kashinsky, B. Kozmenko and R. Gorelik, (1986). "Study of upward bubbly flow at low liquid velocities" *Izv.Sib.Otdel.Akad.Nauk SSSR*, 16, 15-20.

[111] Gorelik, R., O. Kashinskii and V. Nakoryakov, (1987). "Study of a downward bubbly flow in a vertical pipe" *Journal of Applied Mechanics and Technical Physics*, 28(1), 64-67.

[112] Takemura, F., S. Takagi, J. Magnaudet and Y. Matsumoto, (2002). "Drag and lift forces on a bubble rising near a vertical wall in a viscous liquid" *J. Fluid Mech.*, 461, 277-300.

[113] Zeng, L., S. Balachandar and P. Fischer, (2005). "Wall-induced forces on a rigid sphere at finite Reynolds number" *J. Fluid Mech.*, 536, 1-25.

[114] Zeng, L., F. Najjar, S. Balachandar and P. Fischer, (2009). "Forces on a finite-sized particle located close to a wall in a linear shear flow" *Phys. Fluids*, 21(3), 033302.

[115] Zaruba, A., D. Lucas, H. Prasser and T. Höhne, (2007). "Bubble-wall interactions in a vertical gas–liquid flow: Bouncing, sliding and bubble deformations" *Chemical engineering science*, 62(6), 1591-1605.

[116] Vhora, S., S. Cancelos and I. Bolotnov A, (2013). *"Interface tracking study of bubble/wall interaction" ANS Winter Meeting*, 109, 1618-1620.

[117] Lucas, D., E. Krepper and H. Prasser, (2007). "Use of models for lift, wall and turbulent dispersion forces acting on bubbles for poly-disperse flows" *Chemical Engineering Science*, 62(15), 4146-4157.

[118] Tomiyama, A., (1998). "Struggle with computational bubble dynamics" *Multiphase Science and Technology*, 10(4), 369-405.

[119] Moraga, F., A. Larreteguy, D. Drew and R. Lahey, (2003). "Assessment of turbulent dispersion models for bubbly flows in the low Stokes number limit" *Int. J. Multiphase Flow*, 29(4), 655-673.

[120] Zhang, H., T. Yokomine and T. Kunugi, (2015). "Turbulence modulation of the upward turbulent bubbly flow in vertical ducts" *Nuclear Engineering and Technology*, 47(5), 513-522.

[121] Metrailer, D., S. Reboux and D. Lakehal, (2015). *"Near-wall turbulence-bubbles interactions in a channel flow at Re_tau=400: a DNS/LES investigation" NURETH-16*, Chicago, IL.

[122] Serizawa, A., I. Kataoka and I. Michiyoshi, (1975). "Turbulence structure of air-water bubbly flow—III. Transport properties" *Int. J. Multiphase Flow*, 2(3), 247-259.

[123] Serizawa, A., I. Kataoka and I. Michiyoshi, (1975). "Turbulence structure of air-water bubbly flow—II. Local properties" *Int. J. Multiphase Flow*, 2(3), 235-246.

[124] Serizawa, A., I. Kataoka and I. Michiyoshi, (1975). "Turbulence structure of air-water bubbly flow—I. Measuring techniques" *Int. J. Multiphase Flow*, 2(3), 221-233.

[125] Shawkat E., M., C. Ching Y. and M. Shoukri, (2008). "Bubble and liquid turbulence characteristics of bubbly flow in a large diameter vertical pipe" *Int.J.of Multiphase Flow*, 34, 767-785.

[126] Hetsroni, G., (1989). "Particles-turbulence interaction" *Int. J. Multiphase Flow*, 15(5), 735-746.

[127] Gore, R. and C.T. Crowe, (1989). "Effect of particle size on modulating turbulent intensity" *Int. J. Multiphase Flow*, 15(2), 279-285.

[128] Serizawa, A. and I. Kataoka, (1990). "Turbulence suppression in bubbly two-phase flow" *Nucl. Eng. Des.*, 122(1), 1-16.

[129] Sato, Y., M. Sadatomi and K. Sekoguchi, (1981). "Momentum and heat transfer in two-phase bubble flow—II. A comparison between experimental data and theoretical calculations" *Int. J. Multiphase Flow*, 7(2), 179-190.

[130] Michiyoshi, I. and A. Serizawa, (1986). "Turbulence in two-phase bubbly flow" *Nucl. Eng. Des.*, 95, 253-267.

[131] Theofanous, T. and J. Sullivan, (1982). "Turbulence in two-phase dispersed flows" *J. Fluid Mech.*, 116, 343-362.

[132] Tsuji, Y., Y. Morikawa and K. Terashima, (1982). "Fluid-dynamic interaction between two spheres" *Int. J. Multiphase Flow*, 8(1), 71-82.

[133] Mudde, R., J. Groen and H. Van Den Akker, (1997). "Liquid velocity field in a bubble column: LDA experiments" *Chemical Engineering Science*, 52(21), 4217-4224.

[134] Rensen, J., S. Luther, J. de Vries and D. Lohse, (2005). "Hot-film anemometry in bubbly flow I: bubble–probe interaction" *Int. J. Multiphase Flow*, 31(3), 285-301.

[135] Mendez-Diaz, S., J. Serrano-Garcia, R. Zenit and J. Hernandez-Cordero, (2013). "Power spectral distributions of pseudo-turbulent bubbly flows" *Physics of Fluids (1994-present)*, 25(4), 043303.

[136] Bouche, E., V. Roig, F. Risso and A. Billet, (2012). "Homogeneous swarm of high-Reynolds-number bubbles rising within a thin gap. Part 1. Bubble dynamics" *J. Fluid Mech.*, 704, 211-231.

[137] Bouche, E., S. Cazin, V. Roig and F. Risso, (2013). "Mixing in a swarm of bubbles rising in a confined cell measured by mean of PLIF with two different dyes" *Exp. Fluids*, 54(6), 1-9.

[138] Bouche, E., V. Roig, F. Risso and A. Billet, (2014). "Homogeneous swarm of high-Reynolds-number bubbles rising within a thin gap. Part 2. Liquid dynamics" *J. Fluid Mech.*, 758, 508-521.

[139] Bolotnov A., I., R. Lahey T., D. Drew A. and K. Jansen E., (2008). "Turbulent Cascade modeling of single and bubbly two-phase turbulent flows" *Int. J. Multiphase Flow*, 34, 1142-1151.

[140] Brown, C. and I. Bolotnov, (2016). "Spectral Analysis of Single-and Two-Phase Bubbly DNS in Different Geometries" *Nucl. Sci. Eng.*, 184(3), 363-376.

[141] Merle, A., D. Legendre and J. Magnaudet, (2005). "Forces on a high-Reynolds-number spherical bubble in a turbulent flow" *J. Fluid Mech.*, 532, 53-62.

[142] Tokuhiro, A., M. Maekawa, K. Iizuka, K. Hishida and M. Maeda, (1998). "Turbulent flow past a bubble and an ellipsoid using shadow-image and PIV techniques" *Int. J. Multiphase Flow*, 24(8), 1383-1406.

[143] Saffman, P., (1956). "On the rise of small air bubbles in water" *J. Fluid Mech.*, 1(03), 249-275.

[144] Feng, J. and I.A. Bolotnov, (2016). *"Single bubble drag force evaluation in turbulent flow based on DNS results" ANS Winter Meeting*, 115, 1649.

[145] Feng, J. and I. Bolotnov, (2014). "Single deformable bubble interaction with turbulence in uniform and shear flows" *Bulletin of the American Physical Society*, 59.

[146] Jansen, K.E., (1999). "A stabilized finite element method for computing turbulence" *Comput. Methods Appl. Mech. Eng.*, 174(3), 299-317.

[147] Jansen, K.E., (1993). "Unstructured grid large eddy simulations of wall bounded flows" *Annual Research Briefs, Center for Turbulence Research, NASA Ames/Stanford University*, 151.

[148] Sahni, O., J. Müller, K.E. Jansen, M.S. Shephard and C.A. Taylor, (2006). "Efficient anisotropic adaptive discretization of the cardiovascular system" *Comput. Methods Appl. Mech. Eng.*, 195(41), 5634-5655.

[149] Tejada-Martínez, A.E. and K.E. Jansen, (2006). "A parameter-free dynamic subgrid-scale model for large-eddy simulation" *Comput. Methods Appl. Mech. Eng.*, 195(23), 2919-2938.

[150] Whiting, C.H. and K.E. Jansen, (2001). "A stabilized finite element method for the incompressible Navier-Stokes equations using a hierarchical basis" *Int. J. Numer. Methods Fluids*, 35(1), 93-116.

[151] Trofimova, A.V., A.E. Tejada-Martínez, K.E. Jansen and R.T. Lahey Jr, (2009). "Direct numerical simulation of turbulent channel flows using a stabilized finite element method" *Comput. Fluids*, 38(4), 924-938.

[152] Araya, G., L. Castillo, C. Meneveau and K. Jansen, (2011). "A dynamic multi-scale approach for turbulent inflow boundary conditions in spatially developing flows" *J. Fluid Mech.*, 670, 581-605.

[153] Sussman, M., A.S. Almgren, J.B. Bell, P. Colella, L.H. Howell and M.L. Welcome, (1999). "An adaptive level set approach for incompressible two-phase flows" *Journal of Computational Physics*, 148(1), 81-124.

[154] Galimov, A., (2007) "An Analysis of Interfacial Waves and Air Ingestion Mechanisms" ProQuest.

[155] Galimov Yu., A., O. Sahni, M. Shephard, D. Drew A, K. Jansen E. and R. Lahey T., (2010). "Parallel Adaptive Simulation of a Plunging Liquid Jet" *Acta Mathematica Scientia*, 30(2), 522-538.

[156] Rodriguez, J., O. Sahni, R. Lahey and K. Jansen, (2013). "A parallel adaptive mesh method for the numerical simulation" *Computers and Fluids*, 87, 115-131.

[157] Behafarid, F., K. Jansen and M. Podowski, (2015). "A study on large bubble motion and liquid film in vertical pipes and inclined narrow channels" *Int. J. Multiphase Flow*, 75, 288-299.

[158] Maneri, C. and N. Zuber, (1974). "An experimental study of plane bubbles rising at inclination" *Int. J. Multiphase Flow*, 1(5), 623-645.

[159] Fang, J., M. Rasquin and I.A. Bolotnov, (2017). "Interface tracking simulations of bubbly flows in PWR relevant geometries" *Nucl. Eng. Des.*, 312, 205-213.

[160] Sahni, O., C. Carothers D, M. Shephard S and K. Jansen E, (2009). "Srtong Scaling analysis of a parallel, unstructured, implicit solver and the influence of the operating system interference" *Scientific Programming*, 17, 261-274.

[161] Rasquin, M., C. Smith, K. Chitale, E.S. Seol, B.A. Matthews, J.L. Martin, O. Sahni, R.M. Loy, M.S. Shephard and K.E. Jansen, (2014). "Scalable Implicit Flow Solver for Realistic Wing Simulations with Flow Control" *Computing in Science & Engineering*, 16(6), 13-21.

[162] Squillacote, A.H., (2007) "The ParaView Guide: A Parallel Visualization Application" Kitware.

[163] Brackbill, J.U., D.B. Kothe and C. Zemach, (1992). "A continuum method for modeling surface tension" *Journal of computational physics*, 100(2), 335-354.

[164] Sussman, M. and E. Fatemi, (1999). "An efficient, interface-preserving level set re-distancing algorithm and its application to interfacial incompressible fluid flow" *Siam J.on Scientific Computing*, 20(4), 1165-1191.

[165] Sussman, M., E. Fatemi, P. Smereka and S. Osher, (1998). "An improved level set method for incompressible two-phase flows" *Comput. Fluids*, 27(5), 663-680.

[166] Fang, J., (2016). "Development of Advanced Analysis Toolkit for Turbulent Bubbly Flow Simulations.".

[167] Thomas, A.M., J. Fang and I.A. Bolotnov, (2014). *"Estimation of Shear-induced Lift Force in Laminar and Turbulent Flows" International Topical Meeting on Advances in Thermal Hydraulics - 2014 (ATH '14)*, Reno, NV.

[168] Sussman, M., P. Smereka and S. Osher, (1994). "A level set approach for computing solutions to incompressible two-phase flow" *Journal of Computational physics*, 114(1), 146-159.

[169] Owen, P. and H. Zienkiewicz, (1957). "The production of uniform shear flow in a wind tunnel" *J. Fluid Mech.*, 2(6), 521-531.

[170] Bolotnov, I.A., (2011). *"Direct numerical simulation of turbulent flow in a channel with different types of surface roughness" 64rd Annual Meeting of the APS Division of Fluid Dynamics*,.

[171] Lu, J. and G. Tryggvason, (2006). "Numerical study of turbulent bubbly downflows in a vertical channel" *Phys. Fluids*, 18(10), 103302.

[172] Marie, J., (1987). "Modelling of the skin friction and heat transfer in turbulent two-component bubbly flows in pipes" *Int. J. Multiphase Flow*, 13(3), 309-325.

[173] Roache, P.J., (1998). "Verification of codes and calculations" *AIAA J.*, 36(5), 696-702.

[174] Roache, P.J., (1998) "Verification and Validation in Computational Science and Engineering" Hermosa.

[175] Richardson, L.F., (1911). "The approximate arithmetical solution by finite differences of physical problems involving differential equations, with an application to the stresses in a masonry dam" *Philosophical Transactions of the Royal Society of London.Series A, Containing Papers of a Mathematical or Physical Character*, 210, 307-357.

[176] Richardson, L.F. and J.A. Gaunt, (1927). "The deferred approach to the limit. Part I. Single lattice. Part II. Interpenetrating lattices" *Philosophical Transactions of the Royal Society of London.Series A, containing papers of a mathematical or physical character*, 226, 299-361.

[177] Dabiri, S., J. Lu and G. Tryggvason, (2013). "Transition between regimes of a vertical channel bubbly upflow due to bubble deformability" *Physics of Fluids (1994-present)*, 25(10), 102110.

[178] Bernoulli, D., (1738). "Hydrodynamica".

[179] Jeong, J. and F. Hussain, (1995). "On the identification of a vortex" *J. Fluid Mech.*, 285, 69-94.

[180] Rensen, J., S. Luther and D. Lohse, (2005). "The effect of bubbles on developed turbulence" *J. Fluid Mech.*, 538, 153-187.

[181] Yuan, H. and A. Prosperetti, (1994). "On the in-line motion of two spherical bubbles in a viscous fluid" *J. Fluid Mech.*, 278, 325-349.

[182] Ruzicka, M., (2000). "On bubbles rising in line" *Int. J. Multiphase Flow*, 26(7), 1141-1181.

[183] Ling, J. and J. Templeton, (2015). "Evaluation of machine learning algorithms for prediction of regions of high Reynolds averaged Navier Stokes uncertainty" *Physics of Fluids (1994-present)*, 27(8), 085103.

[184] Ma, M., J. Lu and G. Tryggvason, (2015). "Using statistical learning to close two-fluid multiphase flow equations for a simple bubbly system" *Physics of Fluids (1994-present)*, 27(9), 092101.

[185] Ma, M., J. Lu and G. Tryggvason, (2016). "Using statistical learning to close two-fluid multiphase flow equations for bubbly flows in vertical channels" *Int. J. Multiphase Flow*, 85, 336-347.

APPENDICES

Appendix A

This appendix provides the step-by-step derivation of the relationship between Reynolds number and mesh size. DNS should resolve all the spatial scales down to the Kolmogorov length scale which is expressed as

$$\eta = \left(\frac{\nu^3}{\varepsilon}\right)^{\frac{1}{4}} \quad (111)$$

Considering an integral length L and the number of points N along a given mesh direction, we assume that the mesh elements are identical and the length of each mesh is h.

$$Nh = L \quad (112)$$

The single mesh length h should be less than η. Then we get

$$N\eta \geq L \quad (113)$$

$$N \geq \frac{L}{\eta} = \frac{L\varepsilon^{\frac{1}{4}}}{\nu^{\frac{3}{4}}} \quad (114)$$

Note that the dissipation rate ε is proportional to $\frac{u'^3}{L}$ where $u' = \sqrt{\frac{1}{3}({u'_1}^2 + u'^2_2 + u'^3_3)}$. We can insert the expression of ε to Eq. (114).

$$N \geq \frac{Lu'^{\left(\frac{3}{4}\right)}}{L^{\frac{1}{4}}\nu^{\frac{3}{4}}} = \left(\frac{u'L}{\nu}\right)^{\frac{3}{4}} = Re^{\frac{3}{4}} \quad (115)$$

For the full 3D DNS, the minimum total mesh size is given as follows and it grows exponentially with power of $9/4$:

$$N^3 \geq \left(Re^{\frac{3}{4}}\right)^3 = Re^{\frac{9}{4}} \quad (116)$$

Appendix B

This appendix contains the control coefficients setup of the PID bubble controller for different laminar and turbulent flow scenarios.

The full expression of the PID bubble control is expressed as follows:

$$CF_i^{(n+1)} = c_1\overline{CF_i^{(n)}} + c_2\left[CF_i^{(n)} + c_3 dx_i^{(n)} + c_4 dx_i^{2(n)} + c_5 dx_i^{3(n)} + c_6 v_i^{(n)} + c_7 v_i^{2(n)} + c_8 v_i^{3(n)} + c_9 dv_i^{(n)}\right] + \left[c_{10} dx_2^{2(n)}\right]_{if\ i=1} \quad (117)$$

The validation study of PID bubble controller shown in Figure 7 adopts the following control coefficients setup:

Table 17. Control coefficients setup for the validation study of PID bubble controller.

Control coefficients	c_1	c_2	c_3	c_4	c_5	c_6	c_9
Streamwise direction (x) controls	0.1	0.9	200.0	2.0	4.0	20.0	60.0
Wall-normal direction (y) controls	0.2	0.8	200.0	2.0	4.0	60.0	60.0
Lateral direction (z) controls	0.2	0.8	200.0	2.0	4.0	60.0	60.0

After enough test and trials, we observe that the higher order terms of the PID bubble controller will have small influence on the stability of the bubble control and identical control coefficient setup in all three directions has better bubble control performance, especially in the scenarios of highly deformable bubble and turbulent flow field. A simplified version of the PID bubble controller is described as follows

$$CF_i^{(n+1)} = c_1\overline{CF_i^{(n)}} + c_2\left[CF_i^{(n)} + c_3 dx_i^{(n)} + c_4 dx_i^{2(n)} + c_5 v_i^{(n)}\right] \quad (118)$$

The evaluation of interfacial closures in laminar shear velocity field and homogeneous turbulent flow field adopts the following control coefficients setup:

Table 18. Control coefficients setup for the evaluation of lift forces in laminar shear field and turbulent flow field.

Control coefficients	c_1	c_2	c_3	c_4	c_5
All directions (x, y and z)	0.2	0.8	5.0×10^6	5.0×10^4	5.0×10^6

Appendix C

This appendix contains the various portions of the transient boundary conditions (BCT) capability modules in PHASTA.

genbc.f: determine the surface ID and extract all the elements' information on that surface.

```
if(nsidg.gt.0) then       ! if there are any surfID's
nsurf(:) = 0
do k = 1, nsidg        ! loop over Surface ID's
sid = sidmapg(k)
firstvisit(:)=.true.
wnrm(:,1:3)=zero
do iblk=1, nelblb   ! loop over boundary element blocks
npro = lcblkb(1,iblk+1)-lcblkb(1,iblk)
nenbl = lcblkb(6,iblk)
nshl = lcblkb(9,iblk)
allocate( ienb(nshl) )
do i = 1, npro   ! loop over boundary elements
iBCB1=miBCB(iblk)%p(i,1)
iBCB2=miBCB(iblk)%p(i,2)
ienb(1:nshl)=mienb(iblk)%p(i,1:nshl)
! We want to print out SurfID coordinates even if they are not on a
modeled surface:
!  (btest condition has been moved downstream by Igor)
! don't bother with elements that don't lie on the current surface
if (iBCB2.ne.sid) cycle
!
!.... calculate this element's area-weighted normal vector
!
e1 = x(ienb(2),:)-x(ienb(1),:)
e2 = x(ienb(3),:)-x(ienb(1),:)
elnrm(1) = e1(2)*e2(3)-e1(3)*e2(2)
elnrm(2) = e1(3)*e2(1)-e1(1)*e2(3)
elnrm(3) = e1(1)*e2(2)-e1(2)*e2(1)
if (iRBCT.eq.0) then
if (sid.eq.10.or.sid.eq.11) then
if (inew.eq.1) then
if( myrank.ge.0 .and. myrank.le.9)then
write(filenum,'(i1.1)')myrank
else if(myrank.ge.10 .and. myrank.le.99)then
write(filenum,'(i2.2)')myrank
else if(myrank.ge.100 .and. myrank.le.999)then
write(filenum,'(i3.3)')myrank
else if(myrank.ge.1000 .and. myrank.le.9999)then
write(filenum,'(i4.4)')myrank
else if(myrank.ge.10000 .and. myrank.le.99999)then
write(filenum,'(i5.5)')myrank
else if(myrank.ge.100000 .and. myrank.le.999999)then
write(filenum,'(i6.6)')myrank
```

```
else if(myrank.ge.1000000 .and. myrank.le.9999999)then
write(filenum,'(i7.7)')myrank
else if(myrank.ge.10000000 .and. myrank.le.99999999)then
write(filenum,'(i8.8)')myrank
else if(myrank.ge.100000000 .and. myrank.le.999999999)then
write(filenum,'(i9.9)')myrank
else if(myrank.ge.1000000000 .and. myrank.le.9999999999)then
write(filenum,'(i10.10)')myrank
end if
open(93+myrank,file='../bct.dat.'//trim(filenum)//'',status='replace')
inew = 0
end if

do j12 = 1, nenbl  ! Number of nodes on the boundary face
write(93+myrank, '(I6, 10E15.7)') myrank, x(ienb(j12), :)
end do
end if !sid
end if !iRBCT
```

bctint.f: reads the input bct.dat files for the production cases and implement the instantaneous velocity profiles on multiple cores.

```
    !  This one should be used for boundary layer meshes where bct.dat
must
    !  be given to greater precision than is currently being generated.
    epsd=1.0d-12            ! this is distance SQUARED to save square root
    ic=0                      !count the number on this processor
    if (iRBCT.eq.0) then !read original bct.dat and generate multi bct
files
    write(*,*) 'read bct.dat and generate bct.dat.ID'
    ic=0
    if(any(ibits(iBC,3,3).eq.7)) then
    open(unit=567, file='bct.dat',ACTION='READ',STATUS='old')
    ! reading the #of nodal points - ntv, and #of time series  - ntpts.
    read(567,*) ntv,nptsmax
    allocate (nBCt(numnp))
    allocate (numBCt(ntv))
    if (tvbcswitch.eq.0) then
    allocate (BCt(ntv,nptsmax,4))
    else
    allocate (BCt(ntv,nptsmax,ndof+1))
    allocate (rj_temp(ndof+1))
    endif
    endif
    else if (iRBCT.eq.1) then !read multi bct.dat.*1.*2
    write(*,*) 'read the data of boundary points on each processor'
    call MPI_BARRIER (MPI_COMM_WORLD,ierr)
    ic=0
```

```
    if( myrank.ge.0 .and. myrank.le.9)then
    write(filenum1,'(i1.1)')myrank
    else if(myrank.ge.10 .and. myrank.le.99)then
    write(filenum1,'(i2.2)')myrank
    else if(myrank.ge.100 .and. myrank.le.999)then
    write(filenum1,'(i3.3)')myrank
    else if(myrank.ge.1000 .and. myrank.le.9999)then
    write(filenum1,'(i4.4)')myrank
    end if
    call MPI_BARRIER (MPI_COMM_WORLD,ierr)
    inquire(file='bct.dat.1.'//trim(filenum1)//'',exist=extsbct)
    call MPI_BARRIER (MPI_COMM_WORLD,ierr)
    if(extsbct) then
    iextsbct=1
    endif
    if(iextsbct.eq.1) then

open(1989,file='bct.dat.1.'//trim(filenum1)//'',action='read',status='old')
    write(*,*) 'bct.dat.1.', myrank, 'is reading'
    read(1989,*) ntv,nptsmax
    allocate (nBCt(numnp))
    allocate (numBCt(ntv))
    allocate (BCt(ntv,nptsmax,4))
    do k=1,ntv
    read(1989,*) x1,x2,x3,ntpts
    do i=1,numnp
    if(ibits(ibc(i),3,3) .eq.7) then
    dd= distds(x1,x2,x3,x(i,1),x(i,2),x(i,3))
    if(dd.lt.epsd) then
    ic=ic+1
    nBCt(ic)=i ! the pointer to this point
    numBCt(ic)=ntpts ! the number of time series
    do j=1,ntpts
    if (tvbcswitch.eq.0) then
    read(1989,*) (BCt(ic,j,n),n=1,4)
    BCt(ic,j,1)=BCt(ic,j,1)+shvebct !Jinyong, Jan-2015:apply velocity
shift
    else
    !************Now the structure of the BCT.dat is changed: previuos
structure was: u v w t
    !***********it is replaced by follows: t p u v w sc1 sc2 ..
    read(1989,*) (BCt(ic,j,n),n=1,ndof+1)
    BCt(ic,j,1)=BCt(ic,j,1)+shvebct
    endif
    enddo
    exit
    endif
    endif
    enddo !numnp
    enddo !ntv
    BCt(:,:,4)=BCt(:,:,4)*bcttimescale
    itvn=ic
    close(1989)
```

```
if (ic.gt.0) then
write(*,*) 'myrank=',myrank,' and I found ',ic,'nodes.'
endif
endif
endif !end if iRBCT==0
return
end
```

Appendix D

This appendix contains the various subroutines to convert the recorded instantaneous velocity history files (varts data) to the readable bct files for PHASTA.

BCTMerge.f: merge the multiple varts data files into single file.

```
! read the current case path:
open(101, file = 'path.dat')
read(101, 50) ipath
50    format(A80)
close(101)

write(*,*) 'Processing the case located in ', trim(ipath)

! Read the input data:
open(1, file = trim(ipath)//'/merge.inp')

do i = 1, 6     ! skip the header
read(1,*)
end do

read(1,*) Nrun
read(1,*)
read(1,*) istart        ! Range of timesamples in the result
read(1,*) istop
read(1,*)
read(1,*) Nfiles
read(1,*)
do i = 1, Nfiles+1
read(1,*) istep(i)
end do

close(1)

! Read the point data:
open(2, file = trim(ipath)//'/xyzts.dat')

read(2, *) np, nskip, tol, nd1, nd2
close(2)

write(*,*) 'Number of points per step = ', np

write(*,*) 'Processing run #', Nrun

reclength = 2*8+3+15*15     ! record length
recl2 = 1*8 + 4*15  ! merged file rec length
open(20, file = trim(ipath)//'/varts_run'//MyChar2(Nrun)//'.dat'
```

```
    1     , status='unknown', form='formatted', recl=recl2,
access='direct')

    ! loop over files:
    icount = 0
    do j = 1, Nfiles
    write(*,*) 'Processing the step number: ', istep(j)
    if (Nrun.gt.9) then
    if (istep(j).lt.1000) then
    open(3, file =
trim(ipath)//'/varts.'//MyChar3(istep(j))//'.run.'//MyChar2(Nrun)//'.dat'
    1     , status='unknown', form='formatted', recl=reclength,
access='direct')
    else if (istep(j).lt.10000) then
    open(3, file =
trim(ipath)//'/varts.'//MyChar4(istep(j))//'.run.'//MyChar2(Nrun)//'.dat'
    1     , status='unknown', form='formatted', recl=reclength,
access='direct')
    else if (istep(j).lt.100000) then
    open(3, file =
trim(ipath)//'/varts.'//MyChar5(istep(j))//'.run.'//MyChar2(Nrun)//'.dat'
    1     , status='unknown', form='formatted', recl=reclength,
access='direct')
    else
    open(3, file =
trim(ipath)//'/varts.'//MyChar6(istep(j))//'.run.'//MyChar2(Nrun)//'.dat'
    1     , status='unknown', form='formatted', recl=reclength,
access='direct')
    end if
    else
    if (istep(j).lt.1000) then
    open(3, file =
trim(ipath)//'/varts.'//MyChar3(istep(j))//'.run.'//MyChar1(Nrun)//'.dat'
    1     , status='unknown', form='formatted', recl=reclength,
access='direct')
    else if (istep(j).lt.10000) then
    open(3, file =
trim(ipath)//'/varts.'//MyChar4(istep(j))//'.run.'//MyChar1(Nrun)//'.dat'
    1     , status='unknown', form='formatted', recl=reclength,
access='direct')
    else if (istep(j).lt.100000) then
    open(3, file =
trim(ipath)//'/varts.'//MyChar5(istep(j))//'.run.'//MyChar1(Nrun)//'.dat'
    1     , status='unknown', form='formatted', recl=reclength,
access='direct')
    else
    open(3, file =
trim(ipath)//'/varts.'//MyChar6(istep(j))//'.run.'//MyChar1(Nrun)//'.dat'
    1     , status='unknown', form='formatted', recl=reclength,
access='direct')
    end if
    end if
```

```
! read/write the information
iread = 0
do i = 1, istep(j+1)-istep(j)   ! Loop over number of steps
isn = istep(j) + i - 1
! We check if the step is dividable by Nskip:
fin = 0
if (mod(isn,NSkip).eq.0) fin = 1
if (fin) then
iread = iread + 1
!    write(*,*) 'start reading time step number : ', isn
do i1 = 1, np
read(3, '(2I8, I3, 15E15.7)', REC=np*(iread-1)+i1)
1            lstep,jj,iphase,(varts(k), k=1, 15)
!     if (i1.eq.np) write(*,*) i, lstep, isn, jj, iphase
fout = 0
if (lstep.ge.istart.and.lstep.lt.istop) fout = 1
!     if (i.eq.100) write(*,*) varts(1:15)
if (fout) then
icount = icount + 1
write(20,'(1I8, 4E15.7)', REC=icount)
1            lstep,(varts(k), k=2, 5)
end if

end do ! i1, np
end if ! fin
end do   ! i, isteps
close(3)
end do  ! j, Nfiles
```

Varts_BCT.f: generate velocity information of all nodes for different time windows.

```
! Read the point data:
open(2, file = trim(ipath)//'/xyzts.dat')

read(2, *) np, nskip, tol, nd1, nd2, NRun
! Read the point coordinates:
do i = 1, np
read(2, *) xx(i), yy(i), zz(i)
end do
close(2)
write(*,*) 'Number of points per step = ', np
write(*,*) 'Processing run #', Nrun
reclength = 1*8+4*15        ! record length
Nbct = int(1.0E0*(istop - istart)/(deltat/phdt))+1
write(*,*) 'Anticipated number of bct.dat files: ', Nbct
! loop over files:
icount = 0
write(*,*) 'Processing the run number: ', Nrun
open(3, file = trim(ipath)//'/varts_run'//MyChar2(Nrun)//'.dat'
```

```
    1     , status='unknown', form='formatted', recl=reclength,
access='direct')
    ! read/write the information
    iread = 0
    ts1(1) = 1
    do i2 = 1, nbct
    if (i2.lt.nbct) then
    maxts(i2) = nint(deltat/phdt)
    else
    maxts(i2) = mod(istop - istart, maxts(i2-1))
    end if
    ts2(i2) = ts1(i2) + maxts(i2) - 1
    ! Expand the timestep range to provide slight overlap:
    if (i2.eq.1) then
    ts2(i2) = ts2(i2) + ioverlap
    else if (i2.eq.nbct) then
    ts1(i2) = ts1(i2) - ioverlap
    else
    ts1(i2) = ts1(i2) - ioverlap
    ts2(i2) = ts2(i2) + ioverlap
    end if
    write(*,*) 'File ', i2, ' range is timesteps: ', ts1(i2), ts2(i2)
    ts1(i2+1) = ts1(i2) + maxts(i2)
    end do
    ctime = 0.0
    ! Loop over bct.dat files:
    do mbct = 1, nbct
    write(*,*) 'Processing file #', mbct, ' of ', nbct
    if( mbct.ge.0 .and. mbct.le.9)then
    write(filenum,'(i1.1)')mbct
    else if(mbct.ge.10 .and. mbct.le.99)then
    write(filenum,'(i2.2)')mbct
    else if(mbct.ge.100 .and. mbct.le.999)then
    write(filenum,'(i3.3)')mbct
    else if(mbct.ge.1000 .and. mbct.le.9999)then
    write(filenum,'(i4.4)')mbct
    end if
    open(20+mbct, file = trim(ipath)//'/bct.'//trim(filenum)//'.dat'
    1     , status='unknown')
    write(20+mbct, 13) np, ts2(mbct) - ts1(mbct) + 1   !, maxts(mbct)
    ! Loop over points:
    do i1 = 1, np
    ctime = real(ts1(mbct)-1)*phdt
    do i = ts1(mbct), ts2(mbct)   ! Loop over number of steps
    read(3, 11, REC=np*(i-1)+i1)
    1            lstep,(varts(k), k=2, 5)
    ! Record the point coordinates and the number of time steps
    if (i.eq.ts1(mbct)) then
    write(20+mbct, 12) xx(i1), yy(i1), zz(i1), ts2(mbct) - ts1(mbct) + 1
!, maxts(mbct)
    end if
    ! Accumulate time:
    if (i.gt.1) ctime = ctime + varts(5)
```

```
    fout = 0
    if (ctime.ge.tstart.and.ctime.lt.tstop) fout = 1
    if (fout) then
    icount = icount + 1
    write(20+mbct,10) varts(2:4), ctime  !, i1, i, lstep, jj, iphase
    end if
    end do   ! i, isteps
    end do ! i1, np
    close(20+mbct)
    end do ! mbct, nbct
```

bct_partition.f: generate the selected nodes information for different time window and cores.

```
    open(30000,file='path.dat')
    read(30000,50) ipath
    50       format(A80)
    close(30000)
    !        write(*,*) bctnum
    do p=1, bctnum
    if( p.ge.0 .and. p.le.9)then
    write(filenum2,'(i1.1)')p
    else if(p.ge.10 .and.p .le.99)then
    write(filenum2,'(i2.2)')p
    else if(p.ge.100 .and.p.le.999)then
    write(filenum2,'(i3.3)')p
    else if(p.ge.1000 .and.p.le.9999)then
    write(filenum2,'(i4.4)')p
    end if
    open(p, file=trim(ipath)//'/bct.'//trim(filenum2)//'.dat')
    read(p,*) np, nts
    write(*,*) np*(nts+1)
    do m=1, np*(nts+1) !lopp over the points
    read(p,*) u(m), v(m), w(m), t(m)
    enddo
    close(p)
    open(20000,file=trim(ipath)//'/myrank.txt')
    do while(.true.)
    read(20000,*,iostat=stat) myrank
    if(stat==0) then
    open(bctnum+2+myrank, file =
trim(ipath)//'/bctin.dat.'//trim(filenum1)//'')
    read(bctnum+2+myrank, *) np_bct
    do l=1, np_bct
    read(bctnum+2+myrank, *) x(l), y(l), z(l)
    enddo
    close(bctnum+2+myrank)


open(1000+myrank,file=trim(ipath)//'/bct_input/bct.dat.'//trim(filenum2)//
'.'
    & //trim(filenum1)//'', status='unknown')
```

```
write(*,*) 'Processing processor', myrank,' of time series', p
write(1000+myrank,13) np_bct, nts
do i=1, np_bct
x_p=x(i)
y_p=y(i)
z_p=z(i)
write(1000+myrank,12) x_p, y_p, z_p, nts
flag=0
do j=1, np
if (flag.eq.0) then
if ((abs(y_p-v((j-1)*(nts+1)+1)).lt.epsd).and.(
& abs(z_p-w((j-1)*(nts+1)+1)).lt.epsd).and.
& (abs(x_p-u((j-1)*(nts+1)+1)).lt.epsd)) then
do k=1, nts
write(1000+myrank,11) u((j-1)*(nts+1)+1+k), v((j-1)*(nts
& +1)+1+k), w((j-1)*(nts+1)+1+k), t((j-1)*(nts+1)+1+k)
enddo
flag=1
else
continue
end if
endif
enddo !end of search identical points
enddo !end of loop over points on processor
close(1000+myrank)
else if(stat>0) then
write(*,*) 'something is wrong with reading operation'
else
exit
endif
enddo
close(20000)
enddo
```

Appendix E

This appendix contains the modules to analyze the varts data.

```
~~
    Nhom2 = Nhom
    time1 = time1 + raw(5,j,(i-1)*Nhom+1,ir)  ! accumulate time
    time1p = time1p + raw(5,iphtime(3,k),(i-1)*Nhom+1,ir)  ! accumulate
time for pressure term
    Mean(1, k) = Mean(1, k) + raw(2, j, (i-1)*Nhom+1,ir)*raw(5, j, (i-
1)*Nhom+1,ir)  ! multiplied by dt

    Mean(2, k) = Mean(2, k) + (1)**ih2 * raw(3, j, (i-1)*Nhom+1,ir)*raw(5,
j, (i-1)*Nhom+1,ir)  ! multiplied by dt
    ! Span wise (W) velocity, time, dU/dx, dV/dx and dW/dx:
    Mean(3:7, k) = Mean(3:7, k) + raw(4:8, j, (i-1)*Nhom+1,ir)*raw(5, j,
(i-1)*Nhom+1,ir)  ! multiplied by dt
    ! dU/dy, dV/dy and dW/dy is:
    Mean(8:10, k) = Mean(8:10, k) +  raw(9:11, j, (i-1)*Nhom+1,ir) *raw(5,
j, (i-1)*Nhom+1,ir)  ! multiplied by dt
    ! dU/dz, dV/dz and dW/dz is:
    Mean(11:13, k) = Mean(11:13, k) + raw(12:14, j, (i-
1)*Nhom+1,ir)*raw(5, j, (i-1)*Nhom+1,ir)  ! multiplied by dt
    Mean(14, k) = Mean(14, k) + raw(1, j, (i-1)*Nhom+1,ir)*raw(5, j,(i-
1)*Nhom+1,ir)
! Turbulent fluctuation fields
    fluct = fluct + 0.5E0*(raw(k1+1, j, (i-1)*Nhom+1, ir)-Mean(k1,k))
*(raw(k1+1, j, (i-1)*Nhom+1, ir)-Mean(k1,k))*raw(5, j,(i-1)*Nhom+1, ir)
! Turbulent transport contribution:
    ttfl = ttfl + 0.5E0*((raw(k1+1, j, (i-1)*Nhom+1, ir) -
Mean(k1,k))**2.0E0)*(raw(3, j, (i-1)*Nhom+1, ir)-Mean(2,k))*raw(5, j, (i-
1)*Nhom+1, ir)
    fluctx=fluctx+0.5E0*(raw(1+1, j, (i-1)*Nhom+1, ir)-
Mean(1,k))*(raw(1+1, j, (i-1)*Nhom+1, ir)-Mean(1,k))*raw(5, j,(i-
1)*Nhom+1, ir)
    flucty=flucty+0.5E0*(raw(2+1, j, (i-1)*Nhom+1, ir)-
Mean(2,k))*(raw(2+1, j, (i-1)*Nhom+1, ir)-Mean(2,k))*raw(5, j,(i-
1)*Nhom+1, ir)
    fluctz=fluctz+0.5E0*(raw(3+1, j, (i-1)*Nhom+1, ir)-
Mean(3,k))*(raw(3+1, j, (i-1)*Nhom+1, ir)-Mean(3,k))*raw(5, j,(i-
1)*Nhom+1, ir)
    TKE(1,k,i) = TKE(1,k,i) + fluct/time1   ! divided by this phase time
    TKEX(1,k,i)=TKEX(1,k,i)+fluctx/time1
    TKEY(1,k,i)=TKEY(1,k,i)+fluctz/time1
    TKEZ(1,k,i)=TKEZ(1,k,i)+fluctz/time1
    DiffT(k,i) = DiffT(k,i) -  ttfl/time1   ! Only the turbulent transport
!.
    ! Add the pressure diffusion component:
     DiffP(k,i) = DiffP(k,i) - 1.0/rho*( raw(3, j, (i-1)*Nhom+1, ir) -
Mean(2,k))*(raw(1, j, (i-1)*Nhom+1, ir) - Mean(14,k))*raw(5, j,(i-
1)*Nhom+1, ir)/time1
```

```
    if (nd2.ge.15) then !two-phase cases
    write(5,10)  x(Mcoord), y(Mcoord), z(Mcoord), Mean(1:3, k),
TKE(1,k,i), Eps(1,k)
    1     , Alpha(k), Mean2(1:3, k), TKE(2,k,i), Eps(2,k), Mean(14,k),
Mean2(14,k)
    2     , tau_xy, dUdy, nuT/nu_cl, Cmu, TKEX(1,k,i),
TKEY(1,k,i),TKEZ(1,k,i)
    3     , DiffP(k,i), DiffT(k,i), Prod(k,i)
    else !single-phase cases
    write(5,10)  x(Mcoord), y(Mcoord), z(Mcoord), Mean(1:3, k),
TKE(1,k,i), Eps(1,k), Mean(14,k)
    1     , tau_xy, dUdy, nuT/nu_cl, Cmu, TKEX(1,k,i),
TKEY(1,k,i),TKEZ(1,k,i)
    2    , DiffP(k,i), DiffT(k,i), Prod(k,i)
    endif
~~
```

Appendix F

This appendix contains the subroutines to introduce artificial interface thickness on the solid sphere surface.

```
if (iLSet .eq. 0)then

rho  = datmat(1,1,1) ! single fluid model, i.e., only 1 density
rmu = datmat(1,2,1)    ! viscosity
cp=datmat(1,3,1)
k_T=datmat(1,4,1)
datmat(1,1,2)=1.161
datmat(1,2,2)=1.845e-5

! Smooth the transition of properties for a "distance" of epsilon_ls
!around the interface.  Here "distance" is define as the value of the
!levelset function.  If the levelset function is properly defined,
!this is the true distance normal from the front.  Of course, the
!distance is in a direction normal to the front.

Sclr = zero
sclrx=zero
sclry=zero
sclrz=zero
isc=abs(iRANS)+6
do n = 1, nshl
Sclr = Sclr + shape(:,n) * yl(:,n,isc)
sclrx=sclrx+shape(:,n)*xl(:,n,1)
sclry=sclry+shape(:,n)*xl(:,n,2)
sclrz=sclrz+shape(:,n)*xl(:,n,3)
enddo
!         if (icode .ge. 20) then !scalar 2
do i= 1, npro
  epsilon_lsd_tmp=0.0002 !artificial interface thickness
  Sclr(i)=sqrt((sclrx(i)-0.0075)**2+(sclry(i)-0.0125)**2+
& (sclrz(i)-0.0)**2)-0.0025
 if (sclr(i) .lt. - epsilon_lsd_tmp) then
     prop_blend(i) = zero
  elseif  (abs(sclr(i)) .le. epsilon_lsd_tmp) then
     prop_blend(i) = 0.5*(one + Sclr(i) / epsilon_lsd_tmp +
&                          (sin(pi*Sclr(i)/epsilon_lsd_tmp))/pi)
  elseif (sclr(i) .gt. epsilon_lsd_tmp) then
     prop_blend(i) = one
  endif
enddo
```